UNIVERSITY OF CALIFORNIA
Santa Barbara

Linked and Knotted Fields in Plasma and Gravity

A Dissertation submitted in partial satisfaction
of the requirements for the degree of

Doctor of Philosophy

in

Physics

by

Amy Violet Thompson

Committee in Charge:

Professor Dirk Bouwmeester, Chair

Professor Donald Marolf

Professor David Berenstein

September 2014

The Dissertation of
Amy Violet Thompson is approved:

Professor Donald Marolf

Professor David Berenstein

Professor Dirk Bouwmeester, Committee Chairperson

May 2014

Linked and Knotted Fields in Plasma and Gravity

Acknowledgements

I would to acknowledge my colleagues who were collaborators on the work presented in this thesis. Joe Swearngin contributed immensely to the development of the ideas, and also helped a great deal with the calculations and understanding the results. Alex Wickes worked on the development of the Mathematica code used to generate our results, and helped make many of the figures. Jan Willem Dalhuisen contributed to many discussions, making suggestions and helping with my understanding of the subjects, especially with regards to twistor theory and gravitational radiation. Chris B. Smiet performed the plasma simulations in Chapter 4 and has given many helpful suggestions about the soliton fields in plasma. Dirk Bouwmeester was my advisor for this thesis and also had many discussions with me on both plasma physics and gravity.

I am grateful for a number of fellowships that have supported me during my graduate studies at UCSB: a National Defense Science and Engineering Graduate (NDSEG) Fellowship (2008-2010), a UC Dean's Fellowship (2010-2011), a Marie Curie Fellowship from the European Commission (2012), and a UC Graduate Division Dissertation Fellowship (2014). I would also like to thank Leiden University for hosting me during several extended visits.

Curriculum Vitæ

Amy Violet Thompson

Education

2011	Master of Arts in Physics, Univ. of California, Santa Barbara.
2007	Master of Science in Optics, Univ. of Central Florida.
2005	Bachelor of Science in Physics, Illinois Institute of Technology.

Experience

2008 – 2014	Graduate Research Assistant, Univ. of California, Santa Barbara.
2012	Visiting Researcher, Leiden University.
2005 – 2008	Graduate Research Assistant, Univ. of Central Florida.
2003 – 2005	Undergraduate Research Assistant, Illinois Institute of Technology and Fermi National Accelerator Laboratory.

Publications

Amy Thompson*, Joe Swearngin*, and Dirk Bouwmeester (*equal contributors): "Linked and Knotted Gravitational Radiation," In *Journal of Physics A: Mathematical and Theoretical*, August 2014.

Amy Thompson, Joe Swearngin, Alexander Wickes, and Dirk Bouwmeester: "Constructing a class of topological solitons in magnetohydrodynamics," In *Physical Review E*, April 2014.

Joe Swearngin, Amy Thompson, Alexander Wickes, Jan Willem Dalhuisen, and Dirk Bouwmeester: "Gravitational Hopfions," In *arXiv: gr-qc/1302.1431*, February 2014.

Amy V. Thompson, Hubert Seigneur, Michael N. Leuenberger, and Winston V. Schoenfeld: "Optical switching based on the conditional Faraday effect with electron spins in quantum dots," In *IEEE Journal of Quantum Electronics*, June 2009.

Jeremy W. Mares, Matthew Falanga, Amy V. Thompson, Andrei Osinsky, Jianjun Q. Xie, Brian Hertog, Amir Dabiran, Peter P. Chow, Sergey Karpov, and Winston V. Schoenfeld: "Hybrid CdZnO/GaN quantum-well light emitting diodes," In *Journal of Applied Physics*, November 2008.

Amy V. Thompson, Hubert Seigneur, Michael N. Leuenberger, Winston V. Schoenfeld: "Active components in photonic integrated circuits using electron spins in quantum dots," In *SPIE Proceedings*, April 2008.

Jeremy W. Mares, Jonathan Harben, Amy V. Thompson, Dean W. Schoenfeld, and Winston V. Schoenfeld: "Gamma Radiation Induced Degradation of Operating Quantum Dot Lasers," In *IEEE Transactions on Nuclear Science*, April 2008.

Wantae Lim, David P. Norton, Stephen J. Pearton, Xiangjun J. Wang, Weimin M. Chen, Irina A. Buyanova, Andrei Osinsky, Jeremy W. Dong, Brian Hertog, Amy V. Thompson, Winston V. Schoenfeld, Yu-Lin Wang, and Fan Ren: "Migration and luminescence enhancement effects of deuterium in ZnO/ZnCdO quantum wells," In *Applied Physics Letters*, January 2008.

Amy V. Thompson, Casey Boutwell, Jeremy W. Mares, Winston V. Schoenfeld, Andrei Osinsky, Brian Hertog, Jianjun Q. Xie, Stephen J. Pearton, and David P. Norton: "Thermal stability of CdZnO/ZnO multi-quantum-wells," In *Applied Physics Letters*, November 2007.

Jeremy W. Mares, Forrest R. Ruhge, Amy V. Thompson, Pieter G. Kik, Andrei Osinsky, Brian Hertog, Amir M. Dabiran, Peter P. Chow and Winston V. Schoenfeld: "Optical and morphological properties of MBE grown wurtzite $Cd_xZn_{1-x}O$ thin films," In *Optical Materials*, October 2007.

Amy V. Thompson, Jeremy W. Mares, Hubert Seigneur, Winston V. Schoenfeld: "Optimization of GaAs PIN diodes for neutron detection," In *SPIE Proceedings*, February 2007.

Ivan B. Divliansky, Gregory Weaver, Michael Petrovich, Toufic Jabbour, Hubert P. Seigneur, Caleb Parnell-Lampen, Amy Thompson, Kevin D. Belfield, and Stephen M. Kuebler: "CAD-integrated system for automated multi-photon three-dimensional micro- and nanofabrication," In *SPIE Proceedings*, January 2005.

Abstract

Linked and Knotted Fields in Plasma and Gravity

Amy Violet Thompson

Hopfions are a class of fields whose topology is derived from the Hopf fibration, with field lines that are linked circles which lie on a set of space-filling nested toroidal surfaces. In this thesis, we use analytic and computational methods to study hopfions and their generalization to field configurations based on torus knots in both plasma and gravity.

The Kamchatnov-Hopf solution to the magnetohydrodynamic (MHD) equations is a topological soliton, a field configuration that is stable due to a conserved topological quantity, with linking number one. By realizing that the angular momentum can also serve as a secondary stabilizing mechanism for certain field configurations, we generalize this solution to a class of topological solitons with linking number greater than one and show they are stable in ideal MHD. When studied in full resistive MHD, the results of simulations indicate that the non-zero linking number serves to inhibit the decay of the magnetic field energy.

The vacuum Maxwell and linearized Einstein equations take a similar form when expressed as spin-N field equations, suggesting that electromagnetic and gravitational radiation possess analogous topologically non-trivial field configurations. The solutions to the massless spin-N equations can be found by complex

contour integral transformations with generating functions in terms of twistor variables. Using these methods, we construct the null electromagnetic hopfion and the analogous Petrov Type N gravitational solution. The fields are decomposed into tendex and vortex lines, the analog of the electromagnetic field lines, to investigate their physical properties and characterize their topology. For both electromagnetism and gravity the topology manifests in the lines of force.

We then show that the hopfion solutions are the simplest case in a class of Type N linked and knotted gravitational solutions based on torus knots. Reparameterizing the twistor generating functions in terms of the winding numbers of the field lines allows one to choose the degree of linking or knotting of the associated field configuration.

Finally, we discuss how the singularity structure of the twistor generating functions determines the spinor classification of the fields in Minkowski space. Since the solutions are constructed by contour integral transformations, the poles of the generating functions are directly related to the geometry of the physical fields. By modifying the generating functions, we extend the construction of the Type N gravitational hopfion to find the analogous spin-2 solutions of different Petrov classifications and characterize their tendex and vortex line configurations.

Contents

List of Figures

List of Tables

Chapter 1

Introduction

Knots and links are quite remarkable given that they are as old and ubiquitous as ropes and thread and yet have only relatively recently seen a rigorous formulation within mathematics. The study of knots and links has enjoyed a close relationship with physics since its inception by Gauss [1]. Today the application of these topological structures in theoretical physics is more widespread than it has ever been, from fault resistant quantum computing [2], hadron models [3,4], topological MHD and fluid mechanics [5,6], classical field theories [7–11], quantum field theory [12, 13], DNA topology [14], nematic liquid crystals [15], helium superfluid [16] to Bose-Einstein condensates [17] just to name a few. In this thesis we shall focus on linked and knotted field line configurations in classical electromagnetism, plasma physics and gravitational radiation.

1.1 Overview

It is well-known that there exist solutions to Maxwell's Equations with non-trivial field line topology. *Hopfions*, or linked field configurations whose topology is derived from the Hopf fibration, are one particular class of solutions that often appears in physics. The Hopf fibration is a map from the 3-sphere ($\mathbb{S}^3$) to the 2-sphere ($\mathbb{S}^2$) such that great circles on $\mathbb{S}^3$ map to single points on $\mathbb{S}^2$. The circles on $\mathbb{S}^3$ are called the *fibers* of the map, and when projected stereographically onto $\mathbb{R}^3$ the fibers correspond to linked circles that lie on nested, toroidal surfaces and fill all of space. The fibers can be physically interpreted as the field lines of the configuration, giving the hopfion fields their distinctive toroidal structure [8].

First, we will review hopfion fields in electromagnetism. The solution method originally outlined by Rañada [18] is based on reformulating Maxwell's equations in the language of the exterior calculus leading to a simple construction of solutions on compactified space-time. We will discuss the topological properties of hopfions and how these solutions can arise physically as optical radiation. Finally, we will explore their relationship to other linked and knotted EM fields and give a method for the generalizing hopfions to field configurations based on torus knots [19].

Toroidal magnetic fields with linked field lines are related to increased plasma confinement and stability [20]. The hopfion solution to the magnetohydrodynamic (MHD) equations found by Kamchatnov represents a topological soliton, a field

configuration that is stable due to a conserved topological quantity [5]. Using a modified version of the construction methods for null EM fields, we generalize this solution to an entire class of topological solitons based on torus knots and show they are stable in ideal MHD. Numerical methods for investigating the time evolution of magnetic fields in plasma are discussed. We are currently working on simulations involving these topological solitons and the initial results show that the topological structure is related to the stability of the fields.

We then review twistor integral methods that will allow us to construct solutions to the linearized Einstein's equations with linked and knotted field line configurations. The salient feature of the null EM hopfion is the Poynting vector which is everywhere tangent to a Hopf fibration that propagates at the speed of light without deformation. The Poynting vector structure when extended to become a future pointing light-like 4-vector generates a set of shear-free space-filling null geodesics, collectively referred to as a Robinson congruence. In the twistor formalism the Robinson congruence features prominently as a framework to which many different physical fields are associated via the Penrose transform. From the twistor perspective [21] all solutions of the massless spin-N field equations in Minkowski space are seen to arise from the singularities of homogeneous functions on twistor space. Of particular note are the solutions known as *elementary states*, fields which are constructed from homogeneous twistor functions whose vanishing defines a Robinson congruence [22]. There is a direct correspondence between

the elementary states and the EM hopfion. Moreover, the relationship between the massless linear relativistic fields (massless Dirac, vacuum Maxwell, massless Rarita-Schwinger, and linearized vacuum Einstein equations), as expressed in the form of the massless spin-N field equations, implies that all linear physical fields possess analogous topologically non-trivial field configurations.

After a review of spinor and twistor methods, we present the spin-N hopfion. These solutions correspond to the simplest twistor elementary states. For $N = 1$ this reproduces exactly the EM hopfion constructed by Rañada. The spin-2 solution is analyzed within the framework of gravito-electromagnetism [23, 24]. By decomposing the Weyl tensor into spatial gravito-electric and gravito-magnetic tensors, and the time evolution of the gravitational hopfion can be characterized in terms of the EM hopfion.

We then show that this method can be extended to construct spin-N fields based on torus knots. The twistor functions corresponding to the elementary states admit a parameterization in terms of the poloidal and toroidal winding numbers of the torus knots, allowing one to choose the degree of linking or knotting of the associated field configuration. Using the gravito-electromagnetic formalism, we show that the torus knot structure is exhibited in the tendex and vortex lines. We describe the topology of the gravitational fields and its physical interpretation in terms of the tidal and frame drag forces of the gravitational field.

Finally, we consider the relationship between the singularities of the twistor generating functions and the geometry of the resulting physical fields. Since the fields are constructed through a contour integral transform, the poles of the twistor functions determine the spinor structure of the solutions in Minkowski space. By modifying the twistor function that generates the null EM hopfion, we find the generating function for a non-null EM solution with linked field lines. In a similar manner, we use the Type N hopfion to construct gravitational hopfions of Petrov Type D and Type III. For each case, we describe the time evolution of the tendex and vortex configuration, and how the topological structure of the fields is related to the Robinson congruence.

1.1.1 New Results

The main results presented in this thesis relate to the construction and analysis of linked and knotted fields in magnetic plasmas and gravitational radiation, both through analytic and computational methods, and are summarized as follows.

In Chapter 4, we construct a new class of magnetic field configurations in plasma based on a torus knot topology. A subset of these solutions are shown to represent topological solitons in ideal MHD by a stability analysis based on a scaling argument. The evolution of the solitons is investigated in full MHD using numerical simulations. We discuss the implications of these simulations and how

the results might lead to the construction of solutions with greater stability in realistic plasma systems.

In Chapter 9, we give a new mathematical construction using twistor methods for known null electromagnetic solutions with field line configurations related to the Hopf fibration. This allows us to construct linearized gravitational fields of Petrov Type N based on the same structure. We analyze their physical properties using the gravito-electromagnetic decomposition of the Weyl curvature tensor and show that, similarly to the electromagnetic case, for gravitational fields the topology also manifests in the lines of force.

In Chapter 10, the radiative electromagnetic and gravitational hopfions are shown to be the simplest case in a class of solutions with field line structures based on torus knots. These solutions are also shown to correspond to the elementary states of twistor theory. Although the elementary states were previously known, the details of their structure and the underlying torus knot topology have never been described in literature.

In Chapter 11, we extend the analogy with the electromagnetic hopfion to construct linked gravitational fields of Petrov Type D and Type III. We also characterize the structure of their lines of force and discuss their time evolution.

1.2 History

1.2.1 Knot Theory

The foundation for the mathematical theory of knots began with Gottfried Wilhelm Leibniz's *geometria situs*, or "geometry of position" which is independent of magnitude or scale. He explained in a letter to Christian Huygens in 1679 [25]

> *I am not content with algebra, in that it yields neither the shortest proofs nor the most beautiful constructions of geometry. Consequently, in view of this, I consider that we need yet another kind of analysis, geometric or linear, which deals directly with position, as algebra deals with magnitude.*
>
> Gottfried Wilhelm Leibniz

In 1771, the first paper to directly address the mathematics of knot theory in terms of the geometry of position was *Remarks on the theory of positions* by Alexandre-Théophile Vandermonde [26]. In it he stated

> *Whatever the twists and turns of a system of threads in space, one can always obtain an expression for the calculation of its dimensions, but this expression will be of little use in practice The craftsman who fashions a braid, a net, or some knots will be concerned, not with questions of measurement, but with those of position: what he sees there is the manner in which the threads are interlaced.*
>
> Alexandre-Théophile Vandermonde

Carl Friedrich Gauss played an important role in the development of knot theory. He had a deep interest in knots, and as early as 1794, he made drawings of knots and considered methods for describing different configurations [1]. His

approach was to draw the entire knot structure, then label each crossing in the order that one would find it as they started at an arbitrary point and traced the entire knot until they arrived back at that point. He called this classification the "scheme of the knot." He sketched and described 13 knots in this way. Throughout the following years, Gauss also made many more sketches of knots, including one which contains a drawing of a braid next to a complex coordinate representation of the height of each strand [27]. His interest in knots remained into his later work in electromagnetism, and led him to make one of the most important breakthroughs in the early history of knot theory in 1833. He considered the work done on a magnetic pole moving in closed loop around a closed loop of electric current. In the process, he discovered what is now called the Gauss linking integral, which is equal to an integer describing the linking number of the two curves [28].

Johann Benedict Listing, a student of Gauss at Göttingen University, became interested in Gauss's work on knot theory. He was the first person to use the term "Topologie" (which translates to "Topology") in reference to configurations with links and knots, and in his 1847 paper *Vorstudien zur Topologie* he explained this new branch of mathematical study

> *I hope you will let me use the name "Topology" for this kind of studies of spatial images, rather than suggested by Leibniz name "geometria situs", reminding of notion of "measure" and "measurement" playing here absolutely subordinate role and confiding with "géometrié de position" which is established for a different kind of geometrical studies. Therefore by Topology we will mean the study of modal relations of spatial images, or laws of connectedness, mutual disposition and*

> *traces of points, lines, surfaces, bodies, and their parts or their mutual unions in space, independently of relations of measures and quantities. (Translated by M. Sokolov.)*
>
> Johann Benedict Listing

Listing went on to make contributions to understanding the relationship between a knot and its mirror image, referred to as the chirality of the knot. In 1947 he showed the right-handed and left-handed trefoil are not equivalent, and in 1949 he showed that the figure eight knot and its mirror image are equivalent, or amphichiral [1].

Gauss's linking integral also inspired Hermann Karl Brunn to formalize the concept of a knot diagram in 1892. Brunn realized that the linking number can be found from a knot diagram by counting the crossings of the link components K_1 and K_2, and assigning to each crossing a value of $+1$ for K_1 crossing under K_2 and -1 for K_1 over K_2 [29].

1.2.2 Knots in Physics

In the 1800's electromagnetic waves were generally thought of as vibrations of the "luminiferous ether," leading many scientists to attempt to understand electromagnetism in terms of analogies with fluid mechanics [30]. One clear motivation for this is that the electrostatic equations in vacuum

$$\nabla \cdot \vec{E} = 0 \tag{1.1}$$

$$\nabla \times \vec{E} = 0 \tag{1.2}$$

have the same form as the equations describing the flow of an incompressible fluid in the case of no friction, no viscosity, and no vorticity (curl)

$$\nabla \cdot \vec{v} = 0 \tag{1.3}$$

$$\nabla \times \vec{v} = 0. \tag{1.4}$$

where $\vec{v}$ is the velocity of the fluid.

In 1858, Hermann von Helmholtz generalized this to the case with $\nabla \times \vec{v} \neq 0$ and showed that vortex lines of an ideal fluid are stable closed curves. Peter Guthrie Tait made a demonstration of this effect by pushing smoke out of a hole in a box, thus generating smoke rings. William Thomson (Lord Kelvin) saw this demonstration, and realizing the connection with electromagnetism. This led him to propose his Theory of Vortex Atoms, in which atoms are vortices of the ether. After the Michelson and Morley experiment disproved the existence of the ether in 1887 this theory lost favor, and even Thomson admitted that it was unsuccessful in giving a physical description of atoms in 1905. Despite its failure in that regard, it served to introduce knot theory to the physics community and led to searches for other applications [30].

It is also worth noting that Maxwell was interested in knot theory and its application to physics. He wrote several unpublished papers on knot theory during the late 1800's which were not found until after the same results had been discovered other scientists. These works included classifying knot diagrams and a discussion of the three ways to change a diagram without affecting the knot, which were later discovered by Reidemeister in 1926 [31].

1.2.3 Lines of Force in Electromagnetism

The concept of lines of force was first proposed by Michael Faraday. Around 1931 he began a series experiments on induction which led him to develop this perspective [32]. If a wire intersects magnetic lines of force then a current will be induced in the wire, and Faraday's law of induction describes how the magnitude of the current depends on the rate of change of the intersecting lines. He demonstrated this by inserting a magnet into a helical coil of wire, and as the magnet moved the wire cut through the lines of force thus inducing a current.

In contrast to most of the scientists of the day, Faraday considered electromagnetism to be a force, which could occur in vacuum, rather than a disturbance propagating in a fluid, or ether. He wanted to apply this concept to a broad range of physical phenomena. Many of his writings mention his desire to understand the interconnectedness of the different forces of nature. In 1949 he wrote [33],

"The exertions in physical science of late years have been directed to ascertain not merely the natural powers, but the manner in which they are linked together, the universality of each in its own action, and their probable *unity in one*." In his 1857 paper *On the Conservation of Force* [34], Faraday explained "if it acts in time and across space, it must act by physical lines of force", including "heat, or electricity, or gravitation, or any other form of force." In particular Faraday wanted to understand lines of force in gravity, and in that same year he exchanged several letters with Maxwell on the subject [35]. Maxwell was optimistic about this approach and in his reply wrote that he hoped it could explain the motion of planets and stars. Maxwell not only wanted to understand the physical nature of lines of force in electromagnetism and gravity, but he also expressed interest in a mathematical formulation of the analogous relationship between the two forces.

1.2.4 Lines of Force in Gravity

In 2010, Faraday's vision of finding a gravitational analog of electromagnetic field lines was realized. These gravitational lines of force for a particular observer were introduced by Nichols, *et al.* [24], who were motivated by the desire to understand the non-linear dynamics of curved space-time in a more intuitive, directly physical way than previous approaches. The physical understanding of the electromagnetic field is based upon the decomposition of the Faraday field

strength tensor onto space-like foliations of constant time yielding two spacial vector fields interpreted as the electric and magnetic fields. Analogously, the Weyl curvature tensor admits a decomposition onto constant time hyperplanes yielding two spatial tensors called the gravito-electric and gravito-magnetic tensors. The integral curves of the eigenvector fields of these tensors are called tendex and vortex lines respectively and represent the gravitational analog of electromagnetic field lines. This method was elucidated through a series of papers where it was applied to I) weak field solutions [24], II) stationary black holes [36], and III) weak perturbations of stationary black holes [37].

This method of GEM decomposition is well-suited to studying linked and knotted fields because, as we will show, the field topology manifests in the lines of force for both the electromagnetic and analogous gravitational solutions.

Chapter 2

Knots in Electromagnetism

One of the simplest radiative solutions with non-trivial topology is called the *EM hopfion* and was developed by Rañada in the 1980's [18]. A *hopfion* is a field configuration based on a topology derived from the Hopf fibration. The EM hopfion is a null solution to the source-free Maxwell's equations such that any two field lines associated to either the electric, magnetic, or Poynting vector fields (EBS fields) are closed and linked exactly once [7]. When an EM hopfion is decomposed onto hyperplanes of constant time there always exists a hyperplane wherein the EBS fields are tangent to the fibers of three orthogonal Hopf fibrations.

The derivation presented here uses the normalized area element of $\mathbb{S}^2$ and the pullback by the Hopf map to generate a field configuration with linked field lines. We then discuss how this configuration can be generalized to field line configurations based on a torus knot topology.

2.1 Linking Number

Before we derive the solutions with linked field lines, we will discuss the concept of linking number and how it relates to the structure of physical fields. Typically for EM fields, this is expressed in terms of the helicity carried by the magnetic field. This quantity, called the magnetic helicity h_m, is proportional to the linking number (and equal if the field is normalized).

The Gauss linking number counts the linking of two distinct curves [38]. If two closed curves are labeled 1 and 2 and parameterized by $\vec{x}(\sigma)$ and $\vec{y}(\tau)$ respectively, with $\vec{r} = \vec{x} - \vec{y}$, then the Gauss linking number is given by the double integral

$$L_{12} = \frac{1}{4\pi} \oint_1 \oint_2 \frac{\vec{r}}{r^3} \cdot \left(\frac{d\vec{x}}{d\sigma} \times \frac{d\vec{y}}{d\tau} \right) d\sigma d\tau. \tag{2.1}$$

A magnetic field will possess an infinite number of field lines each with infinitesimal magnetic flux, but it can be approximated as a set of closed flux tubes. If each of N flux tubes carries a total flux Φ_i, then the magnetic helicity can be calculated by

$$h_m = \sum_{i=1}^{N} \sum_{j=1}^{N} L_{ij} \Phi_i \Phi_j. \tag{2.2}$$

If we let $N \to \infty$ then $\Phi_i \to 0$, and from Eqns. (2.1) and (2.2) we find

$$h_m = \frac{1}{4\pi} \iint \frac{\vec{r}}{r^3} \cdot \left[\vec{B}(x) \times \vec{B}(y) \right] d^3x d^3y. \tag{2.3}$$

This is essentially taking the sum over the linking of each pair of field lines in a volume. By taking vector potential in the Coulomb gauge,

$$\vec{A}(x) = \frac{1}{4\pi} \int \frac{\vec{r}}{r^3} \times \vec{B}(y) d^3y. \tag{2.4}$$

we arrive at the standard expression for magnetic helicity

$$h_m = \int \vec{A} \cdot \vec{B} d^3x. \tag{2.5}$$

2.2 Differential Geometry and Electromagnetism

The electromagnetic field strength tensor is described by a differential 2-form on Minkowski space $\mathbb{M}$ [1] that is the exterioir derivative of a 1-form potential A

$$F = dA.$$

Maxwell's equations are then expressed in terms of F, its dual $*F$, and the dual of a 4-current $*J$ as

$$\begin{aligned} dF &= 0 \\ d*F &= *J. \end{aligned}$$

In vacuum the current vanishes and Maxwell's equations simplify to

$$dF = d*F = 0.$$

[1] We follow the conventions of Penrose [39] so that $\eta = diag\,(1, -1, -1, -1)$.

There are two important properties of the exterior derivative d that we will need later:

1. The exterior derivative of an n-form is an $(n+1)$-form, and thus is zero on an n-dimensional manifold.

2. The exterior derivative commutes with the pullback operation, so that

$$d(f^*\omega) = f^* d\omega$$

for any differential form ω and smooth function f.

These properties of differential forms lead to an obvious geometric solution method:

1. $dF = 0$ trivially for any 2-form F on a 2D manifold, so the first Maxwell's equation is trivially satisfied for the pullback $\varphi^*\sigma$ of any 2-form from any 2D manifold.

2. If we introduce a second pullback which is dual to the first $*\vartheta^*\sigma = \varphi^*\sigma$, then we can construct a solution to the system $dF = d*F = 0$, where $F = -\varphi^*\sigma$ and $*F = \vartheta^*\sigma$.

Now that we have this solution method, we will derive the EM field from the normalized area 2-form σ on $\mathbb{S}^2$. Given a smooth map $\varphi : \mathbb{M} \longrightarrow \mathbb{S}^2$, then

$$F = \varphi^*\sigma \tag{2.6}$$

implies that

$$\begin{aligned} dF &= d\varphi^*\sigma \\ &= \varphi^* d\sigma \\ &= 0 \end{aligned}$$

since $\mathbb{S}^2$ is a 2D manifold and 3-forms will vanish. The dual of Eqn. (2.6) yields

$$*F = *\varphi^*\sigma.$$

We then want to find a second map $\vartheta : \mathbb{M} \longrightarrow \mathbb{S}^2$ such that

$$*\varphi^*\sigma = \vartheta^*\sigma,$$

so the second Maxwell equation is trivially satisfied as

$$\begin{aligned} d * F &= d * \varphi^*\sigma \\ &= d\vartheta^*\sigma \\ &= \vartheta^* d\sigma \\ &= 0. \end{aligned}$$

Now we must find the pair of maps (φ, ϑ) such that

$$F = \varphi^*\sigma \tag{2.7}$$

$$*F = \vartheta^*\sigma. \tag{2.8}$$

2.3 Hopf Map

We will obtain a pair of maps (φ, ϑ) corresponding to a physical field configuration, first by finding the Cauchy data for the fields at $t = 0$ and then using Fourier analysis to determine their time evolution. Consider that these should be finite-energy fields and therefore be single-valued at infinity. This means that at each instant of time, the fields can be defined on $\mathbb{R}^3$, or equivalently on its 1-point compactification $\mathbb{S}^3$. Thus, we seek maps (φ, ϑ) which take $\mathbb{S}^3 \longrightarrow \mathbb{S}^2$.

The Hopf map or Hopf fibration is a well-known map of this form sending great circles on $\mathbb{S}^3$ to single points on $\mathbb{S}^2$. These great circles on S^3 are the $\mathbb{S}^1$ fibers of the map. The Hopf fibration is denoted by

$$\mathbb{S}^3 \xrightarrow{\mathbb{S}^1} \mathbb{S}^2.$$

It will be useful to write the Hopf map in terms of two complex coordinates ζ_1 and ζ_2. If we identify $\mathbb{S}^3$ with the unit sphere of $\mathbb{C}^2$, and $\mathbb{S}^2$ with the 1-point compactification of $\mathbb{C}$ via stereographic projection, we find

$$\mathbb{S}^3 = \left\{ (\zeta_1, \zeta_2) \in \mathbb{C}^2 \middle| \, |\zeta_1|^2 + |\zeta_2|^2 = 1 \right\}$$

and the Hopf map $h : S^3 \longrightarrow S^2$ can be written as the ratio

$$h\left(\zeta_1, \zeta_2\right) = \frac{\zeta_1}{\zeta_2}. \tag{2.9}$$

In this form, the fiber structure of the Hopf map is apparent since Eqn. (2.9) is invariant under the transformation $(\zeta_1, \zeta_2) \to e^{i\psi}(\zeta_1, \zeta_2)$, where $\psi \in [0, 2\pi)$ gives the parameterization of the circular fibers.

Define the stereographic projection, $ST^3 : \mathbb{R}^3 \to \mathbb{S}^3$ by

$$(x, y, z) \longrightarrow \left(\frac{2(x+iy)}{r^2+1}, \frac{2z + i\left(r^2-1\right)}{r^2+1} \right). \tag{2.10}$$

Then the map $\varphi = h \circ ST^3$ is the composition of the Hopf map in Eqn. (2.9) with stereographic projection in Eqn. (2.10) and is given by

$$\varphi(t=0, x, y, z) = \frac{2(x+iy)}{2z + i(r^2-1)}. \tag{2.11}$$

Now that we have the map φ, we can find a second map ϑ by permuting the coordinates so that

$$\begin{aligned} \vartheta(t=0, x, y, z) &= \varphi(t=0, y, z, x) \\ &= \frac{2(y+iz)}{2x + i(r^2-1).} \end{aligned} \tag{2.12}$$

A visualization of the Hopf fibration on $\mathbb{R}^3$ is shown in Figure 2.1. The inverse image of a single point on $\mathbb{S}^2$ under the Hopf map is a great circle on $\mathbb{S}^3$. The map φ gives the projection of the Hopf map onto $\mathbb{R}^3$. Stereographic projection is a conformal map, thus circles remain circles. These great circles form a special family of circles called Villarceaux circles that correspond to the integral curves of the physical fields. To understand this field structure in more detail, consider a plane intersecting $\mathbb{S}^2$ which is parallel to the equitorial plane. This intersection is

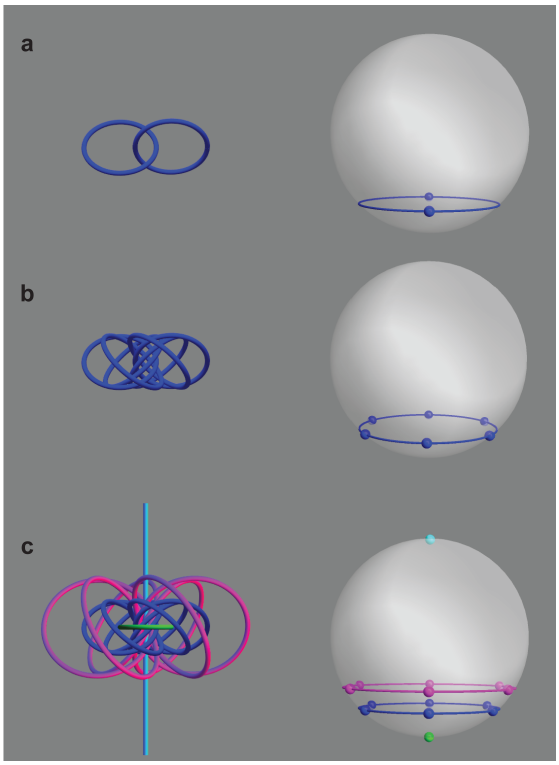

Figure 2.1: The first column shows the structure of the Hopf fibration in $\mathbb{R}^3$ and the second column shows the corresponding points in $\mathbb{S}^2$. **a** The inverse image of two points on $\mathbb{S}^2$ is two linked circles in $\mathbb{R}^3$. **b** The set of points all lying on the same circle in $\mathbb{S}^2$ corresponds to a set of circles filling out a toroidal surface in $\mathbb{R}^3$. **c** Each circle on $\mathbb{S}^2$ corresponds to a different torus in $\mathbb{R}^3$. Note that the poles of the sphere correspond to the degenerate tori.

a circle, and under the map $\varphi = constant$ any two points on it correspond to two linked circles lying on the same toroidal surface in $\mathbb{R}^3$ as in Figure 2.1a. The other points on the same circle in $\mathbb{S}^2$ correspond to linked circles on the same torus in $\mathbb{R}^3$ as in Figure 2.1b. The points on each circle in $\mathbb{S}^2$ intersecting a parallel plane fill out a different toroidal surface as in Figure 2.1c. It should be noted that at the poles the plane intersects $\mathbb{S}^2$ at a single point. In $\mathbb{R}^3$ the toroidal surfaces

become degenerate, with one pole corresponding to a circle through infinity (a line) and the other the unit circle inside the nested toriodal surfaces. This is the characteristic Hopf structure of nested tori, filled by circles that are each linked with every other circle exactly once.

2.4 EM Hopfion

2.4.1 Cauchy data

We now want to find the field of the EM hopfion at $t = 0$. We can use the maps (φ, ϑ) to construct the initial magnetic and electric fields, $\mathbf{B}_R$ and $\mathbf{E}_R$, by Eqn. (2.7) and Eqn. (2.8) respectively. Since our maps send $\mathbb{R}^3 \longrightarrow \mathbb{C}$, the area element σ should be expressed terms of a complex coordinate λ. On $\mathbb{S}^2$, we can express σ in terms of spherical coordinates

$$\sigma = \frac{1}{4\pi} d\theta \wedge d\phi$$

where we have normalized the area element so that

$$\int_{S^2} \sigma = 1.$$

Define the stereographic projection $ST^2 : S^2 \longrightarrow \mathbb{C}$ so that the complex coordinate is

$$\lambda(\theta, \phi) = \frac{\sin\theta}{1 - \cos\theta} e^{i\phi}.$$

The differential element is then

$$\begin{aligned} d\lambda &= \frac{\partial\lambda}{\partial\theta}d\theta + \frac{\partial\lambda}{\partial\phi}d\phi \\ &= \frac{e^{i\phi}}{1-\cos\theta}(i\sin\theta d\phi - d\theta) \end{aligned}$$

and its complex conjugate is

$$d\overline{\lambda} = \frac{-e^{-i\phi}}{1-\cos\theta}(i\sin\theta d\phi + d\theta).$$

Since $d\overline{\lambda}\wedge d\lambda$ is the only 2-form (up to a scale factor) on $\mathbb{C}$, σ must be proportional to $d\overline{\lambda}\wedge d\lambda$. To find the scale factor, write out $d\overline{\lambda}\wedge d\lambda$ explicitly as

$$d\overline{\lambda}\wedge d\lambda = \frac{2i\sin\theta}{(1-\cos\theta)^2}d\theta\wedge d\phi. \tag{2.13}$$

Using the fact that

$$1+\lambda\overline{\lambda} = \frac{2}{1-\cos\theta}$$

we find Eqn. (2.13) can be solved for σ. The result is

$$\sigma = \frac{1}{2\pi i}\frac{d\overline{\lambda}\wedge d\lambda}{\left(1+\lambda\overline{\lambda}\right)^2}. \tag{2.14}$$

Now we return to our original task of finding the $t=0$ expressions for $\mathbf{E}_R$ and $\mathbf{B}_R$. The magnetic field $\mathbf{B}_R$ is found from of Eqn. (2.7) giving

$$\begin{aligned} F &= \varphi^*\sigma \\ &= \frac{1}{2\pi i}\frac{d\overline{\varphi}\wedge d\varphi}{(1+\varphi\overline{\varphi})^2}. \end{aligned} \tag{2.15}$$

Writing out the coordinate expressions for the exterior derivatives and the wedge product in Eqn. (2.15) gives the Faraday tensor $F_{\mu\nu}$ as

$$F_{\mu\nu} = \frac{1}{4\pi i} \frac{\partial_\mu \varphi \partial_\nu \overline{\varphi} - \partial_\nu \varphi \partial_\mu \overline{\varphi}}{\left(1 + \varphi \overline{\varphi}\right)^2}. \tag{2.16}$$

We can calculate the components of the field strength tensor. In matrix form the result is

$$\begin{aligned} F \equiv & \begin{bmatrix} 0 & 0 & 0 & 0 \\ 0 & 0 & -B_z & B_y \\ 0 & B_z & 0 & -B_x \\ 0 & -B_y & B_x & 0 \end{bmatrix} \\ = & \begin{bmatrix} 0 & 0 & 0 & 0 \\ 0 & 0 & -\frac{4\left(-1+x^2+y^2-z^2\right)}{\pi\left(1+x^2+y^2+z^2\right)^3} & \frac{-8(x+yz)}{\pi\left(1+x^2+y^2+z^2\right)^3} \\ 0 & \frac{4\left(-1+x^2+y^2-z^2\right)}{\pi\left(1+x^2+y^2+z^2\right)^3} & 0 & \frac{-8(y-xz)}{\pi\left(1+x^2+y^2+z^2\right)^3} \\ 0 & \frac{8(x+yz)}{\pi\left(1+x^2+y^2+z^2\right)^3} & \frac{8(y-xz)}{\pi\left(1+x^2+y^2+z^2\right)^3} & 0 \end{bmatrix}. \end{aligned} \tag{2.17}$$

The electric field $\mathbf{E}_R$ is obtained similarly from the map ϑ and Eqn. (2.8), and we find

$$
\begin{aligned}
*F \quad &\equiv \quad \begin{bmatrix} 0 & 0 & 0 & 0 \\ 0 & 0 & -E_z & E_y \\ 0 & E_z & 0 & -E_x \\ 0 & -E_y & E_x & 0 \end{bmatrix} \\
&= \quad \begin{bmatrix} 0 & 0 & 0 & 0 \\ 0 & 0 & -\frac{8(y+xz)}{\pi\left(1+x^2+y^2+z^2\right)^3} & \frac{8xy-8z}{\pi\left(1+x^2+y^2+z^2\right)^3} \\ 0 & \frac{8(y+xz)}{\pi\left(1+x^2+y^2+z^2\right)^3} & 0 & -\frac{4\left(1+x^2-y^2-z^2\right)}{\pi\left(1+x^2+y^2+z^2\right)^3} \\ 0 & -\frac{8xy-8z}{\pi\left(1+x^2+y^2+z^2\right)^3} & \frac{4\left(1+x^2-y^2-z^2\right)}{\pi\left(1+x^2+y^2+z^2\right)^3} & 0 \end{bmatrix}.
\end{aligned}
$$

Recall that in Eqn. (2.12) we generated the map ϑ from the map φ by a right-handed permutation of coordinates. The resulting electromagnetic field is oriented so that E, B, and $E \times B$ form a right-handed coordinate basis at every point.

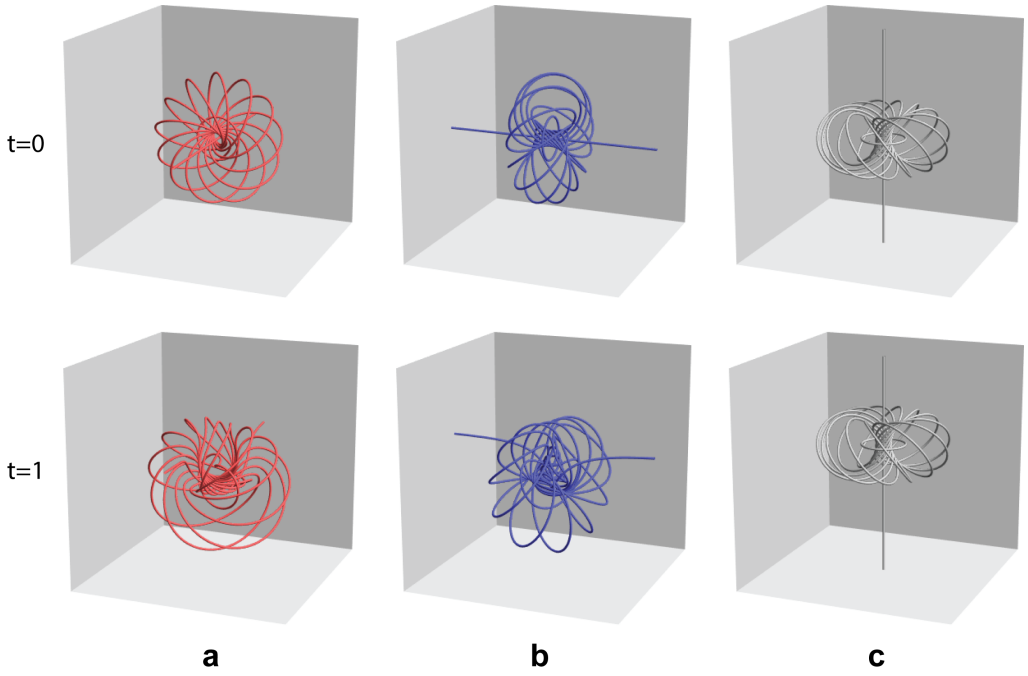

Figure 2.2: The EM hopfion: **a** the electric field, **b** the magnetic field, and **c** the Poynting vector. Row 1 shows the fields at $t = 0$ are tangent to three orthogonal Hopf fibrations. The second row shows the fields at $t = 1$ configuration, where the electric and magnetic fields have deformed, but the Poynting vector has maintained its Hopf structure while propagating at the speed of light.

2.4.2 Time-Dependent Fields

From the Cauchy data, the time-dependent form of the EM hopfion is found using Fourier analysis. The magnetic and electric fields can be expanded as

$$\mathbf{B}_R(t,\mathbf{r}) = \frac{1}{(2\pi)^{3/2}} \int d^3k \left(\mathbf{R}_1(\mathbf{k}) \cos k\cdot x - \mathbf{R}_2(\mathbf{k}) \sin k\cdot x\right) \tag{2.18}$$

$$\mathbf{E}_R(t,\mathbf{r}) = \frac{1}{(2\pi)^{3/2}} \int d^3k \left(\mathbf{R}_1(\mathbf{k}) \sin k\cdot x + \mathbf{R}_2(\mathbf{k}) \cos k\cdot x\right). \tag{2.19}$$

where $k = (\omega, \mathbf{k})$. The key to finding the time-dependent fields is to write the coefficients in the form

$$\mathbf{R}_1(\mathbf{k}) + \imath\mathbf{R}_2(\mathbf{k}) = \frac{1}{(2\pi)^{3/2}} \int d^3r \left(\mathbf{B}_R(0,\mathbf{r}) + \imath\mathbf{E}_R(0,\mathbf{r})\right) e^{\imath\mathbf{k}\cdot\mathbf{r}} \tag{2.20}$$

so that they can be calculated from the $t = 0$ fields. From the Cauchy data in Eqns. (2.17) and (2.18), we find the time-dependent fields[2]

$$\begin{aligned} \mathbf{B}_R(t,\mathbf{r}) &= \frac{1}{\pi(A^2+t^2)^3}(Q\mathbf{H}_1 + P\mathbf{H}_2) \\ \mathbf{E}_R(t,\mathbf{r}) &= \frac{1}{\pi(A^2+t^2)^3}(Q\mathbf{H}_2 - P\mathbf{H}_1) \end{aligned} \tag{2.21}$$

where we have defined the quantites A, Q, and P to be

$$A = \tfrac{1}{2}(r^2 - t^2 + 1), \quad P = t(t^2 - 3A^2), \quad Q = A(A^2 - 3t^2) \tag{2.22}$$

and the vectors $\mathbf{H}_1$ and $\mathbf{H}_2$ are

$$\begin{aligned} \mathbf{H}_1 &= \left((y+t) - xz, -x - (y+t)z, \tfrac{1}{2}(-1 - z^2 + x^2 + (y+t)^2)\right) \\ \mathbf{H}_2 &= \left(\tfrac{1}{2}(1 + z^2 + x^2 - (y+t)^2), -z + x(y+t), (y+t) + xz\right). \end{aligned} \tag{2.23}$$

By a clever guess Rañada was also able to find the maps that generate the time-dependent fields according to Eqn. (2.16). These are

$$\begin{aligned} \varphi(t,x,y,z) &= \frac{(Ax - tz) + \imath(Ay + t(A-1))}{(Az + tx) + \imath(A(A-1) - ty)} \\ \vartheta(t,x,y,z) &= \frac{Ay + t(A-1) + \imath(Az + tx)}{(Ax - tz) + \imath(A(A-1) - ty)}. \end{aligned} \tag{2.24}$$

[2]Note that we have followed the conventions of Rañada, so the EM hopfion field we calculated in this section propagates in the $-\hat{y}$-direction. A right-handed permutation of the coordinates can generate a field propagating in any direction, and most other references will choose $+\hat{z}$ as the direction of propagation.

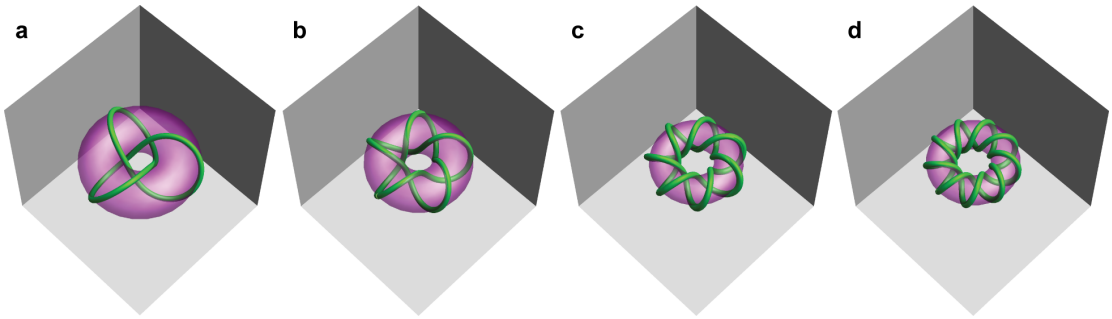

Figure 2.3: Torus knots (green) wind (n_t, n_p) times around a torus (purple) in the toroidal and poloidal directions, respectively. Shown here are the cases of **a** trefoil (2,3) knot, **b** cinquefoil (2,5) knot, **c** septafoil (2,7) knot, and **d** nonafoil (2,9) knot.

2.5 Torus Knots

One generalization of the hopfion is based on the structure of torus knots. A torus knot is a closed curve on the surface of a torus which winds an integer number of times about the toroidal direction n_t and poloidal direction n_p as in Figure 2.3, where n_t and n_p are coprime and both greater than one. If n_t and n_p are not coprime, then there are $n_g = gcd(n_t, n_p)$ linked curves, each corresponding to a (n_t, n_p) mod n_g torus knot. If either n_t or n_p is equal to one, then the knot is trivial with n_g linked curves.

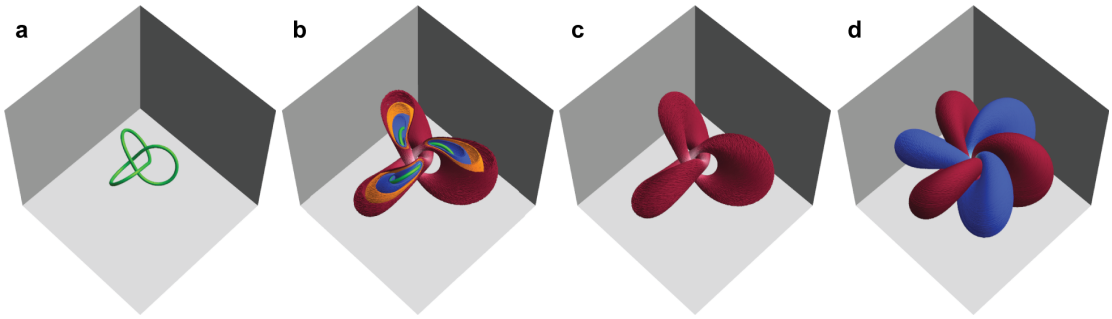

Figure 2.4: The field line structure based on (2,3) trefoil knot. **a** The core field line is a torus knot (green). **b** Each field line except the core lies on the surface of a nested, deformed torus. **c** One field line fills a complete surface (red). **d** Another field line fills a second surface (blue) linked with the first. The two linked core field lines and the nested surfaces around them fill all of space.

2.6 EM Torus Knots

The EM torus knots are constructed from the Euler potentials

$$\alpha = \frac{(r^2 - t^2 - 1) + 2\imath z}{r^2 - (t - \imath)^2} \tag{2.25}$$

$$\beta = \frac{2(x - \imath y)}{r^2 - (t - \imath)^2} \tag{2.26}$$

where $r^2 = x^2+y^2+z^2$. As Ref. [19] points out, at $t = 0$ these are the stereographic projection coordinates on $\mathbb{S}^3$. The Riemann-Silberstein vector for the fields is given by

$$\boldsymbol{F_R} = \boldsymbol{E_R} + i\boldsymbol{B_R} \tag{2.27}$$

$$= \nabla\alpha^{n_t} \times \nabla\beta^{n_p}. \tag{2.28}$$

These fields are null torus knot configurations with a Poynting vector that is everywhere tangent to a Hopf fibration and propagates in the $\hat{z}$-direction with-

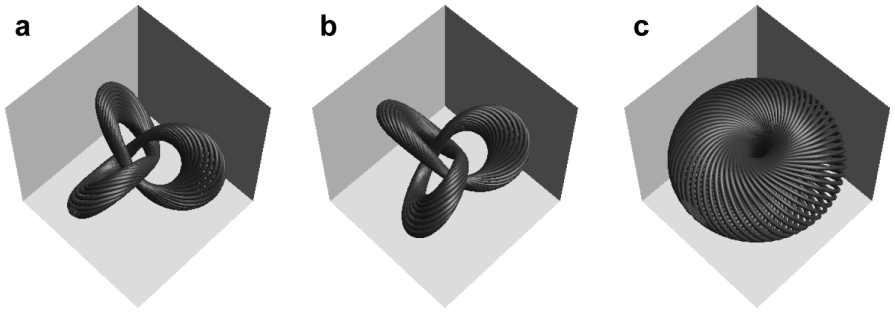

Figure 2.5: The EM trefoil knot at $t = 0$: **a** the electric field, **b** the magnetic field, and **c** the Poynting vector field.

out deformation. Each (n_t, n_p) with $n_t, n_p = 1, 2, 3...$ represents a solution to Maxwell's equations. The electric and magnetic vector fields each have the following topological structure as shown in Figure 2.4 [19]. There are $2n_g$ core field lines, where $n_g = gcd(n_t, n_p)$, which are linked (and knotted if $n_t, n_p > 1$). Each core line has the same configuration as the corresponding torus knot with (n_t, n_p) as in Figure 2.3. A single core field line is surrounded by nested, toroidal surfaces, each filled by one field line, as illustrated in Figure 2.4a-c. A second core field line, also surrounded by nested surfaces, is linked with the first so that there are $2n_g$ sets of linked nested surfaces which fill all of space as shown in Figure 2.4d. A complete solution to Maxwell's equations consists of an electric and a magnetic field orthogonal to each other, both with this field line structure as shown in Figure 2.5. The (1,1) case corresponds to the electromagnetic hopfion.

This gives the $t = 0$ configuration, where the electric and magnetic fields are tangent to orthogonal torus knots. The fields will deform under time evolution, but the topology will be conserved since $\vec{E} \cdot \vec{B} = 0$ [40, 41].

Note that the topology physically manifests in the lines of force for the vacuum EM solutions. Later we will see this also occurs in magnetic configurations in plasma, as well as vacuum solutions to Einstein's equations.

Chapter 3

Plasma Physics Background

The linked and knotted fields in the previous chapter were source-free electromagnetic solutions, but similar topological structures can be found in other areas of physics. Toroidal magnetic fields with linked and knotted field line configurations are particularly important in magnetically confined plasmas. Before discussing knots in plasma we will first review the basics of plasma physics. Our results, which are presented in the next chapter, are based on magnetohydrodynamic (MHD) theory, a model of plasma behavior that is well-suited to large-scale, highly magnetized plasma [42]. The derivation of the MHD equations involves techniques used in other plasma physics models, so first we give a review of these models which will lead into the discussion of MHD. Finally, we will examine the reason why magnetic fields with a nested toroidal configuration are found in a wide range of plasma physics applications.

3.1 Introduction to Plasma

A plasma is a medium of positive and negative charged particles that is overall electrically neutral. The particles are generally the constituents of a fluid, so they are unbound, but not free. As the charges move in the plasma they generate currents and associated fields, which in turn affect other particles. Thus, the collective behavior of a plasma has many degrees of freedom and is more easily described by models based on approximations appropriate in different regimes. The three most common models [43] will be derived in Section 3.3: Vlasov, two-fluid, and magnetohydrodynamics.

A plasma is characterized by three fundamental parameters:

- particle density n,
- temperature T, and
- steady state magnetic field $\mathbf{B}$.

There are many useful quantities that are derived from these three fundamental parameters, such as the Debye length, Larmor radius, plasma frequency, cyclotron frequency, and thermal velocity. In the case of partially ionized plasmas, the fractional ionization and the cross-section of neutral particles can also be considered fundamental for describing the fluid dynamics.

type	$n(m^{-3})$	$T(eV)$	$B(T)$
terrestrial non-fusion	$10^{14} - 10^{22}$	1	$10^{-4} - 1$
terrestrial fusion	$10^{19} - 10^{21}$	$100 - 10^{4}$	$1 - 10$
cosmic	$10^{6} - 10^{30}$	$1 - 100$	$10^{-10} - 10^{11}$

Table 3.1: Order of magnitude comparison of typical parameter values for different types of plasma.

Table 3.1 shows a comparison of typical parameters for different types of plasma, compiled from Refs. [43–49]. Terrestrial non-fusion plasmas produced in laboratories are weakly ionized and have electron temperatures of a few eV, with ion temperatures that are colder, usually about room temperature. The fields they produce are small, as is their density (compare Table 3.1 to air at STP with $n \sim 10^{25}\ m^{-3}$). Fusion plasma systems are carefully designed to have temperatures large enough to generate fully ionized hydrogen or deuterium. An externally applied magnetic field with the desired geometry is supplied by the tokamak (or spheromak) device. The magnetic confinement increases the density of the plasma. Astrophysical plasmas are generated by a wide range of sources and vary greatly. Plasmas in interstellar space are very cold and sparse, while plasmas in stellar cores and near neutron stars are hot and dense.

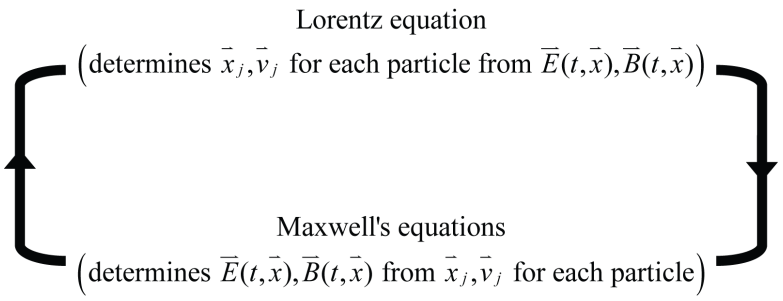

Figure 3.1: Plasma dynamics as determined by the Lorentz equation and Maxwell's equations.

3.2 Plasma Dynamics

Plasma dynamics can in principle be completely determined by the self-consistent interaction between electromagnetic fields and statistically large numbers of charged particles, as illustrated in Figure 3.1 [43]. Determining the time evolution of the plasma is conceptually simple, but computationally intensive, given by the following process:

1. If the initial trajectory $\mathbf{x}_j(t)$ and velocity $\mathbf{v}_j(t)$ for every particle j is known, Maxwell's equations determine the electric field $\mathbf{E}(\mathbf{x}, t)$ and magnetic field $\mathbf{B}(\mathbf{x}, t)$.

2. Given the instantaneous electric field $\mathbf{E}(\mathbf{x}, t)$ and magnetic field $\mathbf{B}(\mathbf{x}, t)$, the Lorentz equation determines the forces on every particle j. This information can be used to calculate the new particle trajectories and velocities.

An exact solution for plasma behavior using this iterative method is difficult to attain given the immensely large number of particles and, in some cases, the complexity of the electromagnetic fields involved. Therefore, plasma dynamics is adapted into a more tractable problem by considering specific phenomena and applying simplifying assumptions appropriate to the regime of interest.

The approximation methods most commonly used to describe plasma behavior are based on assumptions about the particle motion for some species (electrons or ions). Vlasov theory approximates particle behavior by considering the average Lorentz force over particles of a given species with the same velocity at a given location. The plasma is characterized by a distribution function $f_\sigma(\mathbf{v}, \mathbf{x},t)$ for each species σ that gives the density distribution for all particles having velocity $\mathbf{v}$ at position $\mathbf{x}$ at time t. In two-fluid theory, the average velocities are taken over particles of a given species at a given location so that one can characterize the plasma by a density $n_\sigma(\mathbf{x}, t)$, mean velocity $u_\sigma(\mathbf{x}, t)$, and pressure (relative to mean velocity) $p_\sigma(\mathbf{x}, t)$ for each particle species σ. MHD theory involves averaging the momentum over all particles of all species at a given location and the plasma is characterized by the center of mass velocity $U(\mathbf{x}, t)$ and pressure (relative to COM velocity) $p(\mathbf{x},t)$.

3.3 Plasma Models

3.3.1 Vlasov theory

Vlasov theory simplifies the description of plasma behavior by averaging the Lorentz force over all the particles of a given species that have the same velocity at a given location. Consider a phase space diagram with each of the particles in the plasma depicted by it's specific position and velocity, as in Figure 3.2. The plasma can be characterized by a distribution function $f_\sigma(\mathbf{v}, \mathbf{x}, t)$ specifying the instantaneous density of particles at each point $(\mathbf{x}, \mathbf{v})$ in phase space, so that $f_\sigma(\mathbf{v}, \mathbf{x}, t)dxdv$ represents number of particles at time t at a position in the range x to $x + dx$ and with a velocity in the range v to $v + dv$. As the system evolves in time, the velocities and accelerations of the particles cause the particles to move in phase space. Thus, the plasma behavior can be simplified by considering the time evolution of $f_\sigma(\mathbf{v}, \mathbf{x}, t)$ rather than the individual trajectories of each particle.

To derive Vlasov's equation in one dimension, consider the flux into each side of the box in Figure 3.2. If we define $a(x, v, t)$ to be the acceleration of each particle (due to the Lorentz force), then

- $f(v, x, t)vdv$ is the flux into the left side,
- $-f(v, x + dx, t)vdv$ is the flux into the right side,
- $f(v, x, t)a(x, v, t)dx$ is the flux into the bottom, and

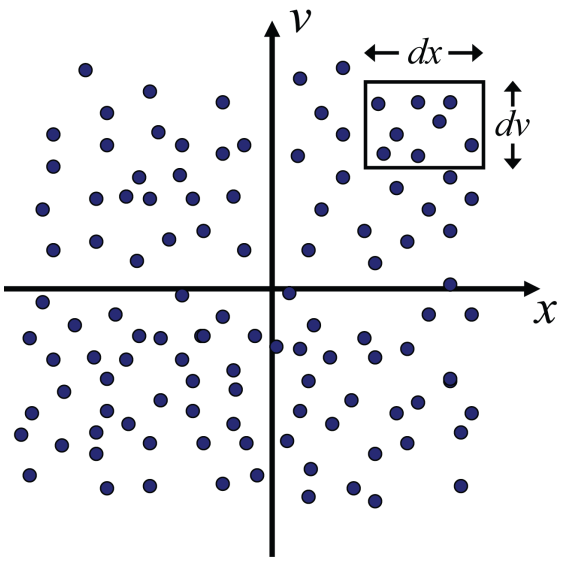

Figure 3.2: A phase space diagram for one instant in time showing the position and velocity of each particle.

- $-f(v+dv,x,t)a(x,v+dv,t)dx$ is the flux into the top.

Since $f(v,x,t)dxdv$ represents the total number of particles in the box, the rate of change of particles is

$$\begin{aligned}\frac{\partial}{\partial t}f(v,x,t)dxdv =& f(v,x,t)vdv - f(v,x+dx,t)vdv \\ &+ f(v,x,t)a(x,v,t)dx - f(v+dv,x,t)a(x,v+dv,t)dx.\end{aligned} \tag{3.1}$$

Taylor expanding each term on the right side of Eqn. (3.1) results in the Vlasov equation in one dimension

$$\frac{\partial f}{\partial t} + v\frac{\partial f}{\partial x} + \frac{\partial}{\partial v}(af) = 0. \tag{3.2}$$

By a similar analysis in three dimensions, the generalized Vlasov equation is found to be

$$\frac{\partial f}{\partial t} + \mathbf{v} \cdot \frac{\partial f}{\partial \mathbf{x}} + \frac{\partial}{\partial \mathbf{v}} \cdot (\mathbf{a} f) = 0. \tag{3.3}$$

3.3.2 Two Fluid Theory

Moments of the Distribution Function

Two fluid theory is derived by "taking moments" of the Vlasov equation. To understand this process, first consider the phase space diagram in Figure 3.3. The shaded strip represents the range x to $x + dx$. If $n(x,t)$ is the number density of particles, then $n(x,t)dx$ is the total number of particles in the shaded region (at time t). The number density is also equivalent to $n(x,t) = \int f(v,x,t)dv$, or the zeroth moment of f. Thus, the phase space description (x, v are the dependent variables) is equivalent to a position space description (x is a dependent variable), where the velocity dependence has been "integrated out" leaving a function of x only.

The mean velocity can also be calculated from the distribution function, since f represents the probability that a particle at position x and time t has velocity v. Thus, averaging over all particles gives $n(x,t)u(x,t) = \int v f(v,x,t)dv$, or the first moment of f. The process of taking moments of the distribution function can be

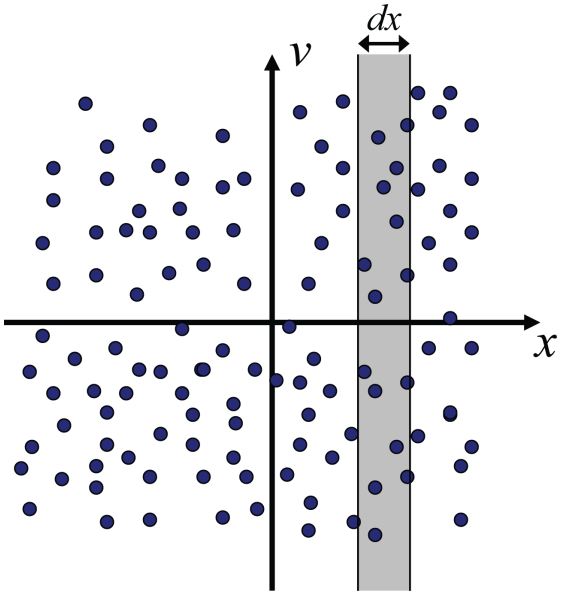

Figure 3.3: Moments are obtained by taking weighted averages over the particles in the shaded strip representing the range x to $x + dx$.

continued - the second moment $n(x,t)\varepsilon(x,t) = m\int v^2 f(v,x,t)dv$ is related to the mean energy ε of the particles, where m is the particle mass.

Similarly, in three dimensions, this process of "moment-taking", i.e. integrating $\int \mathbf{v}^j f(\mathbf{v},\mathbf{x},t)d\mathbf{v}$ for $j = 0, 1, 2, ...$ results in the following quantities:

- the density function (zeroth moment)

$$n(\mathbf{x},t) = \int f(\mathbf{v},\mathbf{x},t)d\mathbf{v},$$

- the mean velocity vector (first moment)

$$\mathbf{u}(\mathbf{x},t) = \frac{\int \mathbf{v} f(\mathbf{v},\mathbf{x},t)d\mathbf{v}}{n(\mathbf{x},t)},$$

- and the average stress tensor (second moment)

$$T(\mathbf{x},t) = \frac{\int \mathbf{v}\cdot\mathbf{v} f(\mathbf{v},\mathbf{x},t) d\mathbf{v}}{m\cdot n(\mathbf{x},t)}.$$

Two-Fluid Equations

The two-fluid model is based on taking moments of the entire Vlasov equation, rather than just the distribution function. This produces two sets of partial differential equations relating the mean number density $n_\sigma(\mathbf{x},t)$, mean velocity $\mathbf{u}_\sigma(\mathbf{x},t)$, and stress tensor T_σ, where σ represents the particle species (electrons or ions). The full derivation is lengthy, but we will list the results.

Electron Fluid Moment Equations ($\frac{d_e}{dt} \equiv \frac{\partial}{\partial t} + \mathbf{u}_e\cdot\bigtriangledown$)

$$\text{Density} \quad : \quad \frac{d_e n_e}{dt} = -n_e(\bigtriangledown\cdot\mathbf{u}_e) \tag{3.4}$$

$$\text{Momentum} \quad : \quad m_e n_e \frac{d_e \mathbf{u}_e}{dt} = -n_e e[\mathbf{E}+\mathbf{u}_e\times\mathbf{B}] - \bigtriangledown p_e \tag{3.5}$$

$$\text{Energy} \quad : \quad \frac{3}{2} n_e \frac{d_e T_e}{dt} = -n_e T_e(\bigtriangledown\cdot\mathbf{u}_e) \tag{3.6}$$

Ion Fluid Moment Equations ($\frac{d_i}{dt} \equiv \frac{\partial}{\partial t} + \mathbf{u}_i\cdot\bigtriangledown$)

$$\text{Density} \quad : \quad \frac{d_i n_i}{dt} = -n_i(\bigtriangledown\cdot\mathbf{u}_i) \tag{3.7}$$

$$\text{Momentum} \quad : \quad m_i n_i \frac{d_i \mathbf{u}_i}{dt} = -n_i Z_i e[\mathbf{E}+\mathbf{u}_i\times\mathbf{B}] - \bigtriangledown p_i \tag{3.8}$$

$$\text{Energy} \quad : \quad \frac{3}{2} n_i \frac{d_i T_i}{dt} = -n_i T_i(\bigtriangledown\cdot\mathbf{u}_i) \tag{3.9}$$

where Z_i is the ion atomic number, $\mathbf{E}$ and $\mathbf{B}$ are the electric and magnetic fields, and p_σ is the scalar pressure. We have also used that the acceleration due to

the Lorentz force is $\frac{q_\sigma}{m}[\mathbf{E} + \mathbf{u}_\sigma \times \mathbf{B}]$. The two-fluid equations sometimes include terms for the frictional force between particles $R \sim (\mathbf{u}_e - \mathbf{u}_i)$ or energy exchange $Q \sim (T_e - T_i)$, where T_σ is the temperature of each species, but these can be neglected in most systems. It should also be noted that the equations for the zeroth moment are equivalent to the continuity equation, since the convective derivative is $\frac{d_\sigma}{dt} \equiv \frac{\partial}{\partial t} + \mathbf{u}_\sigma \cdot \bigtriangledown$, so that

$$\frac{d_\sigma n_\sigma}{dt} = -n_\sigma(\bigtriangledown \cdot \mathbf{u}_\sigma) \Longleftrightarrow \frac{\partial n_\sigma}{\partial t} + \bigtriangledown \cdot (n_\sigma \mathbf{u}_\sigma) = 0. \tag{3.10}$$

3.3.3 Magnetohydrodynamics

Magnetohydrodynamics is a model of plasma behavior based on the center of mass quantities for all particles (both ions and electrons). In two-fluid theory, the particle motion was described by the mean velocity of each separate species $\mathbf{u}_i$, $\mathbf{u}_e$. In MHD, two new "velocity-like" variables are defined that are each a linear combination of $\mathbf{u}_i$ and $\mathbf{u}_e$. This description also requires that we use the center of mass pressure p. The first new variable is the current density, which describes the relative velocity between ions and electrons

$$\mathbf{J} = \sum_\sigma n_\sigma q_\sigma \mathbf{u}_\sigma$$

and the second new variable is the center of mass velocity

$$\mathbf{U} = \frac{1}{\rho} \sum_\sigma m_\sigma n_\sigma \mathbf{u}_\sigma$$

where the total mass density is

$$\rho = \sum_{\sigma} m_{\sigma} n_{\sigma}.$$

The MHD equations can be derived from the Vlasov model, in a similar manner to the two-fluid equations. Again, moments of the Vlasov equation are taken, but they are now averaged over the momentum of all particles, by first multiplying by m_σ and summing over the particle species σ before integrating over velocity. For example, the first moment of the Vlasov equation, with the acceleration due to the Lorentz force, is given by the integral

$$\begin{aligned} \frac{\partial}{\partial t} \sum_{\sigma} m_{\sigma} \int \mathbf{v} f_{\sigma}(\mathbf{v}, \mathbf{x}, t) d\mathbf{v} + \frac{\partial}{\partial \mathbf{x}} \cdot \sum_{\sigma} \int m_{\sigma} \mathbf{v} \cdot \mathbf{v} f_{\sigma}(\mathbf{v}, \mathbf{x}, t) d\mathbf{v} \\ + \sum_{\sigma} q_{\sigma} \int \mathbf{v} \frac{\partial}{\partial \mathbf{v}} \cdot [(\mathbf{E} + \mathbf{v} \times \mathbf{B}) f_{\sigma}(\mathbf{v}, \mathbf{x}, t)] = 0. \end{aligned} \tag{3.11}$$

The details of the integration are not shown here, but the results can be summarized as follows:

Center of Mass Fluid Moment Equations

$$\text{Continuity Equation} \quad : \quad \frac{\partial \rho}{\partial t} + \bigtriangledown \cdot (\rho \mathbf{U}) = 0 \tag{3.12}$$

$$\text{Momentum} \quad : \quad \rho \left(\frac{\partial}{\partial t} + \mathbf{U} \cdot \bigtriangledown \right) \mathbf{U} = \mathbf{J} \times \mathbf{B} - \bigtriangledown p + \mathbf{F} \tag{3.13}$$

$$\text{Energy} \quad : \quad \frac{d}{dt} \left(\frac{p}{\rho^{\gamma}} \right) = (\gamma - 1) \eta J^2 \tag{3.14}$$

Maxwell's Equations

$$\text{Faraday's Law} \quad : \quad \bigtriangledown \times \mathbf{E} = -\frac{\partial \mathbf{B}}{\partial t} \tag{3.15}$$

$$\text{Ampere's Law} \quad : \quad \bigtriangledown \times \mathbf{B} = \mu \mathbf{J} \tag{3.16}$$

$$\text{Ohm's Law} \quad : \quad \mathbf{E} + \mathbf{U} \times \mathbf{B} = \eta \mathbf{J} \tag{3.17}$$

where $\gamma = (N+2)/N$, N is the number of dimensions of the system, and η is the plasma's electrical resistivity (or equivalently, the magnetic diffusivity). The term $\mathbf{F} = \left(\sum_{\sigma} n_\sigma q_\sigma \right) \mathbf{E}$ is usually neglected in MHD, since over large spatial scales the plasma is effectively neutral and thus $\sum_{\sigma} n_\sigma q_\sigma = 0$.

The *ideal* MHD regime occurs when resistive effects are negligible, and thus the $\eta \mathbf{J}$ term is small compared to the other terms in Ohm's Law and can be effectively ignored. In such cases, the plasma is considered to be perfectly conducting.

3.4 Toroidal Fields in Plasma

It is important to mention the special role of toroidal topology in plasma physics. Toroidal magnetic fields are ubiquitous in plasma physics, and are found in many physical systems from stars to fusion reactors. The reason this specific field topology is so often found in magnetized plasma can be expressed as a special case of the Poincaré-Hopf Theorem. It is straightforward to show that the

magnetic surfaces form a family of nested toroidal surfaces in the magnetostatic case, but the result also holds for fields in steadily diffusing plasma [50].

A plasma in static equilibrium is described by the equations

$$\nabla p = \mathbf{j} \times \mathbf{B} \tag{3.18}$$

$$\nabla \times \mathbf{B} = \mathbf{j} \tag{3.19}$$

$$\nabla \cdot \mathbf{B} = 0 \tag{3.20}$$

where $\mathbf{B}$ is the magnetic field, $\mathbf{j}$ is the current, and p is the scalar pressure. Taking the dot product of $\mathbf{B}$ and Eqn. (3.18) yields the condition

$$\mathbf{B} \cdot \nabla p = 0. \tag{3.21}$$

Thus, each magnetic surface corresponds to a constant pressure surface, given by $p = P$ [51].

The Ponicaré-Hopf Theorem relates the number of zeroes of a vector field on a manifold to the Euler characteristic of the manifold. A formal statement follows

> **Theorem.** Let M be a compact orientable differentiable manifold. Let $\mathbf{v}$ be a vector field on M with isolated zeroes. If M has boundary, then we insist that $\mathbf{v}$ be pointing in the outward normal direction along the boundary. Then we have the formula
>
> $$\sum_i index_{\mathbf{v}}(x_i) = \chi(M)$$
>
> where the sum of the indices is over all the isolated zeroes of $\mathbf{v}$ and $\chi(M)$ is the Euler characteristic of M.

For a surface of constant pressure that lies in a bounded volume of space and has no edges, if the vector field (either $\mathbf{B}$ or $\mathbf{j}$) vanishes nowhere on the surface,

then we have $\chi(M) = 0$. The only manifold that has $\chi(M) = 0$ and is realizable in physical space is a torus. (A Klein bottle or a Möbius strip are non-physical manifolds with $\chi(M) = 0$.) The proof of this theorem is quite long, but it is possible to get some intuition for where it comes from by examining a manifold with $\chi(M) \neq 0$ such as a sphere. A common analogy is to think of the vector field lines along a given constant pressure surface as strands of hair. On a spherical surface, all the hair cannot lay flat on the surface at every point. There must always be at least one point from which the hair spirals out. (Actually two points on a sphere, so that $\chi(M) = 2$.) At these points Eqn. (3.18) is not satisfied. In other words, there is no smooth vector field on a topological sphere with no sources or sinks, but it is possible for such a field to exist on a torus.

Thus, if we seek a non-trivial magnetic field topology, the field lines must lie on nested toroidal surfaces. We will find in the next chapter that these toroidal fields also possess field lines that wind around the toroidal surfaces in linked and knotted configurations.

Chapter 4

Knotted Fields in Plasma

We present a class of topological plasma configurations characterized by their toroidal and poloidal winding numbers, n_t and n_p respectively. The special case of $n_t = 1$ and $n_p = 1$ corresponds to the Kamchatnov-Hopf soliton, a magnetic field configuration everywhere tangent to the fibers of a Hopf fibration so that the field lines are circular, linked exactly once, and form the surfaces of nested tori. We show that for $n_t \in \mathbb{Z}^+$ and $n_p = 1$ these configurations represent stable, localized solutions to the magnetohydrodynamic equations for an ideal incompressible fluid with infinite conductivity. Furthermore, we extend our stability analysis by considering a plasma with finite conductivity and estimate the soliton lifetime in such a medium as a function of the toroidal winding number. We will also discuss the evolution of these fields in simulations using full resistive MHD.

4.1 Topological Solitons in Condensed Matter Systems

Hopfions have been shown to represent localized topological solitons in many areas of physics - as a model for particles in classical field theory [3], fermionic solitons in superconductors [52], particle-like solitons in superfluid-He [16], knot-like solitons in spinor bose-einstein (BE) condensates [17] and ferromagnetic materials [53], and topological solitons in MHD [5]. The Hopf fibration can also be used in the construction of finite-energy radiative solutions to Maxwell's equations and linearized Einstein's equations [10,11]. Some examples are Ranada's null EM hopfion [7,18] and its generalization to torus knots [8,19,54].

Topological solitons are metastable states. They are not in an equilibrium, or lowest energy state, but are shielded from decay by a conserved topological quantity. The energy E is a function of a scale factor, typically the size R of the soliton, so that the field could decrease its energy by changing this parameter. However, the topological invariant fixes the length scale and thus the energy. In condensed states (superconductors, superfluids, BE condensates, and ferromagnets) the topological structure is physically manifested in the order parameter, which is associated to a topological invariant. For example, the hopfion solutions in ferromagnets are such that the Hopf fibers correspond to the integral curves of

the magnetization vector $\vec{m}$. The associated Hopf invariant is equal to the linking number of the integral curves of $\vec{m}$.

For many systems the solution can still decay by a continuous deformation while conserving the topological invariant. Another physical stabilization mechanism is needed to inhibit collapse [55]. For example, this can be achieved for superconductors with localized modes of a fermionic field [56], for superfluids by linear momentum conservation [16], for BE condensates with a phase separation from a second condensate [57], and for ferromagnets with conservation of the spin projection S_z [58].

4.2 Topological Solitons in MHD

In MHD, the topological structure is present in the magnetic field. The topological soliton of Kamchatnov has a magnetic field everywhere tangent to a Hopf fibration, so that the integral curves of the magnetic field lie on nested tori and form closed circles that are linked exactly once. The Hopf invariant is equal to the linking number of the integral curves of the magnetic field, which is proportional to the magnetic helicity. In addition to the topological invariant, another conserved quantity is required. MHD solitons can be stabilized if the magnetic field has a specific angular momentum configuration which will be discussed below.

Because of the importance of topology in plasma dynamics, there has previously been interest in generalizing the Kamchatnov-Hopf soliton [59]. The topology of field lines has been shown to be related to stability of flux tube configurations, with the helicity placing constraints on the relaxation of magnetic fields in plasma [60, 61]. Magnetic helicity gives a measure of the structure of a magnetic field, including properties such as twisting, kinking, knotting, and linking [38, 62]. Simulations have shown that magnetic flux tubes with linking possess a longer decay time than similar configurations with zero linking number [63–65]. Recently, higher order topological invariants have been shown to place additional constraints on the evolution of the system [60, 66, 67]. The work presented in this chapter distinguishes itself from these topological studies of discrete flux tubes in the sense that we are considering the topology and stability of continuous, space-filling magnetic field distributions. Furthermore, for the ideal case our results are analytic, rather than based on numerical simulations.

There are many applications where magnetic field topology has a significant effect on the stability and dynamics of plasma systems. For example, toroidal magnetic fields increase confinement in fusion reactors [68, 69], and solving for the behavior of some magnetic confinement systems is only tractable in a coordinate system based on a known parameterization of the nested magnetic surface topology [69–71]. In astrophysics, the ratio of the toroidal and poloidal winding of the internal magnetic fields impacts many properties of stars, including

the shape [72, 73] and momentum of inertia [74], as well as the gravity wave signatures [75] and disk accretion [76] of neutron stars. The new class of stable, analytic MHD solutions presented in this chapter may be of use in the study of fusion reactions, stellar magnetic fields, and plasma dynamics in general.

The MHD topological soliton is intimately related to the radiative EM hopfion solution. The EM hopfion constructed by Rañada is a null EM solution with the property that the electric, magnetic, and Poynting vector fields are tangent to three orthogonal Hopf fibrations at $t = 0$. The electric and magnetic fields deform under time evolution, but their field lines remain closed and linked with linking number one. The Hopf structure of the Poynting vector propagates at the speed of light *without deformation*. The EM hopfion has been generalized to a set of null radiative fields based on torus knots with an identical Poynting vector structure [19]. The electric and magnetic fields of these toroidal solutions have integral curves that are not single rings, but rather each field line fills out the surface of a torus.

The time-independent magnetic field of the Kamchatnov-Hopf soliton is the magnetic field of the radiative EM hopfion at $t = 0$

$$\mathbf{B}_{\text{soliton}}(\mathbf{x}) = \mathbf{B}_{\text{hopfion}}(t = 0, \mathbf{x}). \tag{4.1}$$

The soliton field is then sourced by a stationary current

$$\mathbf{j}(\mathbf{x}) = \frac{1}{\mu_0} \nabla \times \mathbf{B}_{\text{soliton}}(\mathbf{x}). \tag{4.2}$$

We will use this relationship, along with the generalization of the EM hopfion to toroidal fields of higher linking number, in order to generalize the Kamchatnov-Hopf topological soliton to a class of stable topological solitons in MHD. We will also discuss how the helicity and angular momentum relate to the stability of these topological solitons.

4.3 Generalization of Kamchatnov-Hopf Soliton

We construct the generalized topological soliton fields using Eqns. (4.1) and (4.2) applied to the null radiative torus knots. The time-independent magnetic field of the soliton is identical to the magnetic field of the radiative torus knots at $t = 0$. The magnetic field is sourced by a current, resulting in a stationary solution.

The torus knots are constructed from the Euler potentials in Eqns. (2.25) and (2.26)

$$\alpha = \frac{(r^2 - t^2 - 1) + 2\imath z}{r^2 - (t - \imath)^2}$$
$$\beta = \frac{2(x - \imath y)}{r^2 - (t - \imath)^2}$$

where $r^2 = x^2 + y^2 + z^2$. The magnetic field of the torus knots is obtained from the Euler potentials for the Riemann-Silberstein vector $\mathbf{F} = \mathbf{E} + \imath\mathbf{B}$.[1]

[1]Note that the Riemann-Silberstein construction is a non-standard use of Euler potentials. We are following the method in Ref. [19].

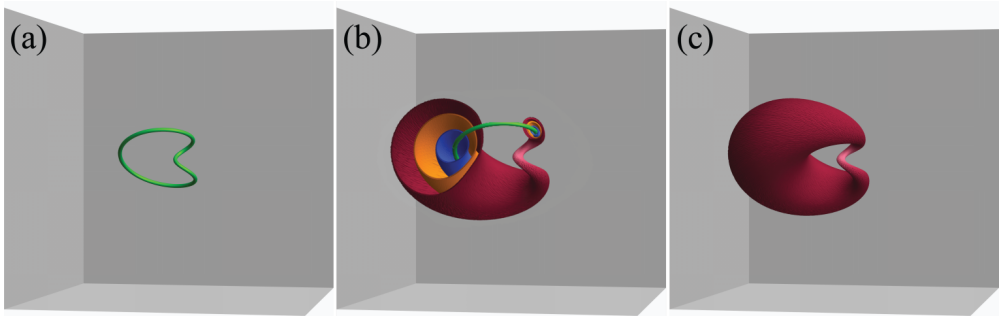

Figure 4.1: One lobe of the field configuration for $n_p = 1$ and $n_t = 2$. (a) A single, closed core magnetic field line. (b) The core field line is surrounded by nested toroidal surfaces, shown in cross section. (c) A complete magnetic surface filled entirely by one field line.

The solitons are found by taking the magnetic field of the torus knots at $t = 0$

$$\mathbf{B} = Im[\nabla\alpha^{n_t} \times \nabla\beta^{n_p}] \mid_{t=0} . \tag{4.3}$$

Each (n_t, n_p) with $n_t, n_p = 1, 2, 3...$ represents a solution to Maxwell's equations. A single magnetic field line fills the entire surface of a torus. These tori are nested and each degenerates down to a closed core field line that winds n_t times around the toroidal direction and n_p times around the poloidal direction, as illustrated in Figure 4.1. A complete solution for a given (n_t, n_p) is composed of pairs of these nested surfaces that are linked and fill all of space as shown in Figure 4.2. For $n_g = gcd(n_t, n_p)$, the solution is a magnetic field with $2n_g$ linked core field lines (knotted if $n_t > 1$ and $n_p > 1$). If $n_t = 1$ and $n_p = 1$, the solution is the Kamchatnov-Hopf soliton.

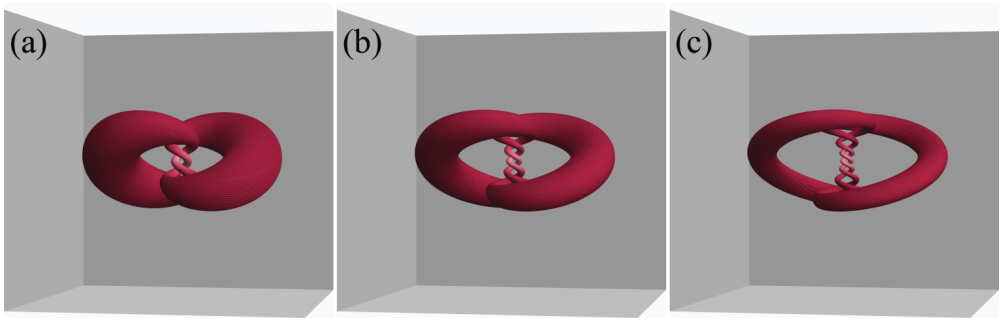

Figure 4.2: Topological solitons in MHD with $n_p = 1$ and (a)$n_t = 2$, (b)$n_t = 3$, and (c)$n_t = 4$. A single magnetic field line fills out each of the linked, toroidal surfaces.

We will analyze these fields and how the linking of field lines affects the stability of magentic fields in plasma. In particular, for $n_p = 1$ and $n_t \in \mathbb{Z}^+$, we will show that these fields can be used to construct a new class of stable topological solitons in ideal MHD. The solutions with $n_p \neq 1$ are not solitons in plasma, and their instability will be discussed in Section 4.4.1.

4.4 Stability Analysis

In this section we assume the plasma is an ideal, perfectly conducting, incompressible fluid. In a fluid with finite conductivity, the magnetic field energy diffuses. Under this condition, one can estimate the lifetime of the soliton as will be shown in Section 4.5.

First we consider the case where the poloidal winding number $n_p = 1$ and the toroidal winding number n_t is any positive integer. These will be shown to

represent stable topological solitons in ideal MHD. In the next section, we will consider the solutions with $n_p \neq 1$. Using the method in this chapter, these do not represent stable solitons, and we will discuss how this instability relates to the angular momentum.

To analyze the stability of these solutions, following the stability analysis in Ref. [5][2], we study the two scaled quantities of the system - the length scale R which corresponds to the size of the soliton and B_0 which is the magnetic field strength at the origin. (The length scale R is also the radius of the sphere $\mathbb{S}^3$ before stereographic projection.) First we change to dimensionful coordinates by taking

$$\{x, y, z\} \rightarrow \{\tfrac{x}{R}, \tfrac{y}{R}, \tfrac{z}{R}\} \tag{4.4}$$

$$|\mathbf{B}\,(0,0,0)\,| = B_0. \tag{4.5}$$

The stability depends on three quantities - energy, magnetic helicity, and angular momentum - which are functions of R and B_0. For a perfectly conducting plasma, the magnetic helicity h_m is an integral of motion and is thus conserved. The magnetic helicity is also a topological invariant proportional to the linking number of the magnetic field lines. If the field can evolve into a lower energy state by a continuous deformation (therefore preserving the topological invariant) then it will be unstable. However, we will show that such a deformation does not exist

[2]Note that Ref. [5] uses CGS units and we use SI units in our analysis. The reference also has a typo - Eqn. (45) should have a factor of R^2 instead of R.

because the angular momentum M is also conserved and serves to inhibit the spreading of the soliton.

The magnetic helicity is defined as

$$h_m = \int \mathbf{A} \cdot \mathbf{B} d^3x \tag{4.6}$$

where $\mathbf{A} = Im[\alpha^{n_t} \nabla \beta^{n_p}] \mid_{t=0}$ is the vector potential. From Eqns. (2.25)-(4.3), it follows that

$$h_m = \frac{2n_t}{(n_t+1)} \pi^2 B_0^2 R^4. \tag{4.7}$$

The MHD equations for stationary flow are satisfied for a fluid with velocity

$$\mathbf{v} = \pm \frac{\mathbf{B}}{(\mu_0 \rho)^{\frac{1}{2}}}. \tag{4.8}$$

The energy of the soliton is given by

$$\begin{aligned} E &= \int \left(\frac{\rho v^2}{2} + \frac{B^2}{2\mu_0} \right) d^3x \\ &= \int \frac{B^2}{\mu_0} d^3x \end{aligned} \tag{4.9}$$

so that

$$\begin{aligned} E &= \frac{2n_t \pi^2}{\mu_0} B_0^2 R^3 \\ &\propto \frac{h_m}{R}. \end{aligned} \tag{4.10}$$

The angular momentum is

$$\begin{aligned}\mathbf{M} =& \rho \int [\mathbf{x} \times \mathbf{v}] d^3x \\ =& \left(\frac{\rho}{\mu_0}\right)^{1/2} 4n_t \pi^2 B_0 R^4 \hat{y}\end{aligned} \tag{4.11}$$

where we took the positive velocity solution. We find that the conserved quantities h_m and $\mathbf{M}$ fix the values of R and B_0,

$$\begin{aligned}R =& \left(\frac{1}{8\pi^2 n_t(n_t+1)} \left(\frac{\mu_0}{\rho}\right) \frac{|M|^2}{h_m}\right)^{\frac{1}{4}}, \\ B_0 =& 2n_t(n_t+1) \left(\frac{\rho}{\mu_0}\right)^{1/2} \frac{h_m}{|M|},\end{aligned} \tag{4.12}$$

thus inhibiting energy dissipation. This shows that the solution given in Eqns. (2.25)-(4.3) (and shown in Figure 4.2) represents a class of topological solitons characterized by the parameter $n_t \in \mathbb{Z}^+$ for $n_p = 1$.

4.4.1 Angular Momentum and Instability for $n_p \neq 1$

For $n_p \neq 1$, the angular momentum for all n_t is zero. Some examples of fields with $n_t = 1$ and different n_p values are shown in Figure 4.3. The field lines fill two sets of linked surfaces. For a given pair of linked surfaces, the field in each lobe wraps around the surface in opposite directions. In Figure 4.3 the red and blue surfaces wind in opposite directions. This means that the contribution to the angular momentum of the two field lines cancels. In this case the length scale

is not fixed by the conserved quantities. The energy can therefore decrease by increasing the radius and the fields are not solitons.

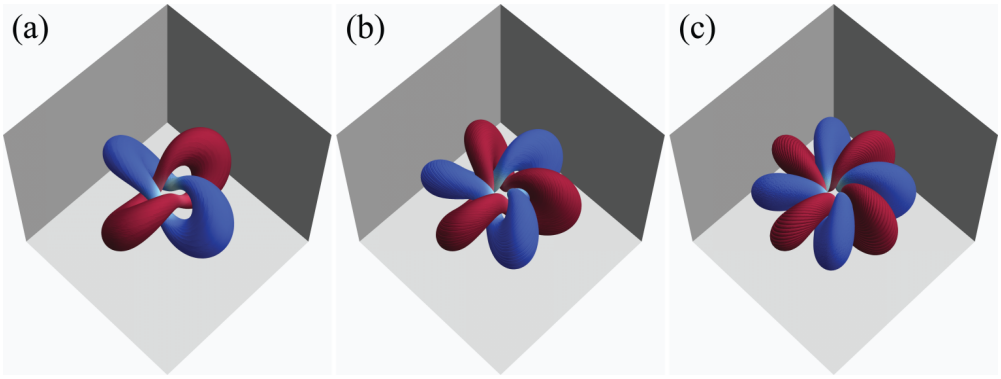

Figure 4.3: The magnetic surfaces for $n_t = 1$ and (a)$n_p = 2$, (b)$n_p = 3$, and (c)$n_p = 4$. Solutions with $n_p \neq 1$ have zero angular momentum and are therefore not stable solitons. The magnetic field lines in each lobe wind in opposite directions, represented by the red and blue surfaces.

4.5 Finite Conductivity and Soliton Lifetime

To include losses due to diffusion, we need to consider a plasma with finite conductivity. We can estimate the soliton lifetime by dividing the energy by dE/dt, calculated before any energy dissipation [5]. Since this is the maximum rate of energy dissipation, we can obtain a lower bound on the time it takes for the total energy to dissipate. Thus,

$$\frac{dE}{dt} = \frac{1}{\sigma}\int j^2 d^3x \tag{4.13}$$

$$= (3n_t + 7n_t^2 + 5n_t^3)\frac{\pi^2 B_0^2 R}{\mu_0^2 \sigma}. \tag{4.14}$$

The resulting lifetime is

$$t_{n_t} \geq \frac{3n_t}{3n_t + 7n_t^2 + 5n_t^3}\mu_0 \sigma R^2. \tag{4.15}$$

For higher n_t, the lifetime decreases although the helicity in Eqn. (4.7) increases. This result is interesting as we would have expected from the results regarding flux tubes mentioned previously that the lifetime would increase with increasing helicity.

4.6 Numerical Methods

The new class of solitons described here is completely stable in ideal MHD. The next step is to numerically study their stability in a resistive, compressible, and viscous plasma. I would like to acknowledge Chris B. Smiet for working with me to study the stability of these solitons in full MHD and running the simulations.

The simulations were done with Pencil Code [77], which solves the full MHD equations using finite-difference methods to sixth-order in space and third-order in time. We assume an isothermal plasma, thus we take the background pressure to be the pressure for an isothermal gas $p = \rho c_s^2$, where ρ is the density and c_s^2 is the speed of sound.

The equation of motion for an isothermal plasma is

$$\frac{D\mathbf{U}}{Dt} = -c_s^2 \nabla \ln \rho + \mathbf{J} \times \mathbf{B}/\rho + \mathbf{F}_{\text{visc}} \tag{4.16}$$

where $\mathbf{U}$ is the fluid velocity and $\frac{D}{Dt} \equiv \frac{\partial}{\partial t} + \mathbf{U} \cdot \nabla$ is the convective derivative, which represents the rate of change of a quantity as experienced by an observer that is moving with the flow. The viscous force is

$$\mathbf{F}_{\text{visc}} = \rho^{-1} \nabla \cdot 2\nu\rho\mathbf{S}$$

where ν is the kinematic viscosity and $\mathbf{S}$ is the traceless rate of strain tensor

$$S_{ij} = \tfrac{1}{2}(U_{i,j} + U_{j,i}) - \tfrac{1}{3}\delta_{ij} \nabla \cdot \mathbf{U}.$$

The continuity equation $\partial\rho/\partial t + \nabla \cdot \rho\mathbf{U} = 0$ in terms of the logarithmic density has the form

$$\frac{D \ln \rho}{Dt} = -\nabla \cdot \mathbf{U}. \tag{4.17}$$

The induction equation

$$\frac{\partial \mathbf{B}}{\partial t} = \nabla \times (\mathbf{U} \times \mathbf{B} - \eta\mathbf{J})$$

can be written terms of the vector potential as

$$\frac{\partial \mathbf{A}}{\partial t} = \mathbf{U} \times \mathbf{B} + \eta \nabla^2 \mathbf{A} \tag{4.18}$$

where η is the magnetic diffusivity, which we have assumed to be constant and is related to the electrical conductivity σ by $\eta = 1/(\mu_0\sigma)$. The code solves Eqns. (4.16), (4.17), and (4.18) for $\mathbf{U}$, ρ, and $\mathbf{A}$, from which the magnetic field is calculated by $\mathbf{B} = \nabla \times \mathbf{A}$.

Eqn. (4.18) assumes that the vector potential is in the resistive gauge, so that the divergence of $\mathbf{A}$ generates a resistive term

$$A_0 = \eta \nabla \cdot \mathbf{A} \tag{4.19}$$

where A_0 is the electrostatic potential. Choosing this gauge removes an extra term from the induction equation, which is equivalent to putting a constraint on the components of the vector potential that stabilizes the diffusion of $\mathbf{A}$ in the numerical simulations [78]. Although Pencil Code has built-in functionality for several different gauge choices, the resistive gauge is typically the most convenient for numerical reasons [79, 80]. Studies of magnetic helicity flux have shown that the results of simulations performed with Pencil Code in different gauges produce the same results [80].

The simulation domain is a square box of size $(2\pi)^3$ with 256^3 meshpoints. All quantities are measured in dimensionless units, where the density is scaled by units of the initial density ρ_0, speed by the isothermal speed of sound c_s, the magnetic field by $(\mu_0 \rho_0 c_s^2)^{1/2}$, and length by units of $1/k$, where $k = (2\pi/L)$ is the smallest wavenumber that will fit into the box length L. This also gives time is in dimensionless units.[3]

The boundary is taken to be perfectly conducting, so that $\mathbf{B} \cdot \hat{n} = 0$ where $\hat{n}$ is the vector normal to the simulation boundary. This is implemented in the

[3]For example, if one chooses SI units then the wavenumber is $k = 1$ meters^{-1}, the box has side length $L = 2\pi$ meters, and each unit of time is one second.

code by fixing the two tangential components of the vector potential $\mathbf{A}$ at the boundary to be zero. In ideal MHD, this boundary condition would ensure that the magnetic helicity is conserved (and also gauge invariant) since the magnetic field lines do not have endpoints on the boundary. Thus, in our simulations any changes in h_m are due to the resistive term $-\eta\mathbf{J}$ in the induction equation.

4.7 Topological Solitons in Simulations

The preliminary results of simulations for a field with the $(2, 1)$ soliton as its initial configuration are presented here. Figure 4.4 shows a plot of the average magnetic field energy (normalized to the energy at $t = 0$), average normalized helicity (helicity divided by the magnetic field energy), and average helicity (normalized to the helicity at $t = 0$). These quantities are shown as a function of time for $t = 0$ to $t = 250$. The average magnetic field strength and average helicity first decrease rapidly then stabilize, indicating that there is an initial fast reconnection phase during which the topology changes rapidly. Then the field reaches a state with a slow decay in the energy and a slow change in topology. The magnetic helicity should limit the decay of the field energy [81], and indeed we see that the helicity normalized to energy initially increases then levels off. This shows that the field decays more rapidly than the helicity at the beginning but then they decay steadily at a similar rate.

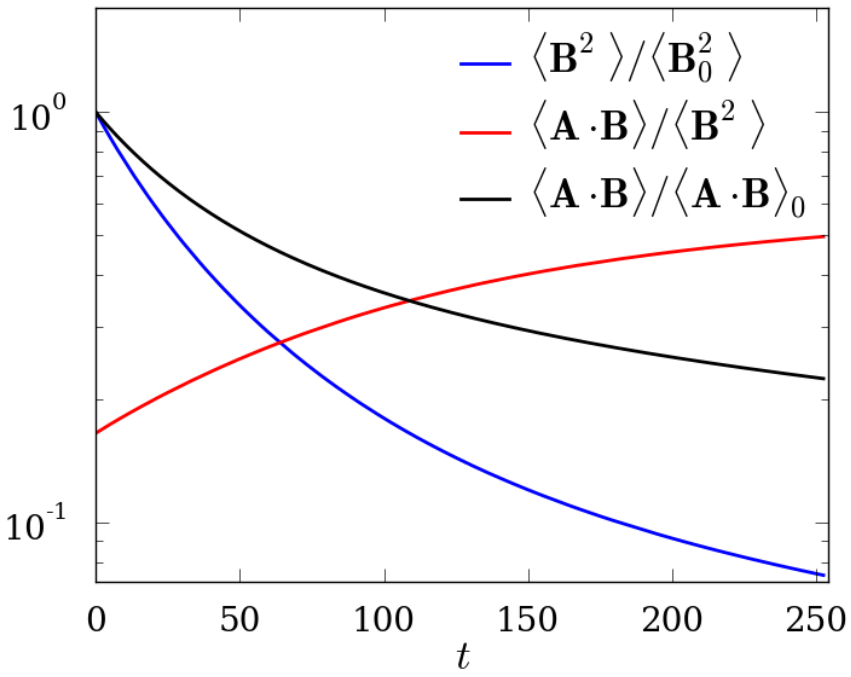

Figure 4.4: The results from a numerical simulation of the $n_t = 2$ and $n_p = 1$ topological soliton. The plot shows the average magnetic field strength (blue), average normalized helicity (red), and average helicity (black) as a function of time.

To examine this process in more detail, consider Figure 4.5 which shows snapshots of the magnetic field lines of the $(2, 1)$ soliton during the early reconnection phase, at time steps from $t = 0$ to $t = 62$. The soliton initially has a double toroidal structure with field lines that lie on linked pairs of nested surfaces, or more specifically Figure 4.5a has the same structure as Figure 4.2a. Then the field reconfigures itself and by $t = 24$ (Figure 4.5e) the double toroidal structure begins to deteriorate as the linking of the field lines begins to break. By $t = 62$

(Figure 4.5g) the field has settled into a structure with single toroidal surfaces. After this point, the variation in the field for each time step is small. This suggests that perhaps there are other solutions based on single toroidal topologies with greater stability in realistic plasma systems. Currently, we are working on generating new classes of topological solitons in ideal MHD and using both analytic and numerical methods to investigate their stability.

4.8 Summary

We have constructed a new class of topological solitons in plasma, which consist of two linked core field lines surrounded by nested tori that fill all of space. The solitons are characterized by the toroidal winding number of the core field lines and have poloidal winding number one in order to have non-zero angular momentum. We have shown that the conservation of linking number and angular momentum give stability to the solitons in the ideal case. We are currently studying the stability of these solutions in a resistive plasma using numerical simulations. Finally, we note that there may be related generalizations of the hopfion fields in other physical systems, such as superfluids, Bose-Einstein condensates, and ferromagnetic materials.

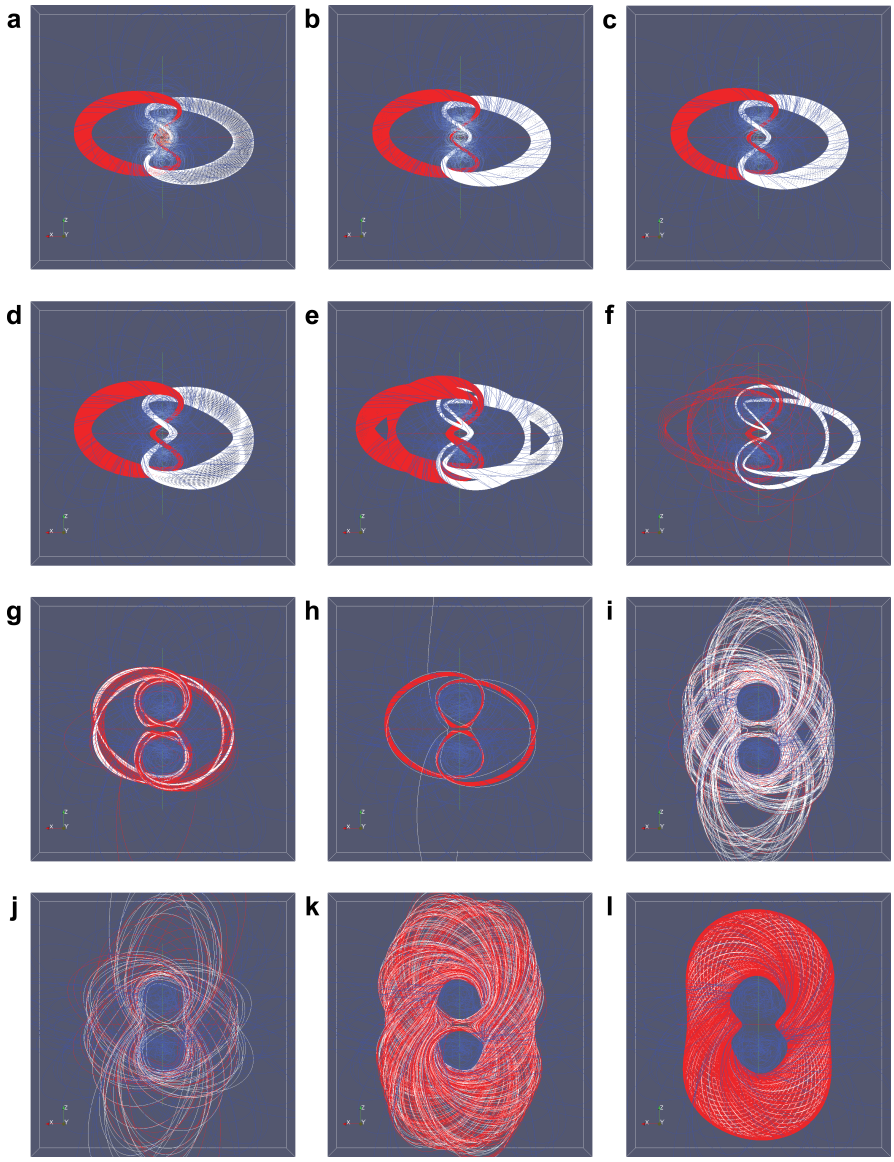

Figure 4.5: A numerical simulation of the topological soliton with winding numbers $n_t = 2$ and $n_p = 1$. The magnetic field lines are shown for **a-k** $t = 0$ to $t = 60$ with time steps of $\Delta t = 6$, and **l** $t = 62$ (note the last time step is shorter). The double toroidal configuration undergoes a fast reconnection phase and quickly settles into a structure with single toroidal surfaces. Future time steps involve only small variations in the field structure.

Chapter 5

Spinors

The second part of this thesis will focus on generalizing linked and knotted electromagnetic fields to analogous gravitational solutions and characterizing the topology of their lines of force. To extend the topologically non-trivial field configurations from electromagnetism to fields of spin-N we will apply complex contour integral methods using generating functions over twistor space. The spin-2 fields are then interpreted as solutions to the linearized Einstein equation representing gravitational radiation. The new solutions we will construct are the analogous gravitational fields corresponding to the null EM hopfions, the null EM torus knots, and the non-null EM hopfions. These field configurations and the analysis of their topological properties will be presented in Chapters 9, 10, and 11 respectively.

First, we give a review of some of the background material related to twistor theory. The heart of the twistor program is the relationship between $SL(2,\mathbb{C})$ spinors and light-like 4-vectors [82]. As preparation for understanding the twistor

integral methods used to construct solutions to the spin-N field equations, we will discuss $SL(2,\mathbb{C})$ spinors as representations of the universal cover of the Lorentz group and explore the underlying spin geometry of Minkowski space [39].

5.1 Introduction to $SL(2,\mathbb{C})$ Spinors

$SL(2,\mathbb{C})$ is the group of complex 2×2 matrices with unit determinant. Choosing the standard basis to be the extended Pauli matrices we define the following symbols, referred to as the *Infeld-van der Waerden symbols*[1]

$$\sigma_0^{AA'} \equiv \tfrac{1}{\sqrt{2}}\begin{pmatrix} 1 & 0 \\ 0 & 1 \end{pmatrix} \qquad \sigma_1^{AA'} \equiv \tfrac{1}{\sqrt{2}}\begin{pmatrix} 0 & 1 \\ 1 & 0 \end{pmatrix}$$
$$\sigma_2^{AA'} \equiv \tfrac{1}{\sqrt{2}}\begin{pmatrix} 0 & i \\ -i & 0 \end{pmatrix} \qquad \sigma_3^{AA'} \equiv \tfrac{1}{\sqrt{2}}\begin{pmatrix} 1 & 0 \\ 0 & -1 \end{pmatrix}.$$

and the inverse symbols $\sigma^a_{AA'}$ are defined by

$$\sigma_0^{AA'} = \sigma^0_{AA'} \quad \sigma_1^{AA'} = \sigma^1_{AA'} \quad \sigma_2^{AA'} = -\sigma^2_{AA'} \quad \sigma_3^{AA'} = \sigma^3_{AA'}.$$

[1] We reserve i and j for spatial indices, other lower case Latin letters for Lorentz indices, upper case Latin letters and their primed variants for spinor and conjugate spinor indices respectively, and lower case Greek letters for twistor indices.

We will now consider the null structure of $\mathbb{M}$ in terms of an $SL(2,\mathbb{C})$ spinorial structure. To each 4-vector $x^a \in \mathbb{M}$ there corresponds a Hermitian matrix $x^{AA'}$

$$\begin{aligned} x^{AA'} &= x^a \sigma_a^{AA'} \\ &= \frac{1}{\sqrt{2}} \begin{pmatrix} x^0 + x^3 & x^1 + ix^2 \\ x^1 - ix^2 & x^0 - x^3 \end{pmatrix}. \end{aligned}$$

It useful to note

$$\det x^{AA'} = \tfrac{1}{2}\left[(x^0)^2 - (x^1)^2 - (x^2)^2 - (x^3)^2\right] \tag{5.1}$$

$$= \tfrac{1}{2} x^a x_a. \tag{5.2}$$

Thus we have

$$\det x^{AA'} > 0 \text{ if } x^a \text{ is a timelike vector} \tag{5.3}$$

$$= 0 \text{ if } x^a \text{ is a null vector} \tag{5.4}$$

$$< 0 \text{ if } x^a \text{ is a spacelike vector.} \tag{5.5}$$

$$\tag{5.6}$$

Consider the transformation

$$\tilde{x}^{AA'} \to \Lambda^A{}_B x^{BB'} \Lambda^{A'}{}_{B'} \tag{5.7}$$

where $\Lambda^A{}_B \in SL(2,\mathbb{C})$ and $\Lambda^{A'}{}_{B'} = \overline{\Lambda^A{}_B}$ act on the unprimed and primed spin spaces, respectively. Note that elements of $SL(2,\mathbb{C})$ have unit determinant, so according to Eqn. (5.2), acting on any $x^{AA'}$ by an $SL(2,\mathbb{C})$ matrix preserves the

determinant, and thus the Minkowski pseudo-norm. So we have that the action of $SL(2,\mathbb{C})$ on $\mathbb{M}$ represents a set of linear transformations that preserve the metric, or the Lorentz transformations. However, from Eqn. (5.7) it is clear that Λ and $-\Lambda$ represent the same element of $SO(1,3)$ so the correspondence is two-to-one.

The transformation in Eqn. (5.7) also preserves the direction of the time axis, as shown by

$$\begin{aligned}
\tilde{x}^0 &= \sigma^0{}_{AA'}\Lambda^A{}_B\sigma_0{}^{BB'}\Lambda^{A'}{}_{B'} && (5.8)\\
&= \delta_{AA'}\Lambda^A{}_B\delta^{BB'}\Lambda^{A'}{}_{B'} && (5.9)\\
&= \left\|\Lambda^0{}_0\right\|^2+\left\|\Lambda^1{}_0\right\|^2+\left\|\Lambda^0{}_1\right\|^2+\left\|\Lambda^1{}_1\right\|^2 && (5.10)\\
&> 0. && (5.11)
\end{aligned}$$

So finally we can conclude that $SL\left(2,\mathbb{C}\right)$ is a 2-1 cover of the proper orthochronous Lorentz group

$$SO^+(1,3)\simeq SL(2,\mathbb{C})/\mathbb{Z}^2. \tag{5.12}$$

We can reparameterize the null structure of $\mathbb{M}$ in terms of an $SL\left(2,\mathbb{C}\right)$ spinorial structure since

1. each 4-vector $x^a\in\mathbb{M}$ corresponds to a Hermitian matrix $x^{AA'}$, and

2. if $x^a x_a=0$, then $\det x^{AA'}=0$.

It then follows that for null hermitian $x^{AA'}$ there exists an $SL(2,\mathbb{C})$ spinor $\pi^{A'}$ such that

$$x^{AA'} = \overline{\pi}^{A}\pi^{A'} = x^{a}\sigma_{a}^{AA'}. \tag{5.13}$$

The inner product on these spin spaces is determined by invariance under $SL(2,\mathbb{C})$ and is given by the Levi-Civita spinor

$$\epsilon_{AB} = \epsilon_{A'B'} = \epsilon^{AB} = \epsilon^{A'B'} \tag{5.14}$$

which is given in the canonical basis as

$$\epsilon_{AB} = \begin{pmatrix} 0 & 1 \\ -1 & 0 \end{pmatrix}. \tag{5.15}$$

The raising and lowering of indices in terms of the ϵ symbol is defined by

$$\begin{aligned} \psi^{A} &= \epsilon^{AB}\psi_{B} \\ \psi_{B} &= \psi^{A}\epsilon_{AB}, \end{aligned}$$

with similar relationships for the primed spin space.

The ϵ_{AB} symbol can be thought of as the spinor counterpart of the metric tensor. They are related by

$$g_{ab} = \epsilon_{AB}\epsilon_{A'B'}\sigma_{a}{}^{AA'}\sigma_{b}{}^{BB'}. \tag{5.16}$$

5.1.1 Spinor Decomposition of a Bivector

The field strength tensor and curvature tensor can be written in terms of their spinor decompositions [83]. Consider a bivector $W_{ab} = -W_{ba}$ that corresponds to the spinor $W_{ab} \to W_{AA'BB'}$. The relative order of the primed and unprimed indices is irrelevant, so we can rearrange them

$$W_{AA'BB'} = W_{ABA'B'}. \tag{5.17}$$

The anti-symmetry in the Lorentz indices allows us to write

$$\begin{aligned} W_{ABA'B'} = &\quad W_{AB[A'B']} + W_{[AB]A'B'} \\ = &\quad \overline{\mu}_{AB}\epsilon_{A'B'} + \epsilon_{AB}\mu_{A'B'} \end{aligned} \tag{5.18}$$

with the symmetric spinor

$$\mu_{AB} = \frac{1}{2} W_{(AB)C'}{}^{C'}. \tag{5.19}$$

The dual of W is

$$*W_{ab} = \frac{1}{2}\epsilon_{abcd}W^{cd} \tag{5.20}$$

and the spinor equivalent of ϵ_{abcd} is given by

$$\epsilon_{AA'BB'CC'DD'} = i(\epsilon_{AC}\epsilon_{BD}\epsilon_{A'D'}\epsilon_{B'C'} - \epsilon_{AD}\epsilon_{BC}\epsilon_{A'C'}\epsilon_{B'D'}). \tag{5.21}$$

Using the above and with some algebra we can decompose W into the anti-self-dual (ASD) and self-dual parts (SD) of W

$$\begin{aligned}(W_+)_{ab} &= \frac{1}{2}\left(W_{ab} + i * W_{ab}\right) \\ (W_-)_{ab} &= \frac{1}{2}\left(W_{ab} - i * W_{ab}\right)\end{aligned}$$

and we find W_+ and W_- are

$$\begin{aligned}(W_+)_{ABA'B'} &= \epsilon_{AB}\mu_{A'B'} \\ (W_-)_{ABA'B'} &= \overline{\mu}_{AB}\epsilon_{A'B'}.\end{aligned}$$

If W is the electromagnetic field strength tensor F_{ab}, then the spinor fields $\bar{\mu}_{AB}$ and $\mu_{A'B'}$ satisfy the source-free field equations.

We can follow a similar procedure for the curvature spinor

$$R_{abcd} = R_{AA'BB'CC'DD'}. \tag{5.22}$$

Since R_{abcd} is anti-symmetric in ab we can use the decomposition in Eqn. (5.18) to write

$$R_{abcd} = \tfrac{1}{2}R_{AX'B}{}^{X'}{}_{cd}\epsilon_{A'B'} + \tfrac{1}{2}R_{XA'}{}^{X}{}_{Bcd}\epsilon_{AB}. \tag{5.23}$$

Using the anti-symmetry in cd, we can apply the bivector decomposition again to obtain

$$R_{abcd} = \quad \bar{X}_{ABCD}\epsilon_{A'B'}\epsilon_{C'D'} + \bar{\Phi}_{ABC'D'}\epsilon_{A'B'}\epsilon_{CD} \tag{5.24}$$

$$+\Phi_{A'B'CD}\epsilon_{AB}\epsilon_{C'D'} + X_{A'B'C'D'}\epsilon_{AB}\epsilon_{CD}, \tag{5.25}$$

where

$$X_{ABCD} = \frac{1}{4} R_{AX'B}{}^{X'}{}_{CY'D}{}^{Y'} \tag{5.26}$$

$$\Phi_{ABC'D'} = \frac{1}{4} R_{AX'B}{}^{X'}{}_{YC'}{}^{Y}{}_{D'}. \tag{5.27}$$

In vacuum, $\Phi = \bar{\Phi} = 0$ yielding the Weyl tensor

$$C_{abcd} = \bar{X}_{ABCD}\epsilon_{A'B'}\epsilon_{C'D'} + X_{A'B'C'D'}\epsilon_{AB}\epsilon_{CD}. \tag{5.28}$$

5.2 $SL(2,\mathbb{C})$ Spinor Geometry

The geometry underlying the $SL(2,\mathbb{C})$ spinor structure is closely related to the Celestial sphere of an observer in $\mathbb{M}$ [84]. The Celestial sphere is the Riemann sphere corresponding to the null histories coincident with the origin. Figure 5.1a illustrates this relationship. The null cone of the origin intersects the $x^0 = \tau$ hyperplane, with each null ray meeting this hyperplane exactly once. This intersection is described by the equation

$$(x^1)^2 + (x^2)^2 + (x^3) = \tau^2. \tag{5.29}$$

This mathematically represents a 2-sphere which can be physically interpreted as the set of light rays that are moving inward toward the observer for $\tau < 0$, until it collapses upon the origin at $\tau = 0$, and then moves outward away from the origin for $\tau > 0$.

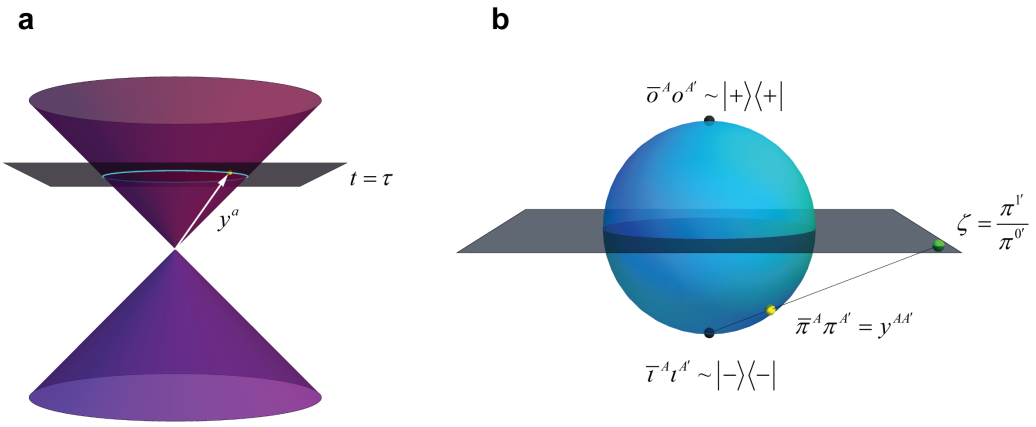

Figure 5.1: The flagpole relation is the central relation in the spin geometry of $\mathbb{M}$. Here we see that to every 2-spinor $\pi^{A'}$ there corresponds a light-like 4-vector y^a called its flagpole. **a** When the lightcone of the origin (violet) is intersected with the space-like hyperplane $t = \tau$ (dark grey), we obtain the Minkowski space representation of an expanding sphere of light emitted at the origin, called the Celestial sphere (blue). Any light-like 4-vector y^a (white) may be represented by the unique point where it meets this sphere (yellow). **b** Analogous to the pure state representation of the Bloch sphere, the Celestial sphere may be put in 1-1 correspondence with the set of 2×2 Hermitian matrices with trace equal to $\sqrt{2}\tau$. The 2-spinor $\pi^{A'}$ is taken as a homogeneous coordinate on the complex plane (light grey) of the sphere $\zeta = \pi^{1'}/\pi^{0'}$ (green). The flagpole of $\pi^{A'}$ is then identified with the 4-vector $y^{AA'}$ written in flagpole form as a 2×2 Hermitian matrix.

To relate the Celestial sphere to the spinor structure of $SL(2, \mathbb{C})$, we associate to it the Riemann sphere parameterized by the complex coordinate

$$\zeta = \frac{x^1 + \imath x^2}{\tau - x^3} \tag{5.30}$$

as in Figure 5.1b. The Möbius group is the isometry group of the Riemann sphere, and thus through stereographic projection is also the isometry group of null rays passing through the origin of $\mathbb{M}$. This means that the action of the

proper orthochronous Lorentz transformations on the Celestial sphere are Möbius transformations on its Riemann sphere. $SL(2,\mathbb{C})/\mathbb{Z}_2$ is related to the Möbius group through the homomorphism with $SO^+(1,3)$.

A general Möbius transformation has the form

$$\widetilde{\zeta} = \frac{a\zeta + b}{c\zeta + d} \tag{5.31}$$

with $a, b, c, d \in \mathbb{C}$ and $ad - bc = 1$. We can treat ζ as a homogeneous coordinate using the 2-spinor $\pi^{A'}$ so that

$$\zeta = \frac{\pi^{1'}}{\pi^{0'}}. \tag{5.32}$$

This homogeneous coordinate allows us to represent Eqn. (5.31) as a fractional linear transformation on an $SL(2,\mathbb{C})$ spinor $\pi^{A'}$.

$$\frac{\widetilde{\pi}^{1'}}{\widetilde{\pi}^{0'}} = \frac{a\pi^{0'} + b\pi^{1'}}{c\pi^{0'} + d\pi^{1'}} \tag{5.33}$$

where $\pi^{A'}$ goes to $\widetilde{\pi}^{A'}$ via the $SL(2,\mathbb{C})$ transformation given by the matrix

$$\begin{pmatrix} a & b \\ c & d \end{pmatrix}. \tag{5.34}$$

To obtain the coordinates for x^a we invert the stereographic projection given by Eqn. (5.30) using the homogeneous coordinate in Eqn. (5.32), where we choose

$\tau = (\overline{\pi}^0\pi^{0'} + \overline{\pi}^1\pi^{1'})/\sqrt{2}$ as the radius of the Celestial sphere. The result is

$$\begin{aligned} x^0 &= \frac{1}{\sqrt{2}}(\overline{\pi}^0\pi^{0'} + \overline{\pi}^1\pi^{1'}) \\ x^1 &= \frac{1}{\sqrt{2}}(\overline{\pi}^0\pi^{1'} + \overline{\pi}^1\pi^{0'}) \\ x^2 &= \frac{i}{\sqrt{2}}(\overline{\pi}^0\pi^{1'} - \overline{\pi}^1\pi^{0'}) \\ x^3 &= \frac{1}{\sqrt{2}}(\overline{\pi}^0\pi^{0'} - \overline{\pi}^1\pi^{1'}). \end{aligned} \tag{5.35}$$

5.3 Spin-N Field Equations

We will now discuss the massless spin-N equations and their solutions in their standard form (on $\mathbb{M}$).

A massless particle with spin-0 satisfies the wave equation given by

$$\Box\phi = 0 \tag{5.36}$$

where the standard wave operator is

$$\Box = \nabla^{AA'}\nabla_{AA'} \tag{5.37}$$

with the 2-spinor derivative related to the gradient operator in $\mathbb{M}$ (or $\mathbb{CM}$) by

$$\nabla^{AA'} = \sigma_a^{AA'}\partial^a. \tag{5.38}$$

The spin-1 equation describes a physical electromagnetic field, so its solution must be a real bivector. As we showed before in Eqn. (5.18), an arbitrary real bivector

has the spinor form

$$F_{AA'BB'} = \overline{\varphi}_{AB}\epsilon_{A'B'} + \epsilon_{AB}\varphi_{A'B'} \tag{5.39}$$

where the only real degree of freedom is a SD bivector generated by the symmetric spinor

$$\varphi_{A'B'} = \varphi_{(A'B')}. \tag{5.40}$$

Now consider the source-free Maxwell equation for a SD field

$$\partial^a F^+_{ab} = 0. \tag{5.41}$$

The spinor form of this equation is

$$\partial^a F^+_{ab} \to \nabla^{AA'} F^+_{AA'BB'} \tag{5.42}$$

and can be written as

$$\nabla^{AA'} F^+_{AA'BB'} = \nabla^{AA'}\epsilon_{AB}\varphi_{A'B'}. \tag{5.43}$$

The spin-1 equation is then obtained from the vanishing of Eqn. (5.43)

$$\nabla^{AA'}\varphi_{A'B'} = 0. \tag{5.44}$$

This generalizes to the source-free massless spin-N spinor field equation given by

$$\nabla^{AA'_1}\varphi_{A'_1\cdots A'_{2h}}(x) = 0. \tag{5.45}$$

In the case of spin-1 and spin-2 the classical field strength tensors are given by

$$\begin{aligned} F_{A'_1A'_2\ A_1A_2} &= \varphi_{A'_1A'_2}\epsilon_{A_1A_2} + \overline{\varphi}_{A_1A_2}\epsilon_{A'_1A'_2} \\ C_{A'_1\cdots A'_4\ A_1\cdots A_4} &= \varphi_{A'_1\cdots A'_4}\ \epsilon_{A_1A_2}\ \epsilon_{A_3A_4} + \overline{\varphi}_{A_1\cdots A_4}\ \epsilon_{A'_1A'_2}\ \epsilon_{A'_3A'_4}. \end{aligned} \tag{5.46}$$

The solutions for the half-integer spin cases have no world-tensor description, but typically are associated with a physical current given by the flagpole of the spinor. For example, the spin-$\frac{1}{2}$ current is

$$j_a = \sigma_a^{AA'} \overline{\varphi}_A \varphi_{A'}. \tag{5.47}$$

The spin-N field equations and their physical interpretations are summarized in Table 5.1.

Spin	Field Eqn.	Spinor Eqn.	Physical Interpretation
0	$\Box\varphi = 0$	$\Box\varphi = 0$	Scalar Wave
$-\frac{1}{2}$		$\nabla^{AA'}\overline{\varphi}_A = 0$	Neutrino (massless)
$+\frac{1}{2}$		$\nabla^{AA'}\varphi_{A'} = 0$	Anti-neutrino
-1	$dF = 0$	$\nabla^{AA'}\overline{\varphi}_{AB} = 0$	Electromagnetism (LH,ASD)
$+1$	$d * F = *J$	$\nabla^{AA'}\varphi_{A'B'} = 0$	Electromagnetism (RH,SD)
$-\frac{3}{2}$		$\nabla^{AA'}\overline{\varphi}_{ABC} = 0$	Anti-gravitino
$+\frac{3}{2}$		$\nabla^{AA'}\varphi_{A'B'C'} = 0$	Gravitino
-2	$g^{bd}C_{abcd} = 0$	$\nabla^{AA'}\overline{\varphi}_{ABCD} = 0$	Gravity (LH,ASD)
$+2$		$\nabla^{AA'}\varphi_{A'B'C'D'} = 0$	Gravity (RH,SD)

Table 5.1: The massless linear relativistic spin-N field equations and their physical interpretation.

5.4 Spinor Classification of Tensors

One of the most useful applications of $SL(2,\mathbb{C})$ spinors in physics is the classification of solutions to the spin-N field equations. These solutions are totally symmetric spinors, and can therefore be written as a symmetrized product of $2N$ one-index spinors [21]. This is referred to as the canonical decomposition. For

example, the spin-2 solutions can be written in general as

$$\overline{\phi}_{(A'B'C'D')} = \alpha_{(A}\beta_B\gamma_C\delta_{D)} \tag{5.48}$$

where α_A, β_B, γ_C, and δ_D are all assumed to be non-vanishing and non-proportional. The flagpole of each one-index spinor represents a *principle null direction (PND)* of the symmetric spinor. The PNDs determine the spinor uniquely, upto an overall complex scalar.

In special cases, the PNDs coincide with each other and this degeneracy provides a classification scheme. This is most often used with real spin-1 and spin-2 fields which are associated to a field strength tensor according to Eqn. (5.46). For the Weyl curvature spinor (and its corresponding world-tensor) this scheme is referred to as the Petrov classification, but it can be generalized to any solutions described by a symmetric spinor. The spinor classification of a solution is related to its physical properties. We will be particularly interested in the relativistic scalar invariants of the fields. These invariants contain physical information about the field configuration [85].

In elecromagnetism, there is one complex relativistic invariant - the square of the RS vector $\vec{F}_{RS} = \vec{E} + \imath\vec{B}$,

$$\begin{aligned} K &= \vec{F}_{RS}^2 \\ &= \vec{E}^2 - \vec{B}^2 + 2i\vec{E}\cdot\vec{B}, \end{aligned} \tag{5.49}$$

whose real and imaginary parts are the two invariants

$$P = \vec{E}^2 - \vec{B}^2 = -\frac{1}{2}\boldsymbol{F}\cdot\boldsymbol{F} \equiv -\frac{1}{2}F^{ab}F_{ab}, \tag{5.50}$$

$$Q = 2\vec{E}\cdot\vec{B} = -\frac{1}{2}\boldsymbol{F}\cdot *\boldsymbol{F} \equiv -\frac{1}{2}F^{ab}\epsilon_{abcd}F^{cd}. \tag{5.51}$$

For spin-1 fields, there are two PNDs and thus two possible configurations. A field with two degenerate PNDs is called null. A field with two distinct PNDs is non-null. Null EM fields are characterized by both invariants P and Q vanishing, implying that the electric and magnetic fields are orthogonal and of the same magnitude (in natural units). Physically null fields are purely radiative, for example an EM plane wave. Non-null EM fields are characterized by $K = P + \imath Q \neq 0$. If $Q = 0$, and $P < 0$ (or > 0), then there must exist a frame in which the field is purely magnetic, $\vec{E} = 0$ (or purely electric, $\vec{B} = 0$). Finally, if $Q \neq 0$ then there is no frame in which the field is purely electric or purely magnetic, but it is possible to find a frame in which $\vec{E}$ and $\vec{B}$ are proportional. The spinor classifications of EM solutions are summarized in Table 5.2.

Spinor Classification	PND degeneracy	ϕ_{AB}	Scalar Invariants
null	$\{2\}$	$\alpha_A\alpha_B$	0 scalars $K = 0$
non-null	$\{11\}$	$\alpha_{(A}\beta_{B)}$	2 scalars $K \neq 0$
O	$\{-\}$	0	0 scalars $K = 0$

Table 5.2: The spinor classifications of the EM field strength tensor and their properties.

Following the analogy with EM, we can use the relationship $\{\boldsymbol{F}\cdot\boldsymbol{F}, \boldsymbol{F}\cdot*\boldsymbol{F}\} \rightarrow \{\boldsymbol{R}\cdot\boldsymbol{R}, \boldsymbol{R}\cdot*\boldsymbol{R}\}$ between the EM and gravitational "curvature" invariants to gain physical insight into the gravitational solutions of various Petrov type.[2]

In the case of the gravitational curvature, the two quadratic invariants are given by

$$E^{ij}E_{ij} - B^{ij}B_{ij} = \frac{1}{8}\boldsymbol{R}\cdot\boldsymbol{R}, \qquad E^{ij}B_{ij} = \frac{1}{16}\boldsymbol{R}\cdot*\boldsymbol{R}. \tag{5.52}$$

These are often combined into a single complex quantity $I \equiv \frac{1}{8}(\boldsymbol{R}\cdot\boldsymbol{R} + i\boldsymbol{R}\cdot*\boldsymbol{R})$. The Riemann tensor differs from the EM tensor in that, in addition to its quadratic invariants, it has two cubic invariants

$$A \equiv \frac{1}{16}R^{ab}{}_{cd}R^{cd}{}_{ef}R^{ef}{}_{ab}, \qquad B \equiv \frac{1}{16}R^{ab}{}_{cd}R^{cd}{}_{ef} * R^{ef}{}_{ab}, \tag{5.53}$$

which are similarly combined into the complex quantity $J \equiv A - iB$.

Just as the EM tensor invariants contain physical information about the EM field configuration, these gravitational invariants contain analogous information about the gravitational field configuration. If $\boldsymbol{R}\cdot\boldsymbol{R} = \boldsymbol{R}\cdot*\boldsymbol{R} = 0$ then the field is purely radiative. If on the other hand $\boldsymbol{R}\cdot*\boldsymbol{R} = 0$, $\boldsymbol{R}\cdot\boldsymbol{R} < 0$ (or > 0), and additionally $M \equiv I^3/J^2 - 6 \geq 0$ (this quantity being real under the other conditions), then there must exist a frame in which the field is purely magnetic, $E_{ij} = 0$ (or purely electric, $B_{ij} = 0$). Finally if $\boldsymbol{R}\cdot*\boldsymbol{R} \neq 0$ then there exists no

[2]Note that in vacuum solutions the Weyl tensor C_{abcd} is equal to the Riemann tensor R_{abcd}.

frame in which the field is purely electric or purely magnetic, which we again call intrinsic curvature.

Petrov class	PND degeneracy	ϕ_{ABCD}	Scalar Invariants
N (null)	$\{4\}$	$\alpha_A\alpha_B\alpha_C\alpha_D$	0 scalars $I = J = 0$
D (double)	$\{22\}$	$\alpha_{(A}\alpha_B\beta_C\beta_{D)}$	2 scalars $I^3 = 6J^2$
III	$\{31\}$	$\alpha_{(A}\alpha_B\alpha_C\beta_{D)}$	0 scalars $I = J = 0$
II	$\{211\}$	$\alpha_{(A}\alpha_B\beta_C\gamma_{D)}$	2 scalars $I^3 = 6J^2$
I	$\{1111\}$	$\alpha_{(A}\beta_B\gamma_C\delta_{D)}$	4 scalars $I^3 \neq 6J^2$
O	$\{-\}$	0	0 scalars $I = J = 0$

Table 5.3: The Petrov classifications of the Weyl curvature tensor and their properties.

Gravitational fields are spin-2 and therefore have four PNDs. There are five non-trivial Petrov classifications. Solutions with three or more PNDs coinciding have all four scalars vanishing. This includes Type N fields, which have four PNDs aligned and are the analog of null EM fields, as well as Type III, which have three PNDs aligned. Solutions with two or more PNDs coinciding have $I^3 = 6J^2$, resulting in only two independent scalars. These fields are the Type D, which have two pairs of aligned PNDs and are the analog of non-null EM fields, and Type II, which has two aligned and two other unique PNDs. Finally there is the most general case, Type I, which has four unique PNDs and four non-trivial

scalar invariants. The spinor classifications of the Weyl curvature are summarized in Table 5.3. These classifications will be important later in our characterization of knotted EM and gravitational solutions.

Chapter 6

Twistor Theory

Twistor theory was developed by Roger Penrose in the late 1960's as an extension of the $sl(2,\mathbb{C})$ spinor algebra [86–88]. One can think of twistor space $\mathbb{T}$ as the total momentum space for massless particles in which the linear and angular momentum are combined into a single object called a twistor [21]. Using the $SL(2,\mathbb{C})$ representation of light-like 4-vectors in $\mathbb{M}$, we can associate each (projective) twistor to a spinor field, with null twistors corresponding to light-like geodesics and non-null twistors corresponding to a collection of twisting shear-free null geodesics called a Robinson congruence [89]. The projection of a Robinson congruence onto a constant time hyperplane forms a vector field tangent to a Hopf fibration, suggesting that the twistor formalism will provide a convenient method for studying the hopfion fields discussed in later chapters. We will now review the fundamentals of twistor theory highlighting its connection to the Robinson congruence.

6.1 Twistors and Total Momentum

Twistor theory uses the underlying geometry of light-like histories in $\mathbb{M}$ to reparameterize the momentum of massless particles by an $SL(2,\mathbb{C})$ spinor structure. When linear and angular momentum are combined, this total momentum possesses two spinorial degrees of freedom denoted by ω^A and $\pi_{A'}$. The dependence of the momentum structure (M^{ab}, p^c) on the origin induces a position dependence in $(\omega^A, \pi_{A'})$, making them spinor fields on space-time.

The linear 4-momentum is given by a null 4-vector p^a which we take to be the flagpole of a spinor $\pi^{A'}$ so that

$$p^a = \overline{\pi}^A \pi^{A'} \sigma^a_{AA'}. \tag{6.1}$$

The angular momentum is a bivector and by Eqn. (5.18) is given by

$$M_{ab} = \left(\mu_{AB}\epsilon_{A'B'} + \epsilon_{AB}\overline{\mu}_{A'B'}\right) \sigma_a^{AA'} \sigma_b^{BB'} \tag{6.2}$$

with μ_{AB} symmetric. The Pauli-Lubanski spin vector, S_a, is defined by

$$\begin{aligned} S_a &= *M_{ab}p^b \\ &= \frac{1}{2}\epsilon_{abcd}M^{cd}p^b, \end{aligned}$$

and from Eqn. (6.1) and (6.2) we find

$$S_{AA'} = \frac{1}{2}\left(\imath\mu_{AB}\epsilon_{A'B'}\overline{\pi}^B\pi^{B'} - \imath\epsilon_{AB}\overline{\mu}_{A'B'}\overline{\pi}^B\pi^{B'}\right).$$

Since massless particles must have spin parallel to p^a we have that

$$\imath\epsilon_{AB}\overline{\mu}_{A'B'}\overline{\pi}^B\pi^{B'} = 0.$$

Thus, $\overline{\mu}_{A'B'}$ must take the form

$$\overline{\mu}_{A'B'} = \alpha_{(A'}\beta_{B')}$$

where either $\alpha_{A'}$ or $\beta_{A'}$ must be proportional to $\pi_{A'}$, so that

$$\overline{\mu}_{A'B'} = i\overline{\omega}_{(A'}\pi_{B')}$$

for some spinor we will call ω_A. Thus we may regard (p, M) and (ω, π) as providing equivalent parameterizations of the dynamical content of a massless free particle. We can summarize this equivalence by

$$p^a \quad \longleftrightarrow \quad \overline{\pi}^A\pi^{A'} \tag{6.3}$$

$$M^{ab} \quad \longleftrightarrow \quad i\omega^{(A}\overline{\pi}^{B)}\epsilon^{A'B'} - i\epsilon^{AB}\overline{\omega}^{(A'}\pi^{B')}. \tag{6.4}$$

To see how the position dependence of (p, M) induces a position dependence on (ω, π), consider a translation of the origin of $\mathbb{M}$. Under a translation by x^a we have that the translated pair $\left(\widetilde{p}, \widetilde{M}\right)$ is given by

$$\begin{aligned} \widetilde{p}^a &= p^a \\ \widetilde{M}^{ab} &= M^{ab} + 2x^{[a}p^{b]}. \end{aligned}$$

The dependence of the momentum structure (M^{ab}, p^c) on the origin induces a position dependence in $(\widetilde{\omega}, \widetilde{\pi})$, so they becomes spinor fields on space-time given

by

$$\widetilde{\pi}^{A'}(x) = \pi^{A'} \tag{6.5}$$

$$\widetilde{\omega}^{A}(x) = \omega^{A} - ix^{AA'}\pi_{A'}. \tag{6.6}$$

A twistor Z, in twistor space $\mathbb{T}$, is composed of this pair of kinematically related $SL(2,\mathbb{C})$ spinors $(\omega^A, \pi_{A'})$ such that:

1. The flagpole of π represents a 4-momentum.

2. The symmetrized products of $i\omega\overline{\pi}$ and its conjugate represent respectively the SD and ASD components of an angular momentum tensor.

Thus, a twistor is a 4D complex object with components

$$Z^{\alpha} = \left(\omega^{A}, \pi_{A'}\right), \tag{6.7}$$

or more explicitly

$$\begin{aligned} \left(Z^0, Z^1\right) &= \left(\omega^0, \omega^1\right) \\ \left(Z^2, Z^3\right) &= \left(\pi_{0'}, \pi_{1'}\right). \end{aligned}$$

The index structure allows one to construct a useful relationship between the twistor psedo-norm and helicity. The twistorial dual is found by permuting the component spinors and taking an overall complex conjugate. This is denoted by

$$\overline{Z}_{\alpha} \equiv \left(\overline{\pi}_{A}, \overline{\omega}^{A'}\right). \tag{6.8}$$

The twistor pseudo-norm

$$Z^{\alpha}\overline{Z}_{\alpha} = \omega^{A}\overline{\pi}_{A} + \pi_{A'}\overline{\omega}^{A'}. \tag{6.9}$$

can then be related to helicity. Recall that for a massless particle we define its helicity, $\mathfrak{h}$, as the constant of proportionality between S_a and p_a. Thus we find that

$$S_{AA'} = \mathfrak{h} p_{AA'}$$

implies

$$\mathfrak{h} = \frac{1}{2} Z^{\alpha} Z_{\alpha}. \tag{6.10}$$

Helicity provides for a natural geometric partition of $\mathbb{T}$ into three sets, $\mathbb{T}^{+}$, $\mathbb{T}^{-}$, and $\mathbb{N}$, according to whether the helicity is positive, negative, or zero.

$$\begin{aligned} \mathbb{T}^{+} &\equiv \left\{ Z^{\alpha} \in \mathbb{T} | \mathfrak{h} > 0 \right\} \\ \mathbb{N} &\equiv \left\{ Z^{\alpha} \in \mathbb{T} | \mathfrak{h} = 0 \right\} \\ \mathbb{T}^{-} &\equiv \left\{ Z^{\alpha} \in \mathbb{T} | \mathfrak{h} < 0 \right\}. \end{aligned}$$

Twistors from $\mathbb{N}$ are called null and elsewise are called non-null. Only null twistors have a direct geometric correspondence with $\mathbb{M}$. As we shall see later, helicity also provides a mechanism for twistor quantization.

6.2 Twistor Geometry

We begin by returning to the spinor fields given in Eqns. (6.5) and (6.6)

$$\begin{aligned} \widetilde{\pi}^{A'}(x) &= \pi^{A'} \\ \widetilde{\omega}^{A}(x) &= \omega^{A} - ix^{AA'}\pi_{A'}. \end{aligned}$$

The spinors $\left(\omega^A, \pi_{A'}\right)$ are constant spinor fields on $\mathbb{M}$ that are equivalent to $\left(\widetilde{\omega}^A, \widetilde{\pi}^{A'}\right)$ at the origin. They define the general solution of

$$\nabla^{(A}_{A'}\widetilde{\omega}^{B)} = 0$$

which is referred to as the twistor equation. Consider the result obtained by taking $\widetilde{\omega} = 0$

$$\omega^A = ix^{AA'}\pi_{A'}. \tag{6.11}$$

Eqn. (6.11) is called the incidence relation and it defines the explicit relationship between $\mathbb{T}$ and $\mathbb{M}$. Since the definition of angular momentum involves both position and momentum there is a direct relation between twistors and positions in Minkowski space. To understand this relationship, fix $\left(\omega^A, \pi_{A'}\right) \in \mathbb{T}$ and solve Eqn. (6.11) for $x^{AA'}$. Suppose $x_0^{AA'}$ satisfies the incidence relation, then

$$x^{AA'} = x_0^{AA'} + \zeta^A\pi^{A'} \tag{6.12}$$

also satisfies it for all $\zeta^A \in \mathbb{CP}^1$, where all tangent vectors v^a are of the form

$$v^a = \sigma^a_{AA'}\zeta^A\pi^{A'}.$$

For a fixed $\pi^{A'}$, varying ζ^A in Eqn. (6.12) gives a complex 2D subspace of complexified Minkowski space $\mathbb{CM}$, where each element is null and any two are orthogonal. Planes with these properties are called α-planes. (There are actually two families of planes on $\mathbb{CM}$ with these properties. The first are the α-planes. The second kind, called β-planes, is found by fixing ζ^A and varying $\pi^{A'}$ and corresponds to dual twistors.)

The intersection of any two α-planes represents a point $y^a \in \mathbb{CM}$. For two twistors $Z^\alpha = \left(\omega^A, \pi_{A'}\right)$ and $W^\alpha = \left(\theta^A, \phi_{A'}\right)$, we can apply the incidence relation to each twistor and solve the set of equations

$$\begin{aligned} \omega^A &= iy^{AA'}\pi_{A'} \\ \theta^A &= iy^{AA'}\phi_{A'}, \end{aligned}$$

and we obtain an explicit formula for the point corresponding to their intersection

$$y^{AA'} = \frac{\omega^A \phi^{A'} - \theta^A \pi^{A'}}{i\left(\phi^{B'}\pi_{B'}\right)}.$$

In general a point $y^a \in \mathbb{CM}$ is represented by a complex 2D subspace in $\mathbb{T}$, given by the set of all twistors Y^α whose associated α-planes intersect at y^a. We say Y^α is the family of α-planes corresponding to y^a and it can be written as a linear combination of Z^α and W^α

$$Y^\alpha = c_1 Z^\alpha + c_2 W^\alpha \tag{6.13}$$

with $c_1, c_2 \in \mathbb{C}$.

Most α-planes contain no real points. However, substituting the incidence relation from Eqn. (6.11) into the helicity from Eqn. (6.10) and evaluating at $x_0^{AA'}$ we find that

$$\mathfrak{h} = \frac{i}{2}\left(x_0^{AA'} - \overline{x_0^{AA'}}\right)\overline{\pi}_A \pi_{A'}. \tag{6.14}$$

If $\mathfrak{h} = 0$ this implies that $x_0^{AA'}$ is real. If the plane contains one real point, then it must contain a line of them. So the remaining solutions have the form

$$x^{AA'} = x_0^{AA'} + r\overline{\pi}^A \pi^{A'} \tag{6.15}$$

for $r \in \mathbb{R}$. This describes a null straight line in the direction of the flagpole of $\bar{\pi}^A$.

Using the hermicity of $x_0^{AA'}$ and the incidence relation we find a particular solution

$$x_0^{AA'} = \frac{\omega^A \overline{\omega}^{A'}}{i(\overline{\omega}^{B'} \pi_{B'})}. \tag{6.16}$$

Combining Eqn. (6.15) with Eqn. (6.16) we arrive at the geometric representation of a null twistor in $\mathbb{M}$. If we fix the origin O of $\mathbb{M}$, then the null twistor Z^α represents a light-like worldline in $\mathbb{M}$ parallel to the flagpole of $\pi_{A'}$, which meets the lightcone of the origin along the flagpole of ω^A at the point x_0^a given by

$$x_0^a = \frac{\omega^A \overline{\omega}^{A'}}{i(\overline{\omega}^{B'} \pi_{B'})} \sigma^a_{AA'}.$$

Figure 6.1a illustrates the correspondence described above.

For non-null twistors, Eqn. (6.11) possesses no Hermitian solutions, and thus its direct geometric interpretation is in terms of complexified Minkowski space.

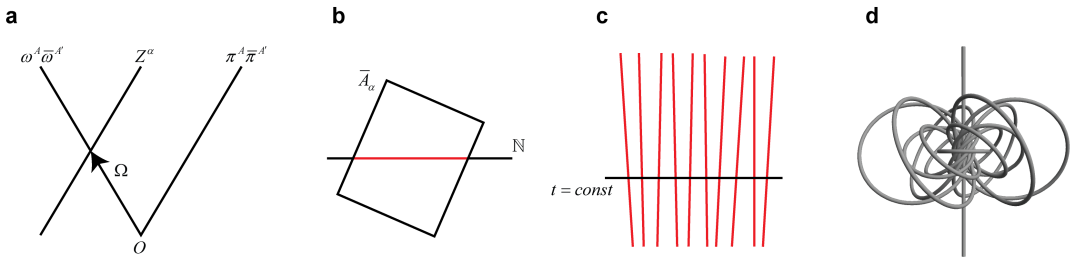

Figure 6.1: A null twistor Z^α corresponds to a light-like world-line in $\mathbb{M}$. A non-null twistor A^α possesses only an indirect correspondence in $\mathbb{M}$ constructed via the direct correspondence for null twistors. **a** If $Z^\alpha = (\omega^A, \pi_{A'})$ is a null twistor, then it corresponds to a light-like world-line (null geodesic) in $\mathbb{M}$, parallel to the flagpole of $\pi_{A'}$, which meets the lightcone of the origin along the light-like ray parallel to the flagpole of ω^A. Here $\Omega = x_0^{AA'}$. **b** The dual of a non-null twistor $\overline{A}_\alpha$ is a plane in $\mathbb{T}$ which is uniquely defined by its intersection with $\mathbb{N}$ (red). **c** The Minkowski space representation of the non-null twistor $\overline{A}_\alpha$ wherein each of the null twistors in the intersection with $\mathbb{N}$ appear as the null geodesics in $\mathbb{M}$ which comprise the Robinson congruence. **d** Viewed on a hyperplane of constant time, the Robinson congruence defines a vector field whose integral curves are the fibers of a Hopf map projected down stereographically onto the hyperplane.

However, as shown in Figure 6.1b-c, we can obtain an indirect geometric correspondence by exploiting the direct relation for null twistors. If A^α is non-null then its dual $\overline{A}_\alpha$ is a plane in $\mathbb{T}$. This plane is uniquely defined by its intersection with $\mathbb{N}$ and hence by the solution of the system

$$\overline{A}_\alpha Z^\alpha = 0, \tag{6.17}$$

$$\overline{Z}_\alpha Z^\alpha = 0. \tag{6.18}$$

Each point in this intersection represents a null geodesic. The set of all null twistors in the intersection corresponds to a space-filling set of null geodesics in $\mathbb{M}$ called the Robinson congruence. If we project the tangent vector field of one of

these congruences onto a hyperplane of constant time then we find that it forms the tangent vector field of a Hopf fibration. The integral curves of the vector field are a special family of circles which lie on a set of space-filling nested tori. Each circle, called a Villarceau circle, is linked with every other one exactly once. In fact, it was the Hopf structure of the Robinson congruence which inspired Penrose to use the name "twistor."

The geometric correspondence defined by the incidence relation in Eqn. (6.11) is projective. That is, a twistor Z^α multiplied by any non-zero complex number corresponds to the same object in $\mathbb{M}$ as Z^α itself. This leads us to consider as most fundamental the projective twistor space $\mathbb{PT}$ defined as $\mathbb{T}$ under the equivalence relation $Z^\alpha \sim \lambda Z^\alpha$ for $\lambda \neq 0$. The partitions of $\mathbb{T}$ naturally extend to partitions of $\mathbb{PT}$, denoted by $\mathbb{PT}^+$, $\mathbb{PT}^-$, and $\mathbb{PN}$. The geometric correspondences are most succinctly characterized in terms of the partitions of $\mathbb{PT}$, as shown in Figure 6.2.

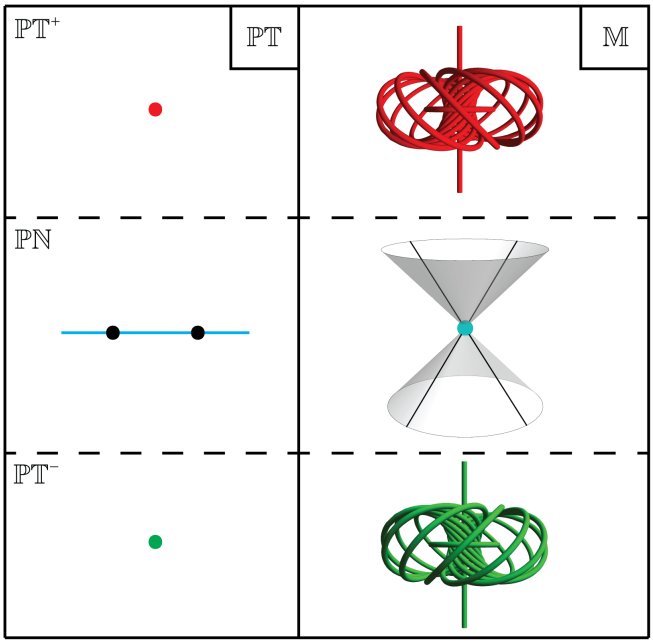

Figure 6.2: A summary of the geometric correspondences in terms of $\mathbb{PT}$ and $\mathbb{M}$. A point in either $\mathbb{PT}^+$ (red) or $\mathbb{PT}^-$ (green) corresponds to a Robinson congruence in $\mathbb{M}$. An entire $\mathbb{CP}^1$ (Celestial sphere) in $\mathbb{PN}$ (blue) corresponds to a point in $\mathbb{M}$. Any two points which lie on a $\mathbb{CP}^1$ in $\mathbb{PN}$ correspond to light-like world-lines which lie on the light cone of the point corresponding to that $\mathbb{CP}^1$.

Chapter 7

The Penrose Transform

As early as 1903 the importance of a complex analytic structure to the solutions of real PDE's began to emerge with the work of Whittaker, who found a contour integral expression for the general solution to Laplace's equation [90]. In 1915 Bateman, building on the results of Whittaker, extended this analytic structure to obtain the general solution to the vacuum Maxwell equations [91]. As we saw in the previous chapters, the twistor program of Penrose interprets the complex analytic structure as encoding the geometry of spinor fields on space-time [92,93]. In this language the various massless linear relativistic fields are represented as symmetric spinor fields (spin-N fields).

In 1969, Roger Penrose first gave the solution to the spin-N field equations for massless fields of helicity h by contour integration over homogeneous twistor wavefunctions [94]. He found that the twistor parameterization of helicity allows for a unique perspective on the standard relativistic field theories whereby the massless spin-h field equations are replaced by the twistor helicity equation [22].

However, the helicity equation simply specifies the helicity associated to the momentum structure encoded in Z^α. In order to treat the helicity as an operator from which we may deduce eigenfunctions, we must first quantize twistor space.

7.1 Helicity Eigenfunctions

The approach to twistor quantization proceeds in much the same way as the process of 'first quantization' in standard quantum theory. We first identify a set of canonical variables, which we promote to operators satisfying a set of commutation relations. Once commutation relations are imposed, we fix a representation in which one operator simply acts to multiply functions, and the other canonical variable becomes a differential operator. After fixing the representation, we can then construct explicit equations for some physical observable for which we can seek eigenfunctions parameterized by only one of the canonical variables.

'Twistor first quantization' follows an analogous procedure [95]. The canonical variables Z^α and $\overline{Z}_\alpha$ become operators, and we impose the commutation relations

$$[Z^\alpha, Z^\beta] = [\overline{Z}_\alpha, \overline{Z}_\beta] = 0, \tag{7.1}$$

$$[Z^\alpha, \overline{Z}_\beta] = \delta^\alpha_\beta. \tag{7.2}$$

These relations, under the momentum correspondences from Eqns. (6.1) and (6.2), are equivalent the standard commutation relations between M^{ab} and p^c. Therefore, twistor quantization can be viewed as total momentum quantization.

Now we must make a choice of representation

$$(Z^\alpha, \overline{Z}_\beta) = (Z^\alpha, -\frac{\partial}{\partial Z^\beta}) \tag{7.3}$$

or

$$(Z^\alpha, \overline{Z}_\beta) = (\frac{\partial}{\partial \overline{Z}_\alpha}, \overline{Z}_\beta). \tag{7.4}$$

Essentially we are specifying that the eigenfunctions be either holomorphic in the twistor parameter Z^α,

$$\frac{\partial}{\partial \overline{Z}_\beta} f = 0, \tag{7.5}$$

or anti-holomorphic,

$$\frac{\partial}{\partial Z^\alpha} f = 0. \tag{7.6}$$

Following Penrose [22] we choose the holomorphic representation defined by Eqns. (7.3) and (7.5). For massless free fields, helicity is the only quantum number and so the dynamics is entirely determined by the eigenfunctions of the helicity in Eqn. (6.10). When the twistor variables are quantized and are therefore non-commuting, the helicity operator becomes

$$\begin{aligned} \mathfrak{h} &= \frac{1}{4}(Z^\alpha \overline{Z}_\alpha + \overline{Z}_\alpha Z^\alpha) \\ &= -\frac{1}{2}(Z^\alpha \frac{\partial}{\partial Z^\alpha} + 2). \end{aligned} \tag{7.7}$$

where we have taken our chosen representation in the last step. The operator $z\frac{\partial}{\partial z}$ is the Euler homogeneity operator and its eigenfunctions satisfy

$$z\frac{\partial}{\partial z}f(z) = nf(z), \tag{7.8}$$

$$f(tz) = t^n f(z). \tag{7.9}$$

Thus we can consider Eqn. (7.7) as representing a shifted Euler homogeneity operator on twistor space, and thus its eigenfunctions are homogeneous twistor functions. The relation between the homogeneity n and the helicity eigenvalue h is given by

$$n = -2h - 2. \tag{7.10}$$

7.2 Penrose Transform

The Penrose transform is a helicity-dependent integral transform which maps the holomorphic eigenfunctions of the helicity operator $f(Z)$ onto solutions of the spin-h field equations on $\mathbb{M}$ [22]. Since we are interested only in real fields of spin-1 and spin-2, and thus fields whose SD and ASD components are conjugate, we require only the Penrose transform for positive helicity,

$$\varphi_{A'_1\cdots A'_{2h}}(x) = \frac{1}{2\pi i}\oint_\Gamma \pi_{A'_1}\cdots\pi_{A'_{2h}} f(Z)\,\pi_{B'}d\pi^{B'} \tag{7.11}$$

where Γ is a contour on the Celestial sphere of x (Figure 5.1b) which separates the poles of $f(Z)$. The result is a spinor field $\varphi_{A'_1\cdots A'_{2h}}(x)$ which satisfies the spin-h

massless field equation

$$\nabla^{AA'_1}\varphi_{A'_1\cdots A'_{2h}}(x) = 0$$

which is the Minkowski space (position space) representation that corresponds to the equation for helicity eigenfunctions on twistor space

$$\mathfrak{h}f(Z) = hf(Z). \tag{7.12}$$

7.2.1 Elementary States

Since the helicity operator is a shifted Euler homogeneity operator on $\mathbb{T}$, we have that the positive helicity eigenfunctions of Eqn. (7.7) are twistor functions of negative homogeneity. The Penrose transform is manifestly a contour integral on the Celestial sphere of x so there must be at least two poles in order for the integral to be non-vanishing. The simplest function which is homogeneous of degree $n = -2h - 2$ with two distinct poles is

$$f(Z) = (\overline{A}_\alpha Z^\alpha)^a (\overline{B}_\beta Z^\beta)^b, \tag{7.13}$$

where $a, b < 0$ and $a + b = -2h - 2$.

These fields can be generalized to a class of twistor functions whose singularities define Robinson congruences on $\mathbb{M}$, which are called the *elementary states* of twistor theory and were introduced by Penrose

$$f(Z) = \frac{(\bar{C}_\gamma Z^\gamma)^c (\bar{D}_\delta Z^\delta)^d}{(\bar{A}_\alpha Z^\alpha)^a (\bar{B}_\beta Z^\beta)^b} \tag{7.14}$$

where $a + b - c - d = -2h - 2$ [22]. The space-time fields corresponding to the elementary states are finite-energy, and in the null case are everywhere non-singular [93]. For integer spin fields, the expansion of a solution over the elementary states in twistor space $\mathbb{T}$ is related to the expansion over spherical harmonics in $\mathbb{M}$ through the Penrose transform [96]. These properties have made the elementary states the topic of many studies [22, 87, 97], and for many problems it is assumed that considering the elementary states is sufficient to describe any solution [98]. We will use the elementary states to explore the fundamental role of the Robinson congruence and its connection to the topology of physical systems.

7.2.2 Example: Scalar Penrose Transform

This example will show the calculation of the simplest non-trivial Penrose transform for scalar fields. It will illustrate the geometry of the Penrose transform, as well as point out some of the mathematical tricks and substitutions that will be used later to obtain our results.

Consider the following integral expression

$$\phi(x) = \frac{1}{2\pi i} \oint_{\Gamma} f\left(Z^{\alpha}\right) \pi_{C'} d\pi^{C'}, \tag{7.15}$$

where $f\left(Z^{\alpha}\right)$ given by

$$f\left(Z^{\alpha}\right) = \frac{1}{\left(A_{\alpha} Z^{\alpha}\right)\left(B_{\beta} Z^{\beta}\right)} \tag{7.16}$$

is homogeneous of degree -2. The homogeneity of f is $n = -2h_\phi - 2$, hence $h_\phi = 0$ and ϕ is a scalar. Let $A_\alpha = \left(A_A, A^{A'}\right)$ and $B_\beta = \left(B_B, B^{B'}\right)$ so that

$$\begin{aligned} A_\alpha Z^\alpha &= iA_A x^{AA'}\pi_{A'} + A^{A'}\pi_{A'} \\ &\equiv \mathcal{A}^{A'}\pi_{A'} \\ B_\beta Z^\beta &= iB_B x^{BB'}\pi_{B'} + B^{B'}\pi_{B'} \\ &\equiv \mathcal{B}^{A'}\pi_{B'}, \end{aligned} \tag{7.17}$$

where we have used the incidence relation to get $Z^\alpha = (ix^{AA'}\pi_{A'}, \pi_{A'})$. We also have

$$\begin{aligned} \pi_{C'} d\pi^{C'} &= \pi_{C'} d\pi_{D'} \varepsilon^{C'D'} \\ &= \pi_{0'} d\pi_{1'} - \pi_{1'} d\pi_{0'} \\ &= (\pi_{0'})^2 d\left(\frac{\pi_{1'}}{\pi_{0'}}\right). \end{aligned} \tag{7.18}$$

Moreover, the expressions

$$\begin{aligned} \frac{1}{\pi_{0'}}\mathcal{A}^{A'}\pi_{A'} &= \mathcal{A}^{0'} + \mathcal{A}^{1'}\left(\frac{\pi_{1'}}{\pi_{0'}}\right) \\ \frac{1}{\pi_{0'}}\mathcal{B}^{B'}\pi_{B'} &= \mathcal{B}^{0'} + \mathcal{B}^{1'}\left(\frac{\pi_{1'}}{\pi_{0'}}\right) \end{aligned} \tag{7.19}$$

imply that the Penrose transform becomes an integral manifestly over $\mathbb{CP}^1$. Thus,

$$\begin{aligned} \phi(x) &= \frac{1}{2\pi i}\oint_\Gamma \frac{d\left(\frac{\pi_{1'}}{\pi_{0'}}\right)}{\left(\mathcal{A}^{0'} + \mathcal{A}^{1'}\left(\frac{\pi_{1'}}{\pi_{0'}}\right)\right)\left(\mathcal{B}^{0'} + \mathcal{B}^{1'}\left(\frac{\pi_{1'}}{\pi_{0'}}\right)\right)} \\ &= \frac{1}{2\pi i \mathcal{A}^{1'}\mathcal{B}^{1'}}\oint_\Gamma \frac{d\zeta}{(\mu+\zeta)(\nu+\zeta)}, \end{aligned}$$

where the projective coordinate and poles are represented by

$$\begin{aligned} \zeta &\equiv \frac{\pi_{1'}}{\pi_{0'}} \\ \mu &\equiv \frac{\mathcal{A}^{0'}}{\mathcal{A}^{1'}} \\ \nu &\equiv \frac{\mathcal{B}^{0'}}{\mathcal{B}^{1'}}. \end{aligned}$$

After the variable substitutions the integral is a contour integral evaluated using Cauchy's integral theorem for a contour Γ enclosing the pole $-\mu$

$$\begin{aligned} \phi(X) &= \frac{1}{2\pi i \mathcal{A}^{1'}\mathcal{B}^{1'}} \oint_{\Gamma} \frac{d\zeta}{(\mu+\zeta)\,(\nu+\zeta)} \\ &= \frac{1}{\mathcal{A}^{1'}\mathcal{B}^{1'}} \frac{1}{(\nu-\mu)} \\ &= \frac{2}{A_A B^A (x^a - y^a)(x_a - y_a)} \end{aligned}$$

where the point y is given as

$$y^{AA'} = i\frac{A^{A'}B^A - B^{A'}A^A}{A_B B^B}. \tag{7.20}$$

The geometry of the Penrose transform is shown in Figure 7.1a. The contour integration turns the pole structure at each point x^a into a specific field configuration on $\mathbb{M}$. The factors $(A_\alpha Z^\alpha)$ and $\left(B_\beta Z^\beta\right)$ determine the poles of the twistor function $f(Z)$ and are represented in $\mathbb{PT}$ by the planes A and B. The planes intersect in a $\mathbb{CP}^1$ which corresponds to some y^a in $\mathbb{CM}$. The point at which we are computing the field is x and is represented in $\mathbb{PT}$ as another $\mathbb{CP}^1$ which meets A and B at the points μ and ν. The integral is taken over the Celestial sphere of x, as shown in Figure 7.1b, where the contour Γ separates the poles.

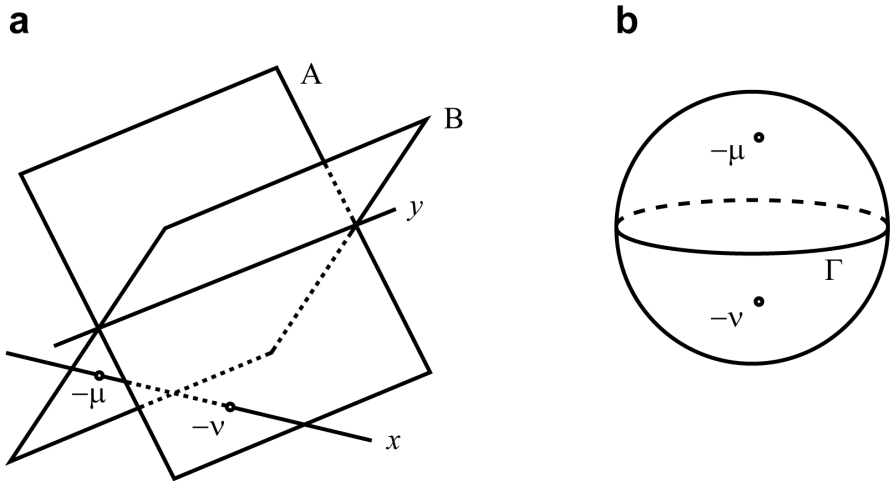

Figure 7.1: Geometry of the integral in the Penrose transform. **a** In $\mathbb{PT}$, A and B are given as planes on which $f(Z)$ is singular, and they intersect at a $\mathbb{CP}^1$ describing a point $y \in \mathbb{CM}$. The point x at which we are computing φ is represented as a $\mathbb{CP}^1$ which meets A and B at the poles $-\mu$ and $-\nu$ of $f(Z)$. **b** The Celestial sphere of x, where the contour Γ separates the poles.

Chapter 8

Computational Methods for Gravitational Fields

In the early chapters of this thesis, we discussed electromagnetic solutions with linked and knotted field lines. In the case of electromagnetic radiation, the physical properties of the fields are well understood. We can generalize these solutions to fields of spin-N using the Penrose transform. Once these new solutions are constructed, the goal is to understand their topological structure and analyze their properties through methods that make use of the analogous relationship with electromagnetism.

Here we present a method for visualizing and characterizing the structure of topologically non-trivial fields of spin-2. The visualization techniques are based on recent work by Nichols, *et al.* [24] that involves decomposing the curvature tensor to find the gravitational lines of force, which are the analog of electromagnetic field lines. Our research group has developed a Mathematica software package to calculate gravitational radiation solutions using twistor integral methods and

visualize their lines of force. I would like to acknowledge Alex Wickes, who worked with me on applying these gravito-electromagnetic techniques to analyze knotted field structures and developing the Mathematica code to make the visualizations.

8.1 Gravito-electromagnetism

Classical electromagnetism resides in the spin-1 sector of Eqn. (5.45) [39] with source-free field equation and field strength spinor given by

$$\nabla^{AA'}\varphi_{A'B'} = 0,$$
$$F_{A'B'AB} = \varphi_{A'B'}\epsilon_{AB} + c.c. \tag{8.1}$$

The standard electric and magnetic fields are recovered by decomposing F_{ab} using a 4-velocity u^a so that

$$\mathcal{E}_a = F_{ab}u^b,$$
$$\mathcal{B}_a = - * F_{ab}u^b \tag{8.2}$$

where $*$ denotes the Hodge dual $*F_{ab} = \frac{1}{2}\varepsilon_{ab}{}^{cd}F_{cd}$. Taking $u^a = (1,0,0,0)$ we have that

$$F_{ab} = \begin{pmatrix} 0 & E_x & E_y & E_z \\ -E_x & 0 & -B_z & B_y \\ -E_y & B_z & 0 & -B_x \\ -E_z & -B_y & B_x & 0 \end{pmatrix}. \tag{8.3}$$

Linearized general relativity makes up the spin-2 sector of the spin-h equations [39]. The field equation and associated field strength spinor are given by

$$\nabla^{AA'}\varphi_{A'B'C'D'} = 0,$$

$$C_{A'B'C'D'ABCD} = \varphi_{A'B'C'D'}\epsilon_{AB}\epsilon_{CD} + c.c. \tag{8.4}$$

In analogy with the spin-1 case, following Maartens, *et al.* [23] and Nichols, *et al.* [24], we decompose the Weyl tensor and its dual by projection onto space-like foliations orthogonal to a 4-velocity u^a. This gives the gravito-electric and gravito-magnetic fields

$$E_{ab} = \gamma_a{}^r\gamma_b{}^s C_{rcsd}u^c u^d$$

$$B_{ab} = -\gamma_a{}^r\gamma_b{}^s * C_{rcsd}u^c u^d, \tag{8.5}$$

where $\gamma_a{}^b$ is the spatial projection operator defined by $\gamma_{ab} = \eta_{ab} - u_a u_b$ and again $*$ is the Hodge dual operator, so that $*C_{abcd} = \frac{1}{2}\varepsilon_{abrs}C^{rs}{}_{cd}$. Taking $u^a = (1, 0, 0, 0)$ we define the spatial tensors

$$E_{ij} = C_{i0j0},$$

$$B_{ij} = - * C_{i0j0}. \tag{8.6}$$

The symmetric traceless tensors E_{ij} and B_{ij} are called the tidal and frame-drag fields, respectively. Two orthogonal observers separated by a small spatial vector $\boldsymbol{\xi}$ will experience a relative tidal acceleration given by

$$\Delta a^i = -E^i{}_j\xi^j \tag{8.7}$$

and a gyroscope at the tip of $\boldsymbol{\xi}$ will precess with angular velocity

$$\Delta\Omega^i = B^i{}_j \xi^j \tag{8.8}$$

relative to inertial frames at the tail of $\boldsymbol{\xi}$. Since the tidal and frame-drag fields are symmetric and traceless, each may be characterized entirely by its eigensystem. Thus, if $\boldsymbol{v}$ is an eigenvector of E_{ij} or B_{ij} then the integral curves of $\boldsymbol{v}$ are the gravitational analog of field lines. The tidal field stretches or compresses objects, and its associated field lines are referred to as tendex lines. The frame-drag field rotates gyroscopes, and its associated field lines are referred to as vortex lines. The tidal field has an associated eigenvalue $E_{\boldsymbol{v}}$ which has a physical interpretation given by the tidal acceleration Eqn. (8.7). Thus, if the tendex eigenvalue is negative (respectively, positive) then an object oriented along the tendex line is stretched (compressed) along the tendex line. Similar relations hold for the frame-drag field whose eigenvalues are interpreted using Eqn. (8.8), where an object oriented along a vortex line observes counter-clockwise (clockwise) precession of gyroscopes around the vortex line.

8.2 Computational Methods

The gravitational fields are constructed and decomposed analytically in Mathematica, and the lines of force are then plotted numerically. The code takes as input a twistor function for an elementary state in the form of Eqn. (7.14), with

specific values of $\bar{A}_\alpha$, $\bar{B}_\beta$, $\bar{C}_\gamma$, and $\bar{D}_\delta$, then calculates the corresponding spinor field on space-time from the Penrose transform (Eqn. (7.11)). This is converted into the Weyl curvature spinor using Eqn. (8.4) and then to tensor form using the Infeld-van der Waerden symbols. The Weyl curvature tensor is decomposed into the tidal and frame-drag tensors according to Eqn. (8.6).

To visualize the gravitational lines of force, we need to plot the integral curves of the eigenvectors of the tidal and frame-drag tensors. For fields described by relatively simple expressions, such as the Type N hopfions that will be presented in Chapter 9, the eigensystem can be computed analytically using the command `Eigensystem[m]` for a matrix m. We then plot a specific field line by choosing a starting point and then numerically integrating along a variable that parameterizes the curve. The magnitude of eigenvalue is depicted by the color scale of the plot. For more complicated fields, including the Type N torus knots in Chapter 10 and the fields of other Petrov Types in Chapter 11, we must find the eigenvectors numerically. This results in a set of values describing the eigensystem at different points in space, and thus requires a modified version of the plotting routine, which will be described later.

We also wrote a version of this code to calculate EM fields, which requires a twistor function of the correct homogeneity as input, then performs the above calculations with the analogous equations for spin-1 fields. It also plots the lines of force, but without the color scaling as in the spin-2 case.

8.2.1 Visualization Method

In the study of differential equations, flow functions give a formal description of the continuous motion of points over time. They are fundamental in the solution of ODEs and are often used to study motion of particles in fluids. Here we apply this concept to find the lines of force for electromagnetic and gravitational fields.

An autonomous ordinary differential equation is an ODE that does not depend explicitly on t. Given an initial value problem for an autonomous ODE

$$\frac{dx}{dt} = f(x(t)) \tag{8.9}$$
$$x(t_0) = x_0,$$

the *flow function* of the ODE is defined as the solution of Eqn. (8.9), denoted as $\phi_t(x_0)$, with the given initial condition, so that

$$\phi_0(x_0) = x_0,$$
$$\phi_{t'}(\phi_t(x)) = \phi_{t+t'}(x)$$

and

$$\frac{d}{dt}\phi_t(x_0) = f(\phi_t(x_0)) \tag{8.10}$$

for all t for which the flow function is defined. In Mathematica syntax, this could be written as

```
\[Phi][f_, x0_, tf_, opts___] :=
    Module[{t, x}, x[tf] /. NDSolve[{x'[t] == f[x[t], t],
    x[0] == x0}, x, {t, 0, tf}, opts][[1]] ]
```

where x is the explicit variable and $t \in [0, tf]$ is the implicit variable. We can adapt this type of ODE solver to plot field lines, by choosing a starting point then "evolving" along the variable that parameterizes the integral curve of the vector field. The function *plotFieldLine* plots the field lines on the interval $[ti, tf]$ for the ODE in Eqn. (8.9) using the initial value $x(0) = x0$ and is defined as

```
plotFieldLine[f_, x0_, {ti_, tf_}, opts___] :=
    Module[{sln, t, x}, sln = NDSolve[{x'[t] == f[x[t], t],
    x[0] == x0}, x, {t, ti, tf}, MaxSteps -> \[Infinity],
    WorkingPrecision -> MachinePrecision][[1]];
  ParametricPlot3D[x[t] /. sln, {t, ti, tf}, opts] ]
```

where f is the normalized vector field, the implicit variable t is the parameter along the field line (not time), and the parameter length that appears in the plot is $(tf - ti)$.

The variable `opts` contains all of the plotting style options. This allows the user to change the plot range, lighting and viewpoint. This also includes the color scaling, which in our program represents the magnitude of the eigenvalue, or the field strength.

A note should be made about the choice of the initial points for the numerical integration. The goal is to understand the topological structure of the field lines, and thus the integral curves shown in the plot should exemplify the overall structure. For example, when visualizing hopfions it is useful to input a list of n evenly spaced points about a circle of radius r in a plane whose normal is parallel to the central axis of the Hopf fibration. This will correspond to a set of evenly spaced

circular fibers that lie on the same toroidal surface. Choosing the initial points from a circle with a different radius will result in another set of circular fibers all lying on another toroidal surface.

When the eigensystem cannot be found analytically and must be computed numerically, there is an important issue to address. Eigenvectors are equivalent up to a nonzero scalar multiple, hence the overall sign and magnitude of an eigenvector is arbitrary. Thus, if the eigenvector is multiplied by a different scalar multiple at different points in space the integral curves will not seem continuous, and any attempts to plot them will not give meaningful results. Although many programs have built-in methods for finding eigenvectors, most do not have the functionality to plot eigenvectors obtained numerically.

Numerical algorithms for solving a differential equation $\dot{\vec{y}} = \vec{f}(t, y)$, such as the Runge-Kutta Method, usually follow a step-by-step process. Each intermediate step takes the previous data $\vec{y}_n$ and t_n as new input, which is used to calculate the next increment typically of the form

$$\vec{k}_i = f(t_n + \varepsilon_i(dt), \vec{y}_n + \vec{\delta}_i(dt, \vec{k}_j)). \tag{8.11}$$

This is used to approximate the values of $\vec{y}_{n+1}$ with $t_{n+1} = t_n + dt$, which is then taken as the input for the next step. To resolve the problems caused by the ambiguity in the sign and magnitude of the eigenvectors, we redefine our

increment. Each time an increment $\vec{k}_i$ is computed, it is replaced by

$$\vec{k}'_i = \mathrm{sgn}(\vec{k}_i \cdot \vec{f}(t_n, y_n))\vec{k}_i \tag{8.12}$$

and this new increment is used for the next step in the computation.

Using this procedure, we can define a Mathematica function that solves ODEs with a modified 4th order Runge-Kutta method as

```
eigCRK4[]["Step"[rhs_, t_, dt_, y_, yp_]] :=
   Module[{k0, k1, k2, k3, ypNew},
   k0 = yp;
   k1 = rhs[t + dt/2, y + dt k0/2]; If[k1.yp < 0, k1 = -k1];
   k2 = rhs[t + dt/2, y + dt k1/2]; If[k2.yp < 0, k2 = -k2];
   k3 = rhs[t + dt, y + dt k2]; If[k3.yp < 0, k3 = -k3];
   ypNew = Normalize[(k0 + 2  k1 + 2  k2 + k3)/6];
   {dt, dt ypNew, ypNew}];
eigCRK4[___]["DifferenceOrder"] := 3;
eigCRK4[___]["StepMode"] := Fixed;
```

The integral curves for any arbitrary vector field can be plotted as before, now using `NDSolve` with the argument `Method -> eigCRK4`.

8.3 Summary

We have described the methods we will use for calculating and plotting gravitational radiation solutions in Mathematica. Fields of spin-N are constructed analytically from twistor functions via the Penrose transform. The visualization techniques are based on the tidal tensor analogy with electromagnetism, whereby the Weyl curvature tensor is first decomposed into the fields seen by a time-like

observer. We then find the eigenvectors of the tidal and frame-drag tensors, and the integral curves of these vector fields are the lines of force experienced by this observer, called tendex and vortex lines, respectively.

We will now return to our discussion of the Penrose transform and how it can be used to generate spin-2 fields based on different topological configurations. The computational techniques based on the physical decomposition of these solutions will serve as a useful aid in visualizing and analyzing the topology of their field line structure.

Chapter 9

Hopfions in Gravity

As discussed in Chapter 2, the EM hopfion is a topologically non-trivial solution to the vacuum Maxwell equations with the property that any two field lines belonging to either the electric, magnetic, or Poynting vector fields (EBS fields) are closed and linked exactly once. The most striking and characteristic feature of this particular field configuration is the existence of an exceptional constant-time hyperplane wherein the EBS fields are tangent to three orthogonal Hopf fibrations. Using twistor methods we find the spin-h generalization of the EM hopfion. Furthermore, we analyze the spin-2 solution within the framework of gravito-electromagnetism and show that the topology is manifest in the tendex and vortex lines. By decomposing the spin-2 field into spatial gravito-electric and gravito-magnetic tensors, we characterize its topological structure and evolution in terms of the EM hopfion.

9.1 Penrose Transform for Spin-h Hopfions

Consider the positive helicity eigenfunctions of Eqn. (7.13), and recall that these must be twistor functions of negative homogeneity. In the case of spin-1 and spin-2 the spinor fields $\varphi_{A'B'}(x)$ and $\varphi_{A'B'C'D'}(x)$ represent the Penrose transform of twistor functions[1] of homogeneity -4 and -6 respectively and correspond to the $SL(2,\mathbb{C})$ representations of the field strength tensor F_{ab} of electromagnetism and the Weyl tensor C_{abcd} of general relativity.

We will calculate the Penrose transform with $f(Z)$ given by

$$f(Z) = (A_\alpha Z^\alpha)^{-1}(B_\beta Z^\beta)^{-2h-1}. \tag{9.1}$$

Let A_α and B_α be dual twistors associated to the spinor fields $\mathcal{A}^{A'}$ and $\mathcal{B}^{B'}$ as in Eqn. (7.17) so that

$$\begin{aligned} A_\alpha Z^\alpha &= iA_A x^{AA'}\pi_{A'} + A^{A'}\pi_{A'} \\ &\equiv \mathcal{A}^{A'}\pi_{A'} \\ B_\beta Z^\beta &= iB_B x^{BB'}\pi_{B'} + B^{B'}\pi_{B'} \\ &\equiv \mathcal{B}^{A'}\pi_{B'}, \end{aligned}$$

Recall from Eqn. (7.18) the measure can be written in the form

$$\pi_{C'} d\pi^{C'} = (\pi_{0'})^2 d\zeta.$$

[1]Since the spinor fields $\varphi_{A'B'}(x)$ and $\varphi_{A'B'C'D'}(x)$ are obtained via complex contour integrals there exists a certain freedom in their twistor descriptions. A detailed exploration of this fact leads to the notion of complex sheaf cohomology.

We also have the relations from Eqn. (7.19)

$$\frac{1}{\pi_{0'}}\mathcal{A}^{A'}\pi_{A'} = \mathcal{A}^{0'} + \mathcal{A}^{1'}\zeta,$$
$$\frac{1}{\pi_{0'}}\mathcal{B}^{A'}\pi_{A'} = \mathcal{B}^{0'} + \mathcal{B}^{1'}\zeta.$$

Introducing the canonical spin bases $\{o_{A'}, \iota_{A'}\}$ into the primed spin space S' we have that

$$\begin{aligned}\pi_{A'} &= \pi_{0'}o_{A'} + \pi_{1'}\iota_{A'} \\ &= \pi_{0'}(o_{A'} + (\frac{\pi_{1'}}{\pi_{0'}})\iota_{A'}) \\ &= \pi_{0'}(o_{A'} + \zeta\iota_{A'}).\end{aligned} \tag{9.2}$$

Thus

$$\begin{aligned}\varphi_{A'_1\cdots A'_{2h}}(x) &= \frac{1}{2\pi i}\oint_\Gamma \frac{(o_{A_1} + (\frac{\pi_{1'}}{\pi_{0'}})\iota_{A'_1})\cdots(o_{A_{2h}} + (\frac{\pi_{1'}}{\pi_{0'}})\iota_{A'_{2h}})}{(\mathcal{A}^{0'} + \mathcal{A}^{1'}(\frac{\pi_{1'}}{\pi_{0'}}))(\mathcal{B}^{0'} + \mathcal{B}^{1'}(\frac{\pi_{1'}}{\pi_{0'}}))^{2h+1}} d(\frac{\pi_{1'}}{\pi_{0'}}) \\ &= \frac{1}{2\pi i\mathcal{A}^{1'}(\mathcal{B}^{1'})^{2h+1}}\oint_\Gamma \frac{(o_{A_1} + \zeta\iota_{A'_1})\cdots(o_{A_{2h}} + \zeta\iota_{A'_{2h}})}{(\mu+\zeta)(\nu+\zeta)^{2h+1}} d\zeta\end{aligned} \tag{9.3}$$

where as before $\zeta = \pi_{1'}/\pi_{0'}$, $\mu = \mathcal{A}^{0'}/\mathcal{A}^{1'}$, and $\nu = \mathcal{B}^{0'}/\mathcal{B}^{1'}$ represent the projective coordinate and poles respectively.

After the variable substitutions, the integral is straightforward. Taking the contour Γ to enclose the pole $-\mu$ we have

$$\begin{aligned}
\varphi_{A'_1\cdots A'_{2h}}(x) &= \frac{1}{\mathcal{A}^{1'}(\mathcal{B}^{1'})^{2h+1}} \operatorname*{Res}_{\zeta=-\mu} \frac{(o_{A_1}+\zeta\iota_{A'_1})\cdots(o_{A_{2h}}+\zeta\iota_{A'_{2h}})}{(\mu+\zeta)(\nu+\zeta)^{2h+1}} \\
&= \frac{1}{\mathcal{A}^{1'}(\mathcal{B}^{1'})^{2h+1}} \frac{(o_{A'_1}-\mu\iota_{A'_1})\cdots(o_{A'_{2h}}-\mu\iota_{A'_{2h}})}{(\nu-\mu)^{2h+1}} \\
&= \frac{(\mathcal{A}^{1'}o_{A'_1}-\mathcal{A}^{0'}\iota_{A'_1})\cdots(\mathcal{A}^{1'}o_{A'_{2h}}-\mathcal{A}^{0'}\iota_{A'_{2h}})}{(\mathcal{A}^{1'}\mathcal{B}^{0'}-\mathcal{A}^{0'}\mathcal{B}^{1'})^{2h+1}} \\
&= \frac{1}{(\epsilon_{A'B'}\mathcal{A}^{A'}\mathcal{B}^{B'})^{2h+1}} \mathcal{A}_{A'_1}\cdots\mathcal{A}_{A'_{2h}} \\
&= \left(\frac{2}{A_A B^A (x^a-y^a)(x_a-y_a)}\right)^{2h+1} \mathcal{A}_{A'_1}\cdots\mathcal{A}_{A'_{2h}} \qquad (9.4)
\end{aligned}$$

where $A_A B^A$ is a constant we will call Ω, and the point y is given in Eqn. (7.20).

9.2 EM Hopfion

For $h = 1$, Eqn. (9.4) becomes

$$\varphi_{A'B'}(x) = \left(\frac{2}{\Omega|x-y|^2}\right)^3 \mathcal{A}_{A'}\mathcal{A}_{B'} \qquad (9.5)$$

where $\mathcal{A}_{A'}$ defines the doubly degenerate principle null direction of F_{ab}. Choosing

$$\overline{A}_a = (-i\sqrt{2}, \sqrt{2}, -i, 1), \qquad (9.6)$$

$$\overline{B}_\beta = \frac{\pi^{1/3}}{2^{4/3}}(-\sqrt{2}, i\sqrt{2}, -1, i) \qquad (9.7)$$

reproduces precisely the EM hopfion of Rañada [7]. The expressions for the electric and magnetic fields can be conveniently expressed by a Riemann-Silberstein

vector,

$$\begin{aligned}\boldsymbol{F_R} &= \boldsymbol{E_R} + i\boldsymbol{B_R} \\ &= \frac{4}{\pi(-(t-i)^2+r^2)^3}\begin{pmatrix}(x-iz)^2-(t-i+y)^2\\ 2(x-iz)(t-i+y)\\ i(x-iz)^2+i(t-i+y)^2\end{pmatrix},\end{aligned} \tag{9.8}$$

where $r^2 = x^2+y^2+z^2$. The energy density and Poynting vector field are

$$U_R = \frac{16(1+x^2+(t+y)^2+z^2)^2}{\pi^2(1+2(t^2+r^2)+(t^2-r^2)^2)^3}, \tag{9.9}$$

$$\boldsymbol{S_R} = \frac{U_R}{(1+x^2+(t+y)^2+z^2)}\begin{pmatrix}2(x(t+y)+z)\\ 1+(t+y)^2-x^2-z^2\\ 2(z(t+y)-x)\end{pmatrix}. \tag{9.10}$$

A visualization of these solutions is presented in row 1 of Figures 9.1 and 9.2 and the formulas are displayed here for comparison with the GEM field configurations derived in the next section.

9.3 GEM Hopfion

The gravito-electromagnetic hopfion (GEM hopfion) is constructed in the same fashion as the EM hopfion since linearized gravitational fields are taken to be spin-2 fields on $\mathbb{M}$. Thus, taking $h = 2$ in Eqn. (9.4) gives

$$\varphi_{A'B'C'D'}(x) = \left(\frac{2}{\Omega|x-y|^2}\right)^5 \mathcal{A}_{A'}\mathcal{A}_{B'}\mathcal{A}_{C'}\mathcal{A}_{D'} \tag{9.11}$$

where $\mathcal{A}_{A'}$ defines the totally degenerate principle null directions of C_{abcd}, indicating this is a Petrov Type N linearized gravitational field. Taking the dual twistors $\overline{A}_\alpha$ and $\overline{B}_\beta$ to be the same as in the EM hopfion we construct the Weyl curvature from Eqn. (8.4). Then we perform the gravito-electric and gravito-magnetic decompositions as in Eqn. (8.6).

The tidal and frame-drag fields are characterized by their spectral decomposition which provides a three-dimensional picture of the space-time via the integral curves of their eigenvector fields and their physical interpretations given by Eqns. (8.7) and (8.8). Performing the decomposition we find that both fields possess an eigenvalue structure $\{+\Lambda, -\Lambda, 0\}$ corresponding respectively to the eigenvectors $\{\boldsymbol{E}_+, \boldsymbol{E}_-, \boldsymbol{E_0}\}$ and $\{\boldsymbol{B}_+, \boldsymbol{B}_-, \boldsymbol{B_0}\}$. The magnitude of the eigenvalue

$$|\Lambda(x)| = \frac{2^{8/3}(1 + x^2 + (y+t)^2 + z^2)^2}{\pi^{5/3}(1 + 2(t^2 + r^2) + (t^2 - r^2)^2)^{5/2}} \tag{9.12}$$

determines the field strength for both the tidal and frame-drag fields.

Considering first the eigenvector fields which correspond to the zero eigenvalue, we find

$$\begin{aligned} \boldsymbol{E_0} = \boldsymbol{B_0} &= \begin{pmatrix} 2(x(t+y)+z) \\ 1 + (t+y)^2 - x^2 - z^2 \\ 2(z(t+y)-x) \end{pmatrix} \\ &= (1 + x^2 + (t+y)^2 + z^2)\frac{\boldsymbol{S_R}}{|\boldsymbol{S_R}|} \end{aligned} \tag{9.13}$$

which is, up to an overall scaling function, the Poynting vector of the EM hopfion. Constructing Riemann-Silberstein structures for the remaining fields

$$\boldsymbol{F_{GE}} = \boldsymbol{E_-} + i\boldsymbol{E_+}, \tag{9.14}$$

$$\boldsymbol{F_{GB}} = \boldsymbol{B_-} + i\boldsymbol{B_+}, \tag{9.15}$$

we find that

$$\boldsymbol{F_{GE}} = e^{i\pi/4}\boldsymbol{F_{GB}} \tag{9.16}$$

$$= e^{iArg(\vartheta)}\boldsymbol{F_R}, \tag{9.17}$$

where

$$\vartheta = \sqrt{-(t-i)^2 + r^2}. \tag{9.18}$$

This defines the tidal and frame-drag fields in terms of the EM hopfion. Eqn. (9.16) shows that the frame-drag field is a rotation of the tidal field about the Poynting vector of the EM hopfion. Thus in passing to spin-2 we obtain two independent gravitational hopfion structures: a gravito-electric hopfion and a gravito-magnetic hopfion which differ simply by a global rotation. Eqns. (9.17) and (9.18) show that the tidal field is a local duality transformation of the EM hopfion. At $t = 0$, $Arg(\vartheta) = 0$ and thus provides no duality transformation. Hence the tendex structure of the tidal field is the same as the field line structure of the EM hopfion. Furthermore, the vortex lines are the same as the tendex lines but rotated by 45° in the xy-plane. Ergo, the $t = 0$ tendex and vortex configuration is given by the

six Hopf fibrations of Figure 9.1 (rows 2 and 3) so that for each fixed eigenvalue the associated tendex (or vortex) lines are closed and linked exactly once. For $t \neq 0$, ϑ is complex and hence the tendex lines differ from those of the EM hopfion by a local duality transformation as shown in Figure 9.2, with the vortex structure different again by only a rotation of 45°.

For electromagnetic fields, there are two quantities that are invariant under local duality transformations: the energy density and Poynting vector. For the EM hopfion, these are given in Eqns. (9.9) and (9.10). In direct analogy with the local duality invariants of electromagnetism, a covariant super-energy density and super-Poynting vector that are invariant under a local duality transformation can be defined [23]. For the GEM hopfion, we find the super-energy density and super-Poynting vector are given by

$$\begin{aligned} U_G &= \frac{1}{2}(E_{ab}E^{ab} + B_{ab}B^{ab}) \\ &= \frac{64 \cdot 2^{1/3}(1 + x^2 + (t+y)^2 + z^2)^4}{\pi^{10/3}(1 + 2(t^2 + r^2) + (t^2 - r^2)^2)^5}, \end{aligned} \tag{9.19}$$

$$\begin{aligned} (S_G)_a &= \epsilon_{abc}E^b_d B^{cd} \\ &= \frac{U_G}{(1 + x^2 + (t+y)^2 + z^2)} \begin{pmatrix} 2(x(t+y) + z) \\ 1 + (t+y)^2 - x^2 - z^2 \\ 2(z(t+y) - x) \end{pmatrix}. \end{aligned} \tag{9.20}$$

There is a striking similarity between the local duality invariants for the spin-1 and spin-2 cases, which differ only by the power of the scalar factor that shows the energy falls off more rapidly for the higher spin fields.

9.4 Summary

According to Robinson, for each null shear-free geodesic congruence in Minkowski space there exists a null solution of Maxwell's equations [99]. Indeed, it has recently been shown using Kerr's theorem that the EM hopfion is derivable via the method of Robinson [9]. Here we took a closer look at the fundamentals of twistor theory and showed that the EM hopfion represents the simplest non-trivial classical solution to the spin-1 massless field equation in twistor space. This enabled the extension of the spin-1 EM hopfion to solutions of the spin-h equations. Taking the $h = 2$ solution as a linearized Weyl tensor, and aided by the concept of tendex and vortex lines as recently developed for the visualization of solutions in general relativity, we investigated the physical properties of the spin-2 GEM hopfion and characterized its evolution in terms of the Riemann-Silberstein structure of the EM hopfion.

These results capitalize on of one of the greatest strengths of the twistor program. It is precisely the unifying power of the twistor philosophy, deeply connected

with the concept of spin, which allows for such a physically sweeping generalization of an EM radiation field to both matter and linearized gravitational fields.

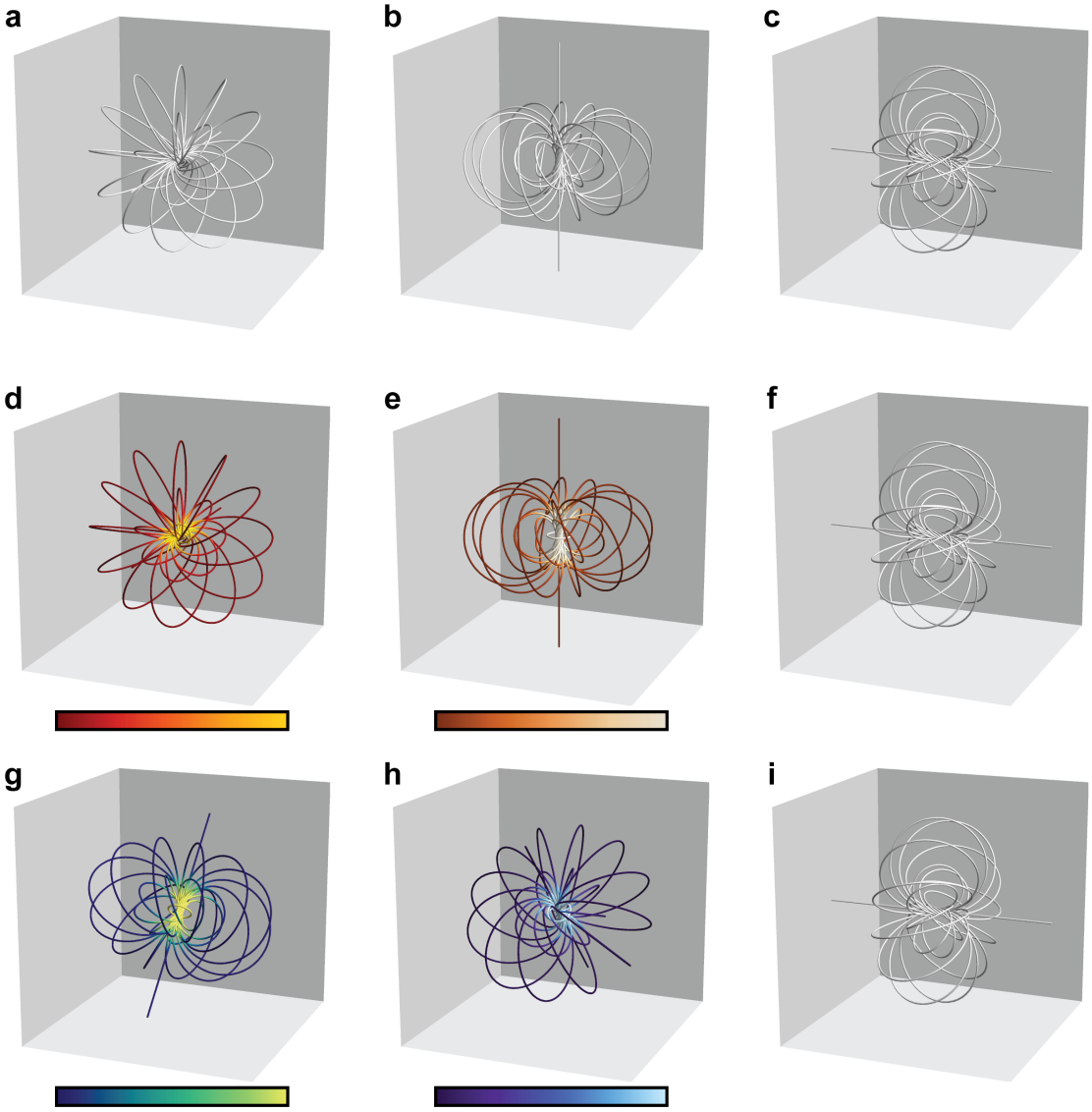

Figure 9.1: A comparison of the spin-1 (EM) and spin-2 (gravity) hopfions at $t = 0$. The first row is the EM hopfion: **a** the electric field, **b** the magnetic field, and **c** the Poynting vector field. The second row is the gravito-electric hopfion: **d** the negative eigenvalue field E_-, **e** the positive eigenvalue field E_+, and **f** the zero eigenvalue field E_0. The third row is the gravito-magnetic hopfion: **g** the negative eigenvalue field B_-, **h** the positive eigenvalue field B_+, and **i** the zero eigenvalue field B_0. The color scale indicates magnitude of the eigenvalue, with lighter colors indicating a higher magnitude.

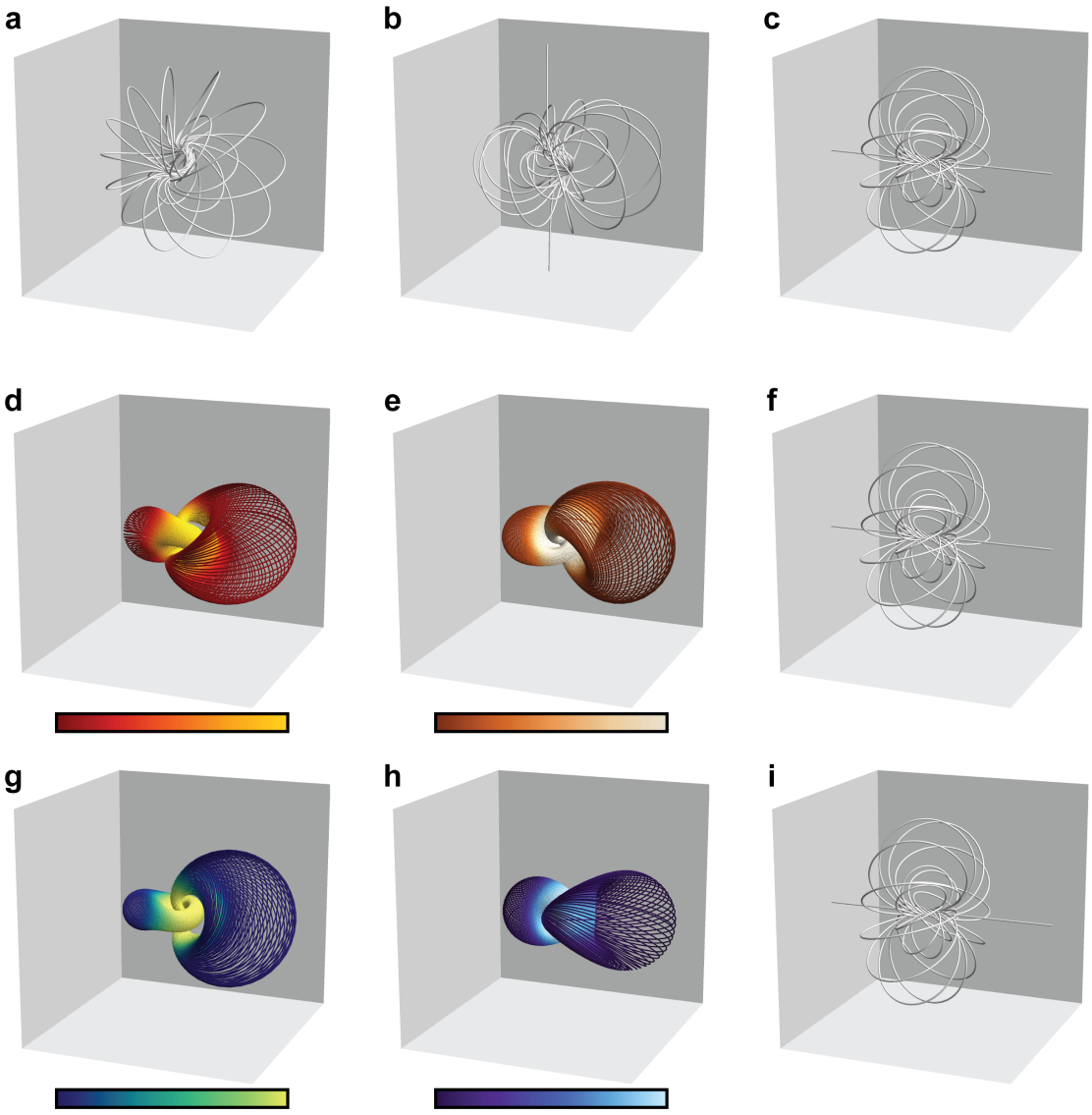

Figure 9.2: A comparison of the spin-1 (EM) and spin-2 (gravity) hopfions at $t = 1$, with layout the same as in Figure 9.1.

Chapter 10

Knots in Gravity

In this chapter, we show that field configurations based on all the torus knots are contained within the elementary states of twistor theory. The Hopf fibration appears as the simplest case whereby the linked and knotted toroidal structure degenerates down to the hopfion configuration. This generalization leads to a construction for spin-h fields based on torus knots. We will focus our analysis on the spin-1 and spin-2 fields, where the topology is physically manifest in the lines of force.[1]

10.1 Parameterization of the Elementary States

We will relate the torus knot topology to the twistor elementary states, so that we can use the Penrose transform to obtain solutions to the EM and gravitational spinor field equations.

[1]For the Weyl fields, the linked and knotted topology appears in the current.

Consider the twistor functions from Eqn. (7.14) which correspond to the elementary states

$$f(Z) = \frac{(\bar{C}_\gamma Z^\gamma)^c (\bar{D}_\delta Z^\delta)^d}{(\bar{A}_\alpha Z^\alpha)^a (\bar{B}_\beta Z^\beta)^b}.$$

Choosing $a = 1$ yields null or Type N solutions with $b = 2h + 1 + c + d$ to give the correct homogeneity $n = -2h - 2$ for a solution with helicity h. We will show that the class of generating functions of the form

$$f(Z) = \frac{(\bar{C}_\gamma Z^\gamma)^{h(n_p-1)} (\bar{D}_\delta Z^\delta)^{h(n_t-1)}}{(\bar{A}_\alpha Z^\alpha)(\bar{B}_\beta Z^\beta)^{h(n_p+n_t)+1}}, \tag{10.1}$$

lead to field configurations with a torus knot topology, where n_p and n_t correspond to the poloidal and toroidal winding numbers.[2]

We choose the dual twistors

$$\begin{aligned} \bar{A}_\alpha &= \imath(0, \sqrt{2}, 0, 1) \\ \bar{B}_\beta &= \imath(-\sqrt{2}, 0, -1, 0) \\ \bar{C}_\gamma &= (0, -\sqrt{2}, 0, 1) \\ \bar{D}_\delta &= \imath(-\sqrt{2}, 0, 1, 0). \end{aligned} \tag{10.2}$$

$\bar{A}_\alpha$ and $\bar{C}_\gamma$ correspond to Robinson congruences with opposite twist, both with central axes aligned along the $+\hat{z}$-direction. $\bar{B}_\beta$ and $\bar{D}_\delta$ correspond to Robinson congruences with opposite twist, but in the $-\hat{z}$-direction. This choice leads to

[2]We use the conventions from Ref. [21]. Also, there is factor of $4n_t n_p$ in Ref. [19] that does not appear in our construction, but it does not affect the topology.

spin-h fields which propagate $+\hat{z}$-direction with field line configurations that are based on a torus knot structure.

10.2 Penrose Transform for Spin-h Torus Knots

We will calculate the Penrose transform

$$\varphi_{A'_1\cdots A'_{2h}}(x) = \frac{1}{2\pi i}\oint_\Gamma \pi_{A'_1}\cdots\pi_{A'_{2h}} f(Z)\pi_{B'}d\pi^{B'}$$

with the twistor function given by Eqn. (10.1)

$$f(Z) = \frac{(\bar{C}_\gamma Z^\gamma)^{h(n_p-1)}(\bar{D}_\delta Z^\delta)^{h(n_t-1)}}{(\bar{A}_\alpha Z^\alpha)(\bar{B}_\beta Z^\beta)^{h(n_p+n_t)+1}}.$$

Let $\overline{A}_\alpha$ be a dual twistor as in Eqn. (7.17) so that

$$\begin{aligned} A_\alpha Z^\alpha &= iA_A x^{AA'}\pi_{A'} + A^{A'}\pi_{A'} \\ &\equiv \mathcal{A}^{A'}\pi_{A'}. \end{aligned}$$

Similar relations hold for the other dual twistors $\overline{B}_\beta Z^\beta \equiv \mathcal{B}^{B'}\pi_{B'}$, $\overline{C}_\gamma Z^\gamma \equiv \mathcal{C}^{C'}\pi_{C'}$, and $\overline{D}_\delta Z^\delta \equiv \mathcal{D}^{D'}\pi_{D'}$. We write the Penrose transform as an integral over the $\mathbb{CP}^1$ coordinate $\zeta = \pi_{1'}/\pi_{0'}$, so we use the measure previously given in Eqn. (7.18) as

$$\pi_{C'}d\pi^{C'} = (\pi_{0'})^2 d\zeta.$$

We adopt the canonical spin bases $\{o_{A'}, \iota_{A'}\}$ as in Eqn. (9.2) so that

$$\pi_{A'} = \pi_{0'}(o_{A'} + \zeta\iota_{A'}).$$

Recalling from Eqn. (7.19) that $\mathcal{A}_{A'}$ is defined implicitly by $\bar{A}_\alpha Z^\alpha = \mathcal{A}_{A'}\pi^{A'}$ we have

$$\frac{1}{\pi_{0'}}\mathcal{A}^{A'}\pi_{A'} = \mathcal{A}^{0'} + \mathcal{A}^{1'}\zeta$$

and similarly for $\mathcal{B}$, $\mathcal{C}$, and $\mathcal{D}$. Thus

$$\begin{aligned}
\varphi_{A'_1\cdots A'_{2h}}(x) &= \frac{1}{2\pi i}\oint_\Gamma f(Z)\pi_{A'_1}\cdots\pi_{A'_{2h}}\pi_{B'}d\pi^{B'} \qquad (10.3)\\
&= \frac{1}{2\pi i}\oint_\Gamma \frac{(\mathcal{C}^{0'}+\mathcal{C}^{1'}(\frac{\pi_{1'}}{\pi_{0'}}))^{h(n_p-1)}(\mathcal{D}^{0'}+\mathcal{D}^{1'}(\frac{\pi_{1'}}{\pi_{0'}}))^{h(n_t-1)}}{(\mathcal{A}^{0'}+\mathcal{A}^{1'}(\frac{\pi_{1'}}{\pi_{0'}}))(\mathcal{B}^{0'}+\mathcal{B}^{1'}(\frac{\pi_{1'}}{\pi_{0'}}))^{h(n_p+n_t)+1}}\\
&\qquad\qquad \times (o_{A_1}+(\frac{\pi_{1'}}{\pi_{0'}})\iota_{A'_1})\cdots(o_{A_{2h}}+(\frac{\pi_{1'}}{\pi_{0'}})\iota_{A'_{2h}})d(\frac{\pi_{1'}}{\pi_{0'}})\\
&= \frac{(\mathcal{C}^{1'})^{h(n_p-1)}(\mathcal{D}^{1'})^{h(n_t-1)}}{2\pi i\mathcal{A}^{1'}(\mathcal{B}^{1'})^{h(n_p+n_t)+1}}\oint_\Gamma \frac{(\rho+\zeta)^{h(n_p-1)}(\tau+\zeta)^{h(n_t-1)}}{(\mu+\zeta)(\nu+\zeta)^{h(n_p+n_t)+1}}\\
&\qquad\qquad \times (o_{A_1}+\zeta\iota_{A'_1})\cdots(o_{A_{2h}}+\zeta\iota_{A'_{2h}})d\zeta
\end{aligned}$$

where $\mu = \mathcal{A}^{0'}/\mathcal{A}^{1'}$, $\nu = \mathcal{B}^{0'}/\mathcal{B}^{1'}$, $\rho = \mathcal{C}^{0'}/\mathcal{C}^{1'}$, and $\tau = \mathcal{D}^{0'}/\mathcal{D}^{1'}$.

As before the contour Γ is taken to enclose the pole $-\mu$, and applying Cauchy's integral theorem gives

$$\begin{aligned}
\varphi_{A'_1\cdots A'_{2h}} &= \frac{(\mathcal{C}^{1'})^{h(n_p-1)}(\mathcal{D}^{1'})^{h(n_t-1)}}{\mathcal{A}^{1'}(\mathcal{B}^{1'})^{h(n_p+n_t)+1}}\operatorname*{Res}_{\zeta=-\mu}\frac{(\rho+\zeta)^{h(n_p-1)}(\tau+\zeta)^{h(n_t-1)}}{(\mu+\zeta)(\nu+\zeta)^{h(n_p+n_t)+1}}\\
&\qquad\qquad \times (o_{A_1}+\zeta\iota_{A'_1})\cdots(o_{A_{2h}}+\zeta\iota_{A'_{2h}})\\
&= \frac{(\mathcal{C}^{1'})^{h(n_p-1)}(\mathcal{D}^{1'})^{h(n_t-1)}}{\mathcal{A}^{1'}(\mathcal{B}^{1'})^{h(n_p+n_t)+1}}\frac{(\rho-\mu)^{h(n_p-1)}(\tau-\mu)^{h(n_t-1)}}{(\nu-\mu)^{h(n_p+n_t)+1}}\\
&\qquad\qquad \times (o_{A'_1}-\mu\iota_{A'_1})\cdots(o_{A'_{2h}}-\mu\iota_{A'_{2h}}).
\end{aligned}$$

After some algebra, we arrive at the result

$$\begin{aligned}\varphi_{A'_1\cdots A'_{2h}} &= \frac{(\mathcal{A}^{1'}\mathcal{C}^{0'} - \mathcal{A}^{0'}\mathcal{C}^{1'})^{h(n_p-1)}(\mathcal{A}^{1'}\mathcal{D}^{0'} - \mathcal{A}^{0'}\mathcal{D}^{1'})^{h(n_t-1)}}{(\mathcal{A}^{1'}\mathcal{B}^{0'} - \mathcal{A}^{0'}\mathcal{B}^{1'})^{h(n_p+n_t)+1}} \\ &\qquad \times (\mathcal{A}^{1'}o_{A'_1} - \mathcal{A}^{0'}\iota_{A'_1})\cdots(\mathcal{A}^{1'}o_{A'_{2h}} - \mathcal{A}^{0'}\iota_{A'_{2h}}) \\ &= \frac{(\epsilon_{C'D'}\mathcal{A}^{C'}\mathcal{C}^{D'})^{h(n_p-1)}(\epsilon_{E'F'}\mathcal{A}^{E'}\mathcal{D}^{F'})^{h(n_t-1)}}{(\epsilon_{A'B'}\mathcal{A}^{A'}\mathcal{B}^{B'})^{h(n_p+n_t)+1}}\mathcal{A}_{A'_1}\cdots\mathcal{A}_{A'_{2h}} \\ &= \frac{(\mathcal{A}_{C'}\mathcal{C}^{C'})^{h(n_p-1)}(\mathcal{A}_{D'}\mathcal{D}^{D'})^{h(n_t-1)}}{(\mathcal{A}_{B'}\mathcal{B}^{B'})^{h(n_p+n_t)+1}}\mathcal{A}_{A'_1}\cdots\mathcal{A}_{A'_{2h}}. \qquad (10.4)\end{aligned}$$

10.3 EM Torus Knots

Taking $h = 1$ in Eqn. (10.4), the resulting spinor field is

$$\phi_{A'B'}(x) = \frac{(\mathcal{A}_{C'}\mathcal{C}^{C'})^{n_p-1}(\mathcal{A}_{D'}\mathcal{D}^{D'})^{n_t-1}}{(\mathcal{A}_{E'}\mathcal{B}^{E'})^{n_p+n_t+1}}\mathcal{A}_{A'}\mathcal{A}_{B'}. \qquad (10.5)$$

The solution in Eqn. (10.5) satisfies the source-free spinor field equation by construction and yields the field strength spinor

$$\nabla^{AA'}\varphi_{A'B'} = 0,$$

$$F_{A'B'AB} = \varphi_{A'B'}\epsilon_{AB} + c.c.$$

The spin-1 fields are the null torus knots discussed in Section 2.6. With the choice for C and D given in Eqn. (10.2), the poloidal and toroidal winding numbers for the EM case are related to the exponents in Eqn. (7.14) by $c = n_p - 1$ and $d = n_t - 1$. The (1,1) case corresponds to the electromagnetic hopfion.

10.4 GEM Torus Knots

Taking $h = 2$ in Eqn. (10.4), the resulting spinor field is

$$\phi_{A'B'C'D'}(x) = \frac{(\mathcal{A}_{F'}\mathcal{C}^{F'})^{2(n_p-1)}(\mathcal{A}_{G'}\mathcal{D}^{G'})^{2(n_t-1)}}{(\mathcal{A}_{E'}\mathcal{B}^{E'})^{2(n_p+n_t)+1}}\mathcal{A}_{A'}\mathcal{A}_{B'}\mathcal{A}_{C'}\mathcal{A}_{D'}. \tag{10.6}$$

The source-free field equation and Weyl field strength spinor are

$$\nabla^{AA'}\varphi_{A'B'C'D'} = 0,$$

$$C_{A'B'C'D'ABCD} = \varphi_{A'B'C'D'}\epsilon_{AB}\epsilon_{CD} + c.c.$$

The Weyl tensor can then be decomposed into the GEM components. For Type N, the eigenvalues for both the gravito-electric and gravito-magnetic tensors take the form $\{-\Lambda(x), 0, +\Lambda(x)\}$. The magnitude of the eigenvalues is

$$|\Lambda(x)| = \frac{(1+r^2+t^2-2tz)^2(r^2-z^2)^{n_p-1}(r^4-2r^2(1+t^2)+(1+t^2)^2+4z^2)^{n_t-1}}{2^{3-2n_p}(r^4-2r^2(-1+t^2)+(1+t^2)^2)^{\frac{5}{2}+n_t+n_p}}. \tag{10.7}$$

We label the eigenvectors $\{\vec{e}_-, \vec{e}_0, \vec{e}_+\}$ and $\{\vec{b}_-, \vec{b}_0, \vec{b}_+\}$ corresponding to the eigenvalues for the tidal and frame-drag fields respectively. For the zero eigenvalue fields, the eigenvectors $\vec{e}_0$ and $\vec{b}_0$ are both aligned with the Poynting vector of the null EM torus knots. For the remaining eigenvectors, we can construct Riemann-Silberstein (RS) vectors $\vec{f_e} = \vec{e}_- + i\vec{e}_+$ and $\vec{f_b} = \vec{b}_- + i\vec{b}_+$ which are related to each other by

$$\vec{f_e} = e^{i\pi/4}\vec{f_b}. \tag{10.8}$$

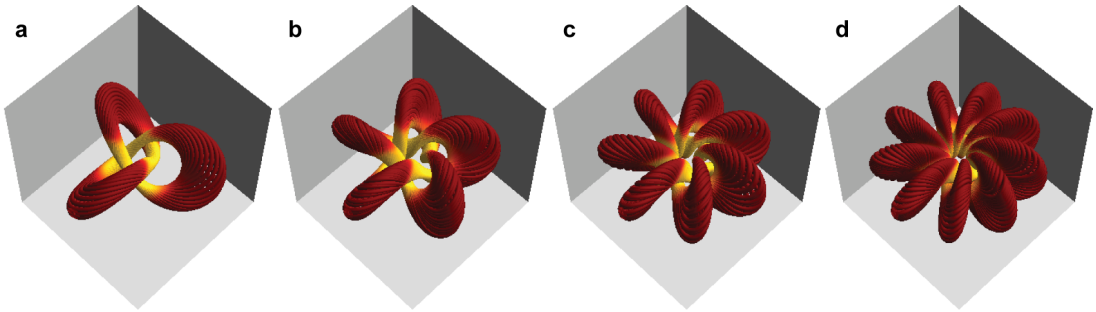

Figure 10.1: The eigenvector field $\vec{e}_-$ for the gravitational field based on the **a** trefoil (2,3) knot, **b** cinquefoil (2,5) knot, **c** septafoil (2,7) knot, and **d** nonafoil (2,9) knot. The color scaling is the same as in Figure 10.2.

At $t = 0$, the eigenvectors of the GE fields have precisely the same structure as the EM fields, and the GM eigenvector fields have the same structure but rotated by 45°. For the spin-2 case, the poloidal and toroidal winding numbers are related to the exponents in Eqn. (7.14) by $c = 2(n_p - 1)$ and $d = 2(n_t - 1)$. The surfaces of the $\vec{e}_-$ eigenvector, color-scaled according to the magnitude of the eigenvalue, for different values of (n_t, n_p) are shown in Figure 10.1. The other GEM fields can be constructed by rotating $\vec{e}_-$ according to Eqn. (10.8). The $\vec{e}_+$ vector field is found by rotating $\vec{e}_-$ by 90° about the Poynting vector. The $\vec{b}_-$ and $\vec{b}_+$ fields are found by rotating $\vec{e}_-$ and $\vec{e}_+$ by 45°, respectively. The eigenvalues of the GEM fields for a given (n_t, n_p) have the same magnitude (color-scaling) given by $|\Lambda(x)|$ in Eqn. (10.7). The complete configuration for the GEM $(2, 3)$ trefoil knot is given in Figure 10.2, with the EM trefoil knot also shown for comparison.

10.5 Summary

Here we have shown that the null EM torus knot solutions correspond to a class of elementary states characterized the poloidal and toroidal winding numbers of the associated field configuration. Using the relationship between fields of different spin in the twistor formalism, we constructed the analogous gravitational radiation configurations that possess tendex and vortex lines based on a torus knot structure. Since the topology is manifest in the tendex and vortex lines, the gravito-electromagnetic tidal tensor decomposition is a straightforward method for characterizing these field configurations.

The elementary states were known as early as the 1970's [22], however the explicit forms of their associated spinor and tensor representations on $\mathbb{M}$ were never published.[3] The modern rediscovery of these solutions has raised interest in obtaining a more complete physical understanding of the topological properties of these fields. The parameterization of the twistor functions corresponding to the elementary states in terms of the poloidal and toroidal winding indicates that the torus knot structure is indeed inherent in the elementary states. For both electromagnetism and gravity, the topology appears in the configuration of the lines of force.

[3] from private discussions with Roger Penrose

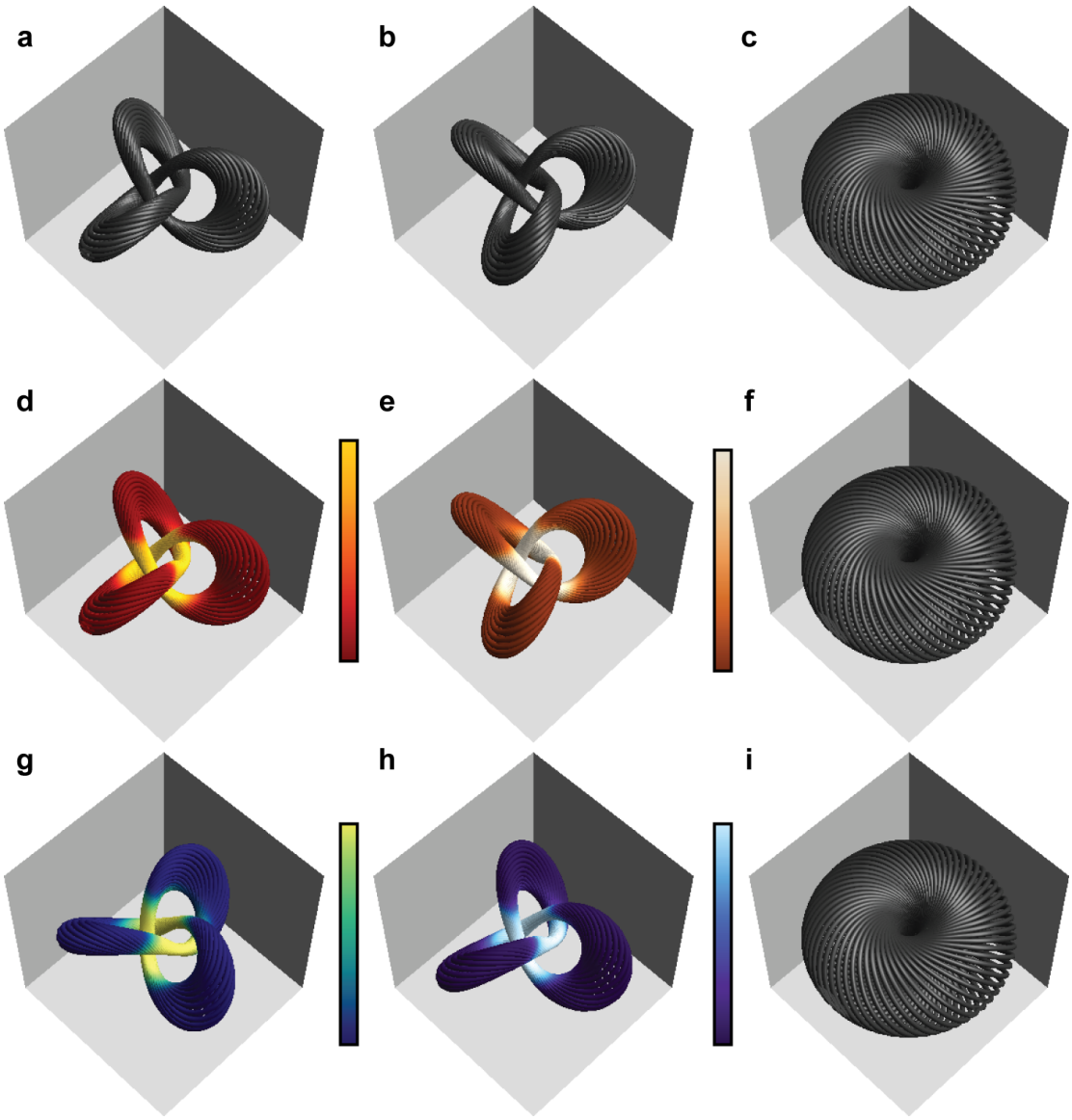

Figure 10.2: A comparison of the spin-1 (EM) and spin-2 (gravity) trefoil knots at $t = 0$. The first row is the EM trefoil knot: **a** the electric field, **b** the magnetic field, and **c** the Poynting vector field. The second row is the gravito-electric trefoil knot: **d** the negative eigenvalue field $\vec{e}_-$, **e** the positive eigenvalue field $\vec{e}_+$, and **f** the zero eigenvalue field $\vec{e}_0$.The third row is the gravito-magnetic trefoil knot: **g** the negative eigenvalue field $\vec{b}_-$, **h** the positive eigenvalue field $\vec{b}_+$, and **i** the zero eigenvalue field $\vec{b}_0$. The color scale indicates magnitude of the eigenvalue, with lighter colors indicating a higher magnitude.

Chapter 11

Generalization of Electromagnetic and Gravitational Hopfions by Algebraic Type

An alternative definition for *hopfion* is a field configuration whose principal null directions (PNDs) all lie tangent to Robinson congruences. As discussed in Chapter 5, given a real-valued spin-h field $\varphi_{A'_{A_1}\ldots A'_{A_{2h}}}$ written in the self-dual $SL(2,\mathbb{C})$ spinor representation, the field can be decomposed into $2h$ single-index spinors called its principal spinors [39]. This is described by the relation

$$\varphi_{A'_{A_1}\ldots A'_{A_{2h}}} \propto \alpha_{(A'_1}\cdots\gamma_{A'_{2h})}, \tag{11.1}$$

with the one-index spinors representing the field's PNDs via their flagpole directions. Thus, for a hopfion arising from the definition given above, the PNDs of the spinors $\alpha,\ldots,\gamma$ lie tangent to Robinson congruences.

In Chapter 9, we used twistor integral methods to extend the EM solutions to find an analogous topologically non-trivial Type N gravitational wave solutions.

Now we will discuss how these methods can be used to find the analogous solutions of the different spinor classifications. In particular, we will construct the non-null electromagnetic, Type D and Type III gravitational hopfion solutions, and then characterize the topology of their lines of force.

11.1 Twistor Methods for Spin-h Hopfions

We saw before that a null spin-1 field can be written as

$$\varphi_{A'B'}(x) = f(x)\mathcal{A}_{A'}\mathcal{A}_{B'} \tag{11.2}$$

where $\mathcal{A}_{A'}$ is an $SL(2,\mathbb{C})$ spinor which defines the doubly degenerate principle null direction of F_{ab} and $f(x)$ is a scalar function that is determined by the electromagnetic field equation.

This suggests for any helicity h there is an analogous spinor field

$$\varphi_{A'_1\cdots A'_{2h}}(x) = f_h(x)\mathcal{A}_{A'_1}\cdots\mathcal{A}_{A'_{2h}} \tag{11.3}$$

with $2h$-fold degenerate PNDs, but we will need to find the scaling function $f_h(x)$ that satisfies the appropriate spin-h field equation.

The twistor formalism allows for the generalization of spin-1 fields to fields of any spin. The Penrose transform expresses solutions to the massless field equations as contour integrals over homogeneous twistor functions $F(Z)$. Thus, generating fields using twistor integral methods ensures that the result is indeed a solution

to the field equations on space-time. We will also see that because of the contour integral the poles of $F(Z)$ play a physical role in the corresponding field geometry.

The twistor function which gives way to the EM hopfion through the Penrose transform is given by

$$F_1(Z) = \frac{1}{(A_\alpha Z^\alpha)(B_\beta Z^\beta)^3}. \tag{11.4}$$

Consider the pole structure of Eqn. (11.4). The term $(A \cdot Z)$ has a simple pole and the power of the $(B \cdot Z)$ term is chosen to give us homogeneity -4, and thus a spin-1 field.

The spin-h analogue follows immediately. We keep the single pole for the $(A \cdot Z)$ term and the power of the $(B \cdot Z)$ term is determined by the relation between helicity and homogeneity given in Eqn. (7.10). The generating function for the spin-h hopfion is then

$$F_h(Z) = \frac{1}{(A_\alpha Z^\alpha)(B_\beta Z^\beta)^{2h+1}}. \tag{11.5}$$

We found before that the associated spinor field from the Penrose transform of this twistor function is

$$\varphi_{A'_1 \cdots A'_{2h}}(x) = \left(\frac{2}{\Omega |x-y|^2}\right)^{2h+1} \mathcal{A}_{A'_1} \cdots \mathcal{A}_{A'_{2h}} \tag{11.6}$$

where Ω is a constant scalar, y is a constant 4-vector determined by the specific values of A_α and B_β, and $\mathcal{A}_{A'}$ is the spinor field associated to the twistor A_α. As expected, we find the solution has a $2h$-fold degeneracy in its PNDs and the

Penrose transform has given us the correct form of the scalar function that will satisfy the field equations.

11.1.1 Petrov Variants

The twistor function in Eqn. (11.5) had a single pole which resulted in a spinor field with all its PNDs degenerate (null EM or Type N gravity fields). Changing the pole structure yields different Petrov classes. Because the Penrose transform is a contour integral, when transforming functions with a pole of order greater than one Cauchy's integral formula involves the derivative of $F(Z)$. This derivative brings the other spinor field, in this case $\mathcal{B}_{B'}$, into the numerator thus breaking the degeneracy of the PNDs. For example,

$$F_h(Z) = \frac{1}{(A_\alpha Z^\alpha)^{h+1}(B_\beta Z^\beta)^{h+1}}. \tag{11.7}$$

results in non-null EM $\{11\}$ or Type D gravity $\{22\}$ fields for $h = 1, 2$.

$$\varphi_{A'_1 A'_2}(x) = f_1(x)\mathcal{A}_{(A'_1}\mathcal{B}_{A'_2)} \tag{11.8}$$

$$\varphi_{A'_1 A'_2 A'_3 A'_4}(x) = f_2(x)\mathcal{A}_{(A'_1}\mathcal{A}_{A'_2}\mathcal{B}_{A'_3}\mathcal{B}_{A'_4)} \tag{11.9}$$

where $\mathcal{A}_{A'}$ and $\mathcal{B}_{A'}$ define the h-fold degenerate principle null directions.

This gives all the classifications of the EM field strength tensor, which has two PNDs. For gravity we can also extend this to other classifications for which there

is no EM analog, for example the Type III Petrov class generated by

$$F_{2,III}(Z) = \frac{1}{(A_\alpha Z^\alpha)^2 (B_\beta Z^\beta)^4} \tag{11.10}$$

and resulting in

$$\varphi_{A'_1 \cdots A'_4, III}(x) = \left(\frac{2}{\Omega |x-y|^2} \right)^{2h+1} \mathcal{A}_{(A'_1} \mathcal{A}_{A'_h} \mathcal{A}_{A'_3} \mathcal{B}_{B'_4)}. \tag{11.11}$$

The simplest hopfions correspond to homogeneous twistor functions of the form

$$F(Z) = \frac{1}{(A \cdot Z)^a (B \cdot Z)^b}. \tag{11.12}$$

The general result is

$$\varphi_{A'_1 \ldots A'_{2h}} = \left(\frac{2}{\Omega |x-y|^2} \right)^{a+b+1} \mathcal{A}_{(A'_1} \cdots \mathcal{A}_{A'_b} \mathcal{B}_{A'_{b+1}} \cdots \mathcal{B}_{A'_{2h})}. \tag{11.13}$$

Thus the hopfions of different algebraic type are characterized by two quantities a and b, with $a + b = 2h + 2$.

We now see that the null EM and Type N gravitational hopfions which we studied in Chapter 9 are elementary hopfions with $a = 1$. In fact all null hopfions take this form, which is obvious from the expression in Eqn. (11.13) where, in the case $a = 1$, the PNDs are all proportional to the flagpole of $\mathcal{A}_{A'}$ and thus completely degenerate. Before we consider the gravitational hopfions, we give a brief overview of the electromagnetic hopfions.

11.2 EM Hopfions

The electromagnetic hopfions are spin-1, and thus have two distinct classifications: fields with two degenerate PNDs (null) and fields with two distinct PNDs (non-null).

11.2.1 Null EM Hopfion

The null EM hopfion $\varphi_{A'B'} \sim \mathcal{A}_{A'}\mathcal{A}_{B'}$ is the simplest example of a hopfion. Previously, we used the twistor construction to generate exactly the solution constructed by Rañada, which propagated in the $-\hat{y}$-direction. It will simplify the solution if we make a new choice of the dual twistors A_α and B_β so that the solution propagates in the $+\hat{z}$-direction. Taking the dual twistors as Robinson congruences oriented in the $+z$ and $-z$ directions

$$A_\alpha = (0, \sqrt{2}, 0, 1), \quad B_\alpha = (\sqrt{2}, 0, 1, 0), \tag{11.14}$$

produces a solution with the same structure as studied previously in Chapter 9, just with a different orientation. The same choice of A_α and B_β will be used in conjunction with Eqn. (11.13) to construct the hopfion fields of different algebraic type.

The Riemann-Silberstein vector is now

$$\vec{F}_{null} = \vec{E}_R + i\vec{B}_R \tag{11.15}$$

$$= \frac{4}{\pi(-(t-i)^2+r^2)^3}\begin{pmatrix} (x-iz)^2-(t-i+y)^2 \\ 2(x-iz)(t-i+y) \\ i(x-iz)^2+i(t-i+y)^2 \end{pmatrix}. \tag{11.16}$$

The energy density u and Poynting vector $\vec{S}$ for this field are given by

$$u_{null} = \frac{(1+x^2+y^2+(t-z)^2)^2}{(1+2(t^2+r^2)+(t^2-r^2)^2)^3}, \tag{11.17}$$

$$\vec{S}_{null} = \frac{u_{null}}{(1+x^2+y^2+(t-z)^2)}\begin{pmatrix} 2(x(t-z)+y) \\ 2(y(t-z)-x) \\ x^2+y^2-(t-z)^2-1 \end{pmatrix}. \tag{11.18}$$

We will use these properties to analyze the new solutions in terms of the structure of the null EM hopfion.

11.2.2 Non-null EM Hopfion

The non-null EM hopfion $\varphi_{A'B'} \sim \mathcal{A}_{(A'}\mathcal{B}_{B')}$ can also be neatly expressed by an RS vector,

$$\vec{F}_{non-null} = \frac{2}{(-(t-i)^2+r^2)^3}\begin{pmatrix} -2(xz-iy(t-i)) \\ -2(yz+ix(t-i)) \\ (t-i)^2+x^2+y^2-z^2 \end{pmatrix}. \tag{11.19}$$

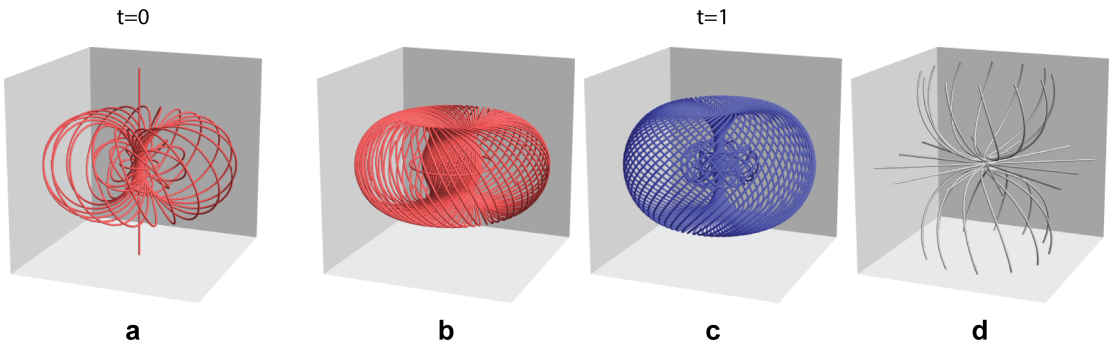

Figure 11.1: The field line structure of the non-null EM hopfion. (**a**) The electric field lines at $t = 0$ have the structure of the Hopf fibration. Not shown are $\vec{B}$ and $\vec{S}$, which are both identically zero at $t = 0$. For $t = 1$,(**b**) the electric field (**c**) the magnetic field, and (**d**) the Poynting vector.

At $t = 0$ the $\vec{E}$ field for this hopfion is everywhere tangent to a Robinson congruence, while $\vec{B}$ and hence $\vec{S}$ are identically zero since the RS vector is purely real. For $t \neq 0$, $\vec{B} \neq 0$ and the field line topologies for $\vec{E}$ and $\vec{B}$ are not preserved since $\vec{E} \cdot \vec{B} \neq 0$, however the field lines do still lie on tori. The field line structure of $\vec{S}$ shows that the solution does not propagate, but rather energy flows outward from the center of the configuration. These results are collected in Figure 11.1.

The non-null EM hopfion has the following expressions for the energy density and Poynting vector

$$u_{non-null} = \frac{2(t^4 + 2t^2(1 + 3r^2 - 4z^2) + (1 + r^2)^2)}{(1 + 2(t^2 + r^2) + (t^2 - r^2)^2)^3}, \tag{11.20}$$

$$\vec{S}_{\substack{non- \\ null}} = \frac{2tu_{non-null}}{(t^4 + 2t^2(1 + 3r^2 - 4z^2) + (1 + r^2)^2)} \begin{pmatrix} x^3 + 2yz + x(1 + t^2 + y^2 - z^2) \\ y^3 - 2xz + y(1 + t^2 + x^2 - z^2) \\ 2z(x^2 + y^2) \end{pmatrix}. \tag{11.21}$$

We will see in the next section that these are related to the analogous gravitational hopfion fields.

11.3 GEM Hopfions

The gravitational hopfions are characterized by $h = 2$, so there are a total of five distinct non-trivial gravitational hopfions, given by the Petrov Types N, D, III, II, and I which classify the degeneracies of the PNDs. Here we review the Type N, then present the Type D and Type III hopfions and analyze their structure using the GEM formalism.

11.3.1 Type N GEM Hopfion

The Type N gravitational hopfion, previously studied in Chapter 9, has the form $\varphi_{A'B'C'D'} \sim \mathcal{A}_{A'}\mathcal{A}_{B'}\mathcal{A}_{C'}\mathcal{A}_{D'}$ and provides a good starting point for discussing the use of GEM in studying hopfions. The Weyl decomposition for the Type N and Type III hopfions has eigenvalues for both GEM fields that take the form $\{\lambda_-, \lambda_0, \lambda_+\}$, with $\lambda_-(x) \leq \lambda_0(x) \leq \lambda_+(x)$ for all points x in space-time Thus,

we may label the eigenvectors $\{\vec{e}_-, \vec{e}_0, \vec{e}_+\}$ and $\{\vec{b}_-, \vec{b}_0, \vec{b}_+\}$ corresponding to the eigenvalues for the tidal and frame-drag fields respectively. For Type N fields, the eigenvalues take the very simple form $\{-\Lambda, 0, \Lambda\}$ with $\Lambda(x)$ a function on space-time.

For the Type N hopfion, the eigenvectors $\vec{e}_0$ and $\vec{b}_0$ are both equivalent to the Poynting vector in Eqn. (11.18) for the null EM hopfion, up to an overall scalar. For the remaining eigenvectors, we can construct RS vectors $\vec{f_e} = \vec{e}_- + i\vec{e}_+$ and $\vec{f_b} = \vec{b}_- + i\vec{b}_+$ which are related to the RS vector $\vec{F}$ for the null EM hopfion from Eqn. (11.15) via

$$\vec{f_e} = e^{i\pi/4}\vec{f_b} = e^{i\,\mathrm{Arg}\,\theta}\vec{F}, \qquad \theta(x) = \sqrt{-(t-i)^2 + r^2}. \tag{11.22}$$

The super-energy and super-Poynting vector for this field and their relationship with the duality invariants of the null EM hopfion, as well as a discussion of the tendex and vortex lines, are discussed in more detail in Chapter 9.

11.3.2 Type D GEM Hopfion

The Type D gravitational hopfion $\varphi_{A'B'C'D'} \sim \mathcal{A}_{(A'}\mathcal{A}_{B'}\mathcal{B}_{C'}\mathcal{B}_{D')}$ is the gravitational analog of the non-null EM hopfion, in that its PNDs are split evenly into two sets. For spin-2, the two sets consist of pairs of doubly degenerate PNDs. This hopfion has eigenvalue structure $\{2\Lambda, -\Lambda + \lambda, -\Lambda - \lambda\}$, where $\lambda = 0$ at $t = 0$ simplifying the eigenvalue structure to $\{2\Lambda, -\Lambda, -\Lambda\}$. Note also that $\Lambda(x)$

used here represents a different function than the $\Lambda(x)$ used before to describe the Type N hopfion; we use the symbol only to describe the overall structure of the eigenvalues. This eigenvalue structure is interesting because at $t = 0$ the eigenvalues $-\Lambda \pm \lambda$ coincide, so their eigenvectors collapse into a doubly degenerate eigenspace. Furthermore, at $t = 0$, the GE field $\vec{e}_{2\Lambda}$ is exactly tangent to a Hopf fibration and the frame-drag field vanishes, hence the GM eigenvalues and eigenvectors vanish as well. The values of Λ and λ are rather complicated, so we will not present them here. The tendex and vortex lines have been plotted numerically in Figure 11.2.

The expressions for the super-energy and super-Poynting vector of the Type D hopfion are quite long, but they take a simpler form when written in terms of the duality invariants of the non-null EM hopfion

$$U = \frac{t^8 + 8t^4(1 + 4x^2 + 4y^2) + (t^6 + t^2(1 + r^2)^2)(5 + 11r^2 - 12z^2) + (1 + r^2)^4}{12(1 + 2(t^2 + r^2) + (t^2 - r^2)^2)^5} + \frac{\frac{1}{2}t^2(-1 + 9r^2 - 12z^2)}{12(1 + 2(t^2 + r^2) + (t^2 - r^2)^2)^2} u_{non-null}, \tag{11.23}$$

$$\vec{P}_D = \frac{1}{32}(1 + 2(t^2 + r^2) + (t^2 - r^2)^2) u_{non-null} \vec{S}_{non-null}. \tag{11.24}$$

Similarly to the non-null EM case, the super-Poynting vector indicates that the field configuration radiates energy outward from the center in all directions, but the overall structure does not propagate.

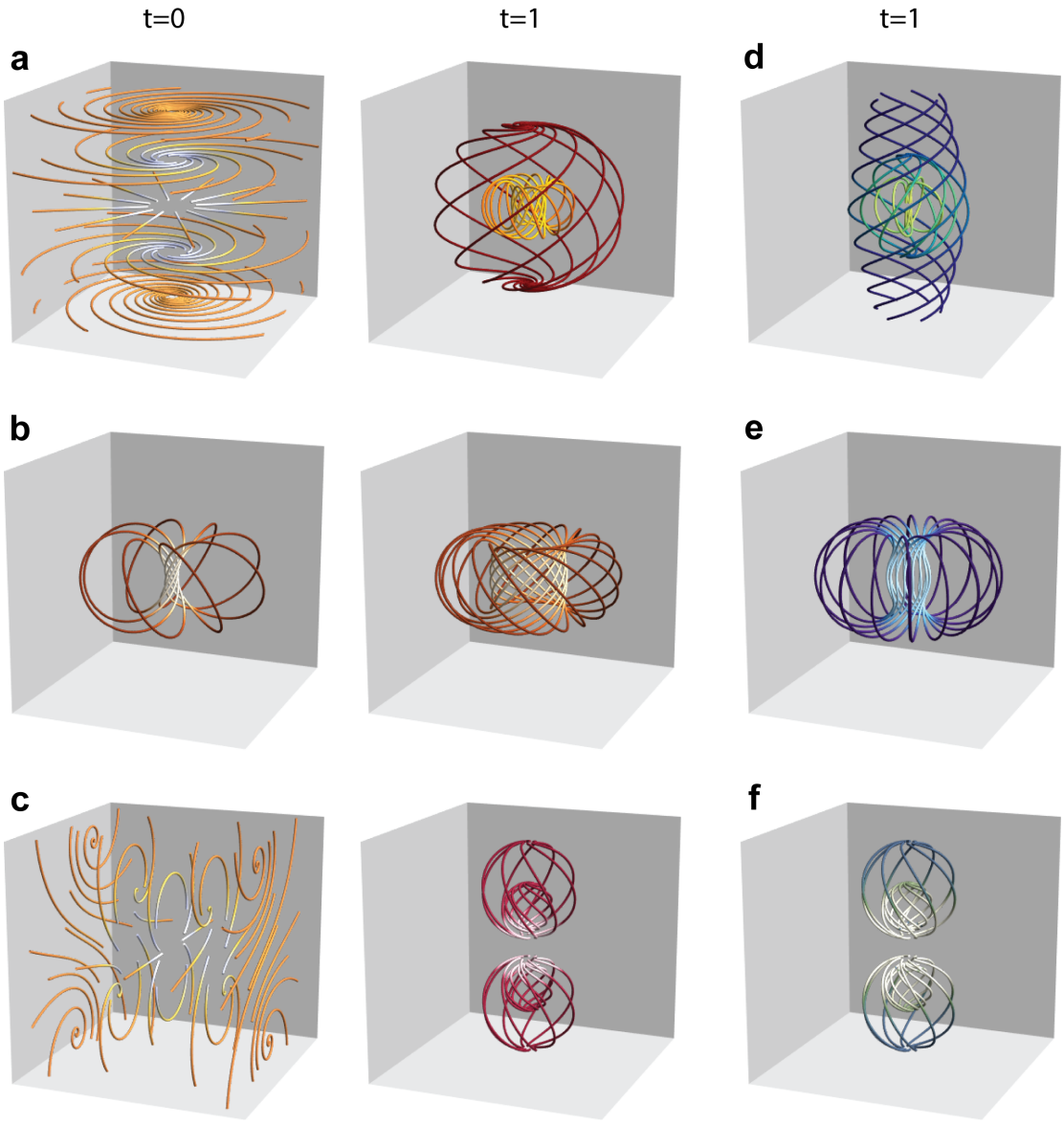

Figure 11.2: The Type D gravitational hopfion at $t = 0$ and $t = 1$: the tidal fields (**a**) $e_{-\Lambda+\lambda}$, (**b**) $e_{2\Lambda}$, and (**c**) $e_{-\Lambda-\lambda}$; and the frame-drag fields (**d**) $b_{-\Lambda+\lambda}$, (**e**) $b_{2\Lambda}$, and (**f**) $b_{-\Lambda-\lambda}$. The frame-drag fields at $t = 0$ are omitted because they are all vanishing then. As before the field lines are colored by the relative magnitude of their eigenvalues, with lighter colors indicating greater magnitude. The fields at $t = 0$ in (**a**) and (**c**) are presented with the same color scheme to convey the fact that they really represent a degenerate eigenspace together.

11.3.3 Type III GEM Hopfion

The Type III gravitational hopfion $\varphi_{A'B'C'D'} \sim \mathcal{A}_{(A'}\mathcal{A}_{B'}\mathcal{A}_{C'}\mathcal{B}_{D')}$ has one set of triply degenerate PNDs and one unique PND. This hopfion has eigenvalue structure $\{\lambda_-, \lambda_0, \lambda_+\} = \{-\Lambda, \lambda, \Lambda - \lambda\}$, where $\lambda = 0$ at $t = 0$. We again note that the functions $\Lambda(x)$ and $\lambda(x)$ used here represent different functions than those used to describe the Type N and Type D hopfions. The tendex and vortex lines have been plotted numerically in Figure 11.3. At $t = 0$, both the GE and GM fields are tangent to three orthogonal Hopf fibrations, but with different orientations than the Type N case. For Type III, the eigenvectors $\vec{e}_0$ and $\vec{b}_0$ are not aligned with the super-Poynting vector, but rather are orthogonal to it (and each other).

For the Type III hopfion, the super-energy density and the super-Poynting vector are given by

$$U_{III} = \frac{(1 + x^2 + y^2 + (t - z)^2)^2(t^4 + 2t^2(1 + 7r^2 - 8z^2) + (1 + r^2)^2)}{8(1 + 2(t^2 + r^2) + (t^2 - r^2)^2)^5}, \quad (11.25)$$

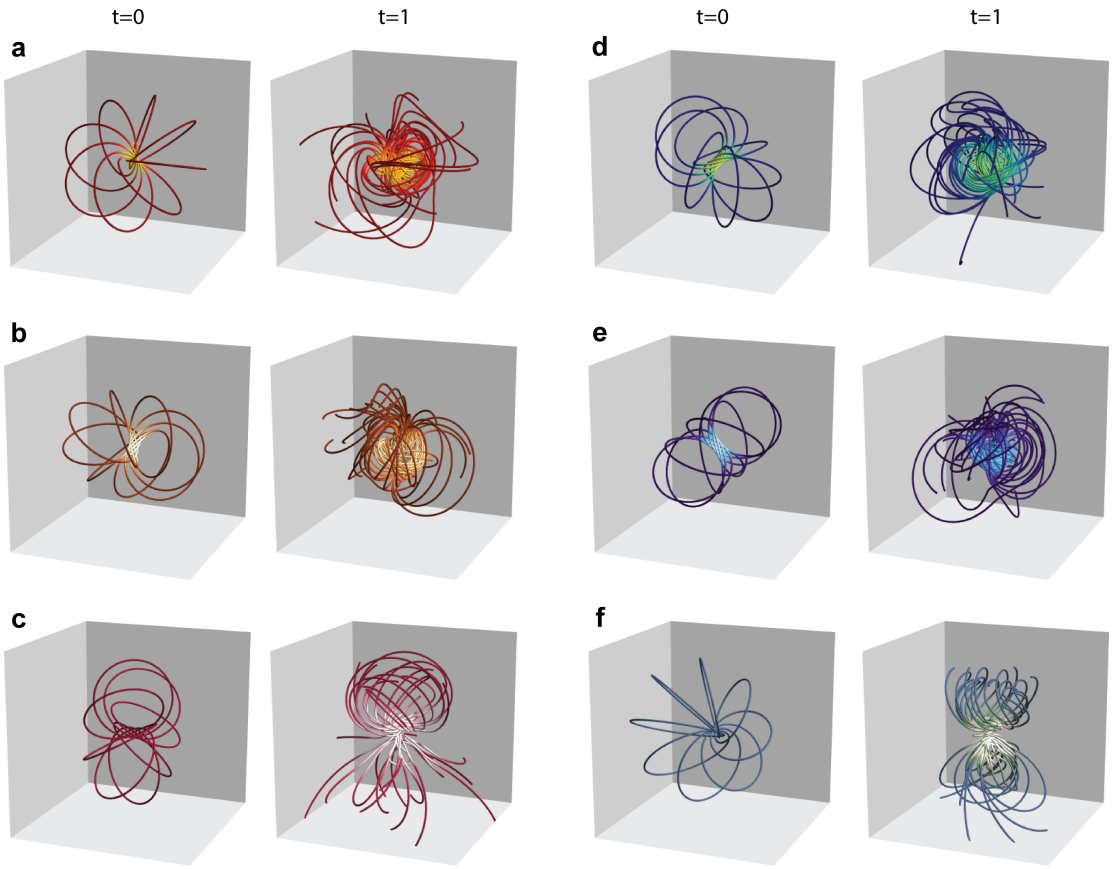

Figure 11.3: The Type III gravitational hopfion at $t = 0$ and $t = 1$: the tidal fields (**a**) e_-, (**b**) e_+, and (**c**) e_0; and the frame-drag fields (**d**) b_-, (**e**) b_+, and (**f**) b_0. The field lines are colored by the relative magnitude of their eigenvalues, with lighter colors indicating greater magnitude.

$$\vec{S}_{III} = \frac{U_{III}}{2(1+x^2+y^2+(t-z)^2)} \begin{pmatrix} 2(x(t-z)+y) \\ 2(y(t-z)-x) \\ -1+x^2+y^2-(t-z)^2 \end{pmatrix} \tag{11.26}$$

$$+ \frac{4tU_{III}}{t^4+2t^2(1+7r^2-8z^2)+(1+r^2)^2} \begin{pmatrix} x^3+2yz+x(1+t^2+y^2-z^2) \\ y^3-2xz+y(1+t^2+x^2-z^2) \\ 2z(x^2+y^2) \end{pmatrix}.$$

Comparing with the energy density and Poynting vector of the EM hopfions, we see that the two sets of local duality invariants are similar. The super-energy is related by

$$U_{III} = \frac{(t^4 + 2t^2(1 + 7r^2 - 8z^2) + (1 + r^2)^2)}{8(1 + 2(t^2 + r^2) + (t^2 - r^2)^2)^2} u_{null}. \tag{11.27}$$

The two vector terms seen here in the super-Poynting vector are the same as the vector terms in the Poynting vectors $\vec{S}_{null}$ and $\vec{S}_{non-null}$ of the EM fields, from Eqns. (11.18) and (11.21) respectively, up to the overall scalar factors

$$\vec{P}_{III} = \frac{U_{III}}{2u_{null}} \vec{S}_{null} + \frac{U_N}{8u_{null}} \vec{S}_{non-null}. \tag{11.28}$$

11.3.4 Type II and Type I Fields

Finally, we briefly mention the Type II and Type I fields. It is not possible to generate algebraically special fields of these types from an elementary state. Type II fields contain three distinct PNDs, therefore one must introduce the $(C \cdot Z)$ term from Eqn. (10.1), where the twistor C_γ has the associated spinor field $\mathcal{C}_{A'}$ which becomes one PND. However, when you apply Cauchy's integral theorem to the contour integral the derivative requires you use the product rule, thus the result includes multiple terms. The solution is then a linear combination of different Type II fields. A similar situation arises for Type I.

11.4 Summary

The beauty of the Penrose transform lies in its complex contour integral nature, which allows for the application of Cauchy's theorem to bring out the spinor structure of solutions in $\mathbb{M}$. Thus, the pole structure of the twistor generating functions encodes the geometry of the resulting physical fields. By understanding this relationship, we used the twistor functions corresponding to the null EM and Type N GEM hopfions to generate a class of spin-h fields, including the non-null electromagnetic, Type D and Type III gravitational hopfions. We characterized the tendex and vortex structure of the gravitational hopfions using the gravito-electromagnetic formalism, and showed that the linked configuration of the Hopf fibration appears in the lines of force.

Chapter 12

Conclusion

> *You are the first person in whom the idea of bodies acting at a distance has arisen, as a principle to actually be believed in... You seem to see the lines of force curving around obstacles and driving plumb at conductors and swerving towards certain directions in crystals, and carrying with them everywhere the same amount of attractive power spread wider or denser as the as the lines widen or contract.*
>
> *You have also seen that the great mystery is... how like bodies attract (by gravitation). But if you can get over that difficulty... then your lines of force can "weave a web across the sky" and lead the stars in their courses...*
>
> James Clerk Maxwell, *in a letter to Faraday* (1857)

Since the earliest days of electromagnetism, when Gauss introduced his integral for calculating the linking number of two curves, the topology of physical fields has been of interest. The concept of field lines was developed by Faraday to give a direct, physical description of electromagnetic phenomena. He had also hoped to find a similar description for gravitational lines of force. Although he and other scientists such as Maxwell gave much thought to finding this analogy connecting electromagnetism and gravity, they were never able to give an adequate explanation or mathematical formulation for this relationship.

In modern times, the relationship between massless linear relativistic fields of different spin has been understood in terms of the $SL(2,\mathbb{C})$ spinor field equations. In this language, the spin-N equations - the Dirac, Maxwell, Rarita-Schwinger, and linear Einstein equations - take on a similar form. Their solutions can be expressed in terms of complex contour integrals allowing one to construct analogous fields based on topologically non-trivial configurations for any spin.

The concept of field lines can be applied to gravity, as was once hoped by Faraday and Maxwell, by decomposing the spin-1 and spin-2 solutions into the forces experienced by a particular time-like observer to find the lines of force. This gravito-electromagnetic tidal tensor analogy provides a direct way of analyzing the hopfion fields and their generalizations based on torus knots, where the topology physically manifests in the lines of force for both electromagnetism and gravity.

As we have seen, topology is also related to the dynamics of physical systems. For null electromagnetic fields and ideal MHD the linking number of the field lines is conserved, so the topology is preserved under time evolution. The radiative fields maintain their linked structure while propagating at the speed of light. Linked and knotted magnetic field configurations in plasma are stabilized by the magnetic helicity, which is associated to a conserved topological number, and thus these stationary solutions are exact solitons in ideal MHD. In full resistive MHD, simulations show that these solitons decay but the lifetime is extended due to the linking of the field lines. Whether a similar conservation law holds for Type N

gravitational fields is not known, but the gravito-electromagnetic analogy with null electromagnetic fields may provide an avenue for investigating how topology affects the dynamics of gravitational fields.

The fields based on the Hopf fibration and torus knots studied here represent some of the simplest topological structures found in continuous, space-filling configurations. The methods presented in this thesis could potentially be extended to the construction of classical electromagnetic and gravitational fields based on more intricate topologies. For example, the twist knots are the simplest class of knots after the torus knots [100], and have been observed in some areas of physics such as polymer materials [101, 102], DNA organization [103, 104], and quantum field theory [105, 106]. Identifying new field configurations and studying their properties could open new physical applications. Deepening our understanding of field line topology gives us insight into the structure and dynamics of physical systems, for indeed, it is these lines of force that determine our paths through the universe.

Bibliography

[1] J. H. Przytycki. Knots: From combinatorics of knot diagrams to combinatorial topology based on knots. 2007, arXiv:math/0703096.

[2] C. Nayak, S. H. Simon, A. Stern, M. Freedman, and S. Das Sarma. Non-abelian anyons and topological quantum computation. *Reviews of Modern Physics*, 80(3):1083–1159, 2008.

[3] T. H. R. Skyrme. A unified field theory of mesons and baryons. *Nuclear Physics*, 31(1):556–569, 1962.

[4] L. Faddeev and Antti J. Niemi. Stable knot-like structures in classical field theory. *Nature*, 387(6628):58–61, 1997.

[5] A. M. Kamchatnov. Topological solitons in magnetohydrodynamics. *Sov. Phys. JETP*, 55(1):69–73, 1982.

[6] Amy Thompson, Joe Swearngin, Alexander Wickes, and Dirk Bouwmeester. Constructing a class of topological solitons in magnetohydrodynamics. *Physical Review E*, 89(4):043104, 2014.

[7] Antonio F. Rañada and José L. Trueba. Topological electromagnetism with hidden nonlinearity. *Modern Nonlinear Optics, Part III*, 119:197–253, 2002.

[8] William T. M. Irvine and Dirk Bouwmeester. Linked and knotted beams of light. *Nature Physics*, 4(9):716–720, 2008.

[9] Jan Willem Dalhuisen and Dirk Bouwmeester. Twistors and electromagnetic knots. *Journal of Physics A: Mathematical and Theoretical*, 45(13):135201, 2012.

[10] Joe Swearngin, Amy Thompson, Alexander Wickes, Jan Willem Dalhuisen, and Dirk Bouwmeester. Gravitational hopfions. 2014, arXiv:gr-qc/1302.1431.

[11] Amy Thompson, Joe Swearngin, and Dirk Bouwmeester. Linked and knotted gravitational radiation. *Journal of Physics A: Mathematical and Theoretical*, 47(35):355205, 2014.

[12] Edward Witten. Quantum field theory and the Jones polynomial. *Communications in Mathematical Physics*, 121(3):351–399, 1989.

[13] G. D. Robertson. Torus knots are rigid string instantons. *Physics Letters B*, 226(3-4):244250, 1989.

[14] Javier Arsuaga, Mariel Vazquez, Paul McGuirk, Sonia Trigueros, De Witt Sumners, and Joaquim Roca. DNA knots reveal a chiral organization of DNA in phage capsids. *Proceedings of the National Acadamy of Sciences*, 102(26):91659169, 2005.

[15] T. Machon and G. Alexander. Knots and nonorientable surfaces in chiral nematics. *Proceedings of the National Acadamy of Sciences*, 110(35):1417414179, 2013.

[16] G. E. Volovik and V. P. Mineev. Particle-like solitons in superfluid He phases. *Sov. Phys. JETP*, 46(2):401–404, 1977.

[17] Yuki Kawaguchi, Muneto Nitta, and Masahito Ueda. Knots in a spinor Bose-Einstein condensate. *Physical Review Letters*, 100(18):180403, 2008.

[18] Antonio F. Rañada. A topological theory of the electromagnetic field. *Letters in Mathematical Physics*, 18(2):97–106, 1989.

[19] Hridesh Kedia, Iwo Bialynicki-Birula, Daniel Peralta-Salas, and William M. T. Irvine. Tying knots in light fields. *Physical Review Letters*, 111(15):150404, 2013.

[20] Richard D. Hazeltine and James D. Meiss. *Plasma Confinement*. Dover Publications, Inc., Mineola, NY, 2003.

[21] Roger Penrose and Wolfgang Rindler. *Spinors and Space-Time: Volume 2, Spinor and Twistor Methods in Space-Time Geometry*. Cambridge monographs on mathematical physics. Cambridge University Press, Cambridge, 1988.

[22] Roger Penrose and M. A. H. MacCallum. Twistor theory: An approach to the quantisation of fields and space-time. *Physics Reports*, 6(4):241–316, 1972.

[23] Roy Maartens and Bruce A. Bassett. Gravito-electromagnetism. *Classical and Quantum Gravity*, 15(3):705, 1998.

[24] David A. Nichols, Robert Owen, Fan Zhang, Aaron Zimmerman, Jeandrew Brink, Yanbei Chen, Jeffrey D. Kaplan, Geoffrey Lovelace, Keith D. Matthews, Mark A. Scheel, and Kip S. Thorne. Visualizing spacetime curvature via frame-drag vortexes and tidal tendexes: General theory and weak-gravity applications. *Phys. Rev. D*, 84(12):124014, 2011.

[25] G. W. Leibniz. Math. schriften. *Göttinger Studien (Abtheilung 1)*, 2:19–20, 1850.

[26] A. T. Vandermonde. Remarques sur les problémes de situation. *Mémoires de l'Académie Royale des Sciences (Paris)*, 2:566–574, 1771.

[27] J. H. Przytycki. Classical roots of knot theory. *Chaos, Solitons, and Fractals*, 9(4-5):531–545, 1998.

[28] C. Nash. Topology and physics - a historical essay. 1997, arXiv:hep-th/9709135.

[29] H. Brunn. Topologische betrachtungen. *Zeitschrift für Mathematik und Physik*, 37:106–116, 1892.

[30] John C. Baez and Javier P. Muniain. *Gauge Fields, Knots, and Gravity*. K & E Series on Knots and Everything. World Scientific, Singapore, 1994.

[31] J. J. O'Conner and E. F. Robertson. Topology and Scottish mathematical physics. 2001. http://www-history.mcs.st-andrews.ac.uk/HistTopics/Knots_and_physics.html.

[32] William H. Cropper. *Great Physicists: The Life and Times of Leading Physicists from Galileo to Hawking*. Oxford University Press, Oxford, 2004.

[33] Bence Jones. *The Life and Letters of Faraday, Volume 2*. Longmans, Green, ans Co., London, 1870.

[34] Michael Faraday. On the conservation of force. *Proceedings of the Royal Institution of Great Britain*, 2:352–365, 1857.

[35] Michael Faraday and Frank A. J. L. James. *The Correspondence of Michael Faraday, Volume 5: 1855-1860*. Institution of Electrical Engineers, London, 2008.

[36] Fan Zhang, Aaron Zimmerman, David A. Nichols, Yanbei Chen, Geoffrey Lovelace, Keith D. Matthews, Robert Owen, and Kip S. Thorne. Visualizing spacetime curvature via frame-drag vortexes and tidal tendexes II. stationary black holes. *Phys. Rev. D*, 86(8):084049, 2012.

[37] David A. Nichols, Aaron Zimmerman, Yanbei Chen, Geoffrey Lovelace, Keith D. Matthews, Robert Owen, Fan Zhang, and Kip S. Thorne. Visualizing spacetime curvature via frame-drag vortexes and tidal tendexes III. quasinormal pulsations of schwarzschild and kerr black holes. *Phys. Rev. D*, 86(10):104028, 2012.

[38] Mitchell A. Berger. Introduction to magnetic helicity. *Plasma Physics and Controlled Fusion*, 41(12B):B167, 1999.

[39] Roger Penrose and Wolfgang Rindler. *Spinors and Space-Time: Volume 1, Two-Spinor Calculus and Relativistic Fields*. Cambridge Monographs on Mathematical Physics. Cambridge University Press, Cambridge, 1987.

[40] William T. M. Irvine. Linked and knotted beams of light, conservation of helicity and the flow of null electromagnetic fields. *Journal of Physics A: Mathematical and Theoretical*, 43(38):385203, 2010.

[41] Manuel Arrayás and José L. Trueba. Exchange of helicity in a knotted electromagnetic field. 2011, arXiv:hep-th/1105.6285.

[42] R. Fitzpatrick, R. D. Hazeltine, and F. L. Waelbroeck. Introduction to plasma physics: A graduate level course. *University of Texas at Austin, Austin, TX*, 2006, http://farside.ph.utexas.edu/teaching/plasma/380.pdf.

[43] P. M. Bellan. *Fundamentals of Plasma Physics*. Cambridge University Press, Cambridge, 2006.

[44] Masaaki Yamada, Hantao Ji, Scott Hsu, Troy Carter, Russell Kulsrud, Norton Bretz, Forrest Jobes, Yasushi Ono, and Francis Perkins. Study of driven magnetic reconnection in a laboratory plasma. *Physics of Plasmas*, 4(5):1936–1944, 1997.

[45] Hantao Ji, Stephen Terry, Masaaki Yamada, Russell Kulsrud, Aleksey Kuritsyn, and Yang Ren. Electromagnetic fluctuations during fast reconnection in a laboratory plasma. *Physical Review Letters*, 92(11):115001, 2004.

[46] D. E. Evans and P. G. Carolan. Measurement of magnetic field in a laboratory plasma by Thomson scattering of laser light. *Physical Review Letters*, 25(23):1605–1608, 1970.

[47] Pasquale Blasi, Scott Burles, and Angela V. Olinto. Cosmological magnetic field limits in an inhomogeneous universe. *The Astrophysical Journal Letters*, 514(2):L79–L82, 1999.

[48] R. Schlickeiser and P. K. Shukla. Cosmological magnetic field generation by the Weibel instability. *The Astrophysical Journal Letters*, 599(2):L57–L60, 2003.

[49] R. C. Duncan and C. Thompson. Formation of very strongly magnetized neutron stars - implications for gamma-ray bursts. *The Astrophysical Journal Letters*, 392(1):L9–L13, 1992.

[50] M. D. Kruskal and R. M. Kulsrud. Equilibrium of a magnetically confined plasma in a toroid. *The Physics of Fluids*, 1(4):265–274, 1958.

[51] J. P. Goedbloed, Rony Keppens, and Stefaan Poedts. *Advanced Magnetohydrodynamics*. Cambridge University Press, Cambridge, UK, 2010.

[52] Ying Ran, Pavan Hosur, and Ashvin Vishwanath. Fermionic Hopf solitons and Berry's phase in topological surface superconductors. *Physical Review B*, 84(18):184501, 2011.

[53] I. E. Dzyloshinskii and B. A. Ivanov. Localized topological solitons in a ferromagnet. *Journal of Experimental and Theoretical Physics*, 29(9):540–542, 1979.

[54] Michikazu Kobayashi and Muneto Nitta. Torus knots as hopfions. *Physics Letters B*, 728:314–318, 2014.

[55] A. N. Kalinkin and V. M. Skorikov. Toroidal solitons in magnetic oxides, Bose-Einstein condensates, and other media. *Inorganic Materials*, 43(5):526–536, 2007.

[56] L. Pismen and S. Rica. Fermions on a vortex ring. *Physical Review D*, 66(4):045004, 2002.

[57] Richard A. Battye, N. R. Cooper, and Paul M. Sutcliffe. Stable skyrmions in two-component Bose-Einstein condensates. *Physical Review Letters*, 88(8):080401, 2002.

[58] A. A. Zhmudskii and B. A. Ivanov. Dynamical topological solitons in a two-dimensional ferromagnet. *Journal of Experimental and Theoretical Physics*, 88(4):833–843, 1999.

[59] V. S. Semenov, D. B. Korovinski, and H. K. Biernat. Euler potentials for the MHD Kamchatnov-Hopf soliton solution. *Nonlinear Processes in Geophysics*, 9(3-4):347–354, 2002.

[60] Simon Candelaresi and Axel Brandenburg. Topological constraints on magnetic field relaxation. *Solar and Astrophysical Dynamos and Magnetic Activity*, 8(S294):353–357, 2012.

[61] Simon Candelaresi, Fabio Del Sordo, and Axel Brandenburg. Influence of magnetic helicity in MHD. *Proceedings of the International Astronomical Union*, 6(S271):369–370, 2011.

[62] Mitchell Berger and George B. Field. The topological properties of magnetic helicity. *Journal of Fluid Mechanics*, 147:133–148, 1984.

[63] Fabio Del Sordo, Simon Candelaresi, and Axel Brandenburg. Magnetic field decay of three interlocked flux rings with zero linking number. *Physical Review E*, 81(3):036401, 2010.

[64] Simon Candelaresi and Axel Brandenburg. Decay of helical and nonhelical magnetic knots. *Physical Review E*, 84(1):016406, 2011.

[65] Simon Candelaresi, Fabio Del Sordo, and Axel Brandenburg. Decay of trefoil and other magnetic knots. *Advances in Plasma Astrophysics*, 6(S274):461–463, 2011.

[66] A. R. Yeates, G. Hornig, and A. L. Wilmot-Smith. Topological constraints on magnetic relaxation. *Physical Review Letters*, 105(8):085002, 2010.

[67] A. R. Yeates and G. Hornig. Dynamical constraints from field line topology in magnetic flux tubes. *Journal of Physics A: Mathematical and Theoretical*, 44(26):265501, 2011.

[68] Roscoe B. White. *The Theory of Toroidally Confined Plasmas*. Imperial College Press, London, 2001.

[69] W. D. D'Haeseleer, W. N. G. Hitchon, J. D. Callen, and J. L. Shohet. *Flux Coordinates and Magnetic Field Structure*. Springer, Berlin, 1991.

[70] A. H. Boozer. Establishment of magnetic coordinates for a given magnetic field. *Physics of Fluids*, 25(3):520–521, 1982.

[71] Shigeo Hamada. Hydromagnetic equilibria and their proper coordinates. *Nuclear Fusion*, 2(1-2):23–37, 1962.

[72] S. Chandrasekhar and E. Fermi. Problems of gravitational stability in the presence of a magnetic field. *The Astrophysical Journal*, 118:116–141, 1953.

[73] Donat G. Wentzel. On the shape of magnetic stars. *The Astrophysical Journal*, 133:170–183, 1961.

[74] L. Mestel, J. Nittmann, W. P. Wood, and G. A. E. Wright. The internal dynamics of the oblique rotator. II. *Monthly Notices of the Royal Astronomical Society*, 195:979–1000, 1981.

[75] Paul D. Lasky and Andrew Melatos. Tilted torus magnetic fields in neutron stars and their gravitational wave signatures. *Physical Review D*, 88(10):103005, 2013.

[76] P. Ghosh and F. K. Lamb. Disk accretion by magnetic neutron stars. *The Astrophysical Journal*, 223:L83–L87, 1978.

[77] The Pencil-Code: a high-order finite-difference code for compressible MHD, May 2014, http://pencil-code.nordita.org/.

[78] Simon Candelaresi, Alexander Hubbard, Axel Brandenburg, and Dhrubaditya Mitra. Magnetic helicity transport in the advective gauge family. *Physics of Plasmas*, 18(1):012903, 2011.

[79] Wolfgang Dobler, Anvar Shukurov, and Axel Brandenburg. Nonlinear states of the screw dynamo. *Physical Review E*, 65(3):036311, 2002.

[80] D. Mitra, S. Candelaresi, P. Chatterjee, R. Tavakol, and A. Brandenburg. Equatorial magnetic helicity flux in simulations with different gauges. *Astronomical Notes*, 331(1):130–135, 2010.

[81] Axel Brandenburg. The inverse cascade and nonlinear alpha-effect in simulations of isotropic helical hydromagnetic turbulence. *The Astrophysical Journal*, 550(2):824–840, 2001.

[82] Roger Penrose. Twistor algebra. *Journal of Mathematical Physics*, 8(2), 1967.

[83] Peter J. O'Donnell. *Introduction to 2-spinors in General Relativity*. World Scientific, Singapore, 2003.

[84] Richard S. Ward and Raymond O. Wells. *Twistor geometry and field theory*. Cambridge University Press, Cambridge, 1991.

[85] L. Filipe O. Costa, Carlos A. R. Herdeiro, and Lode Wylleman. Electromagnetic and gravitational invariants. *Journal of Physics: Conference Series*, 314(1):012072, 2011.

[86] Maciej Dunajski. *Solitons, instantons, and twistors*, Volume 19 of *Oxford Graduate Texts in Mathematics*. Oxford University Press, Oxford, 2010.

[87] Lane P. Hughston and Richard S. Ward. An introduction to twistor theory. In *Advances in twistor theory*. Pitman Publishing Limited, London, 1979.

[88] Stephen A. Huggett and Kenneth P. Tod. *An introduction to twistor theory*, Volume 4 of *London Mathematical Society Student Texts*. Cambridge University Press, Cambridge, 1994.

[89] H. K. Urbantke. The Hopf fibration - seven times in physics. *Journal of Geometry and Physics*, 46(2):125–150, 2003.

[90] E. T. Whittaker. On the partial differential equations of the mathematical physics. *Mathematische Annalen*, 57:333–355, 1903.

[91] Harry Bateman. *The Mathematical Analysis of Electrical and Optical Wavemotion on the Basis of Maxwell's Equations*. Cambridge University Press, Cambridge, 1915.

[92] Roger Penrose. Twistor theory: its aims and achievements. In C. J. Isham, R. Penrose, and D. W. Sciama, editors, *Quantum Gravity, an Oxford Symposium*. Oxford University Press, Oxford, 1975.

[93] Roger Penrose. On the origins of twistor theory. In W. Rindler and A. Trautman, editors, *Gravitation and geometry, a Volume in Honour of I. Robinson*. Bibliopolis, Naples, 1987.

[94] Roger Penrose. Solutions of the zero-rest-mass equations. *Journal of Mathematical Physics*, 10(38):38–39, 1969.

[95] Roger Penrose. Twistor quantisation and curved space-time. *International Journal of Theoretical Physics*, 1(1):61–99, 1968.

[96] Emil Grgin. *A global technique for the study of spinor fields*. Ph.D. Thesis, Syracuse University, 1966.

[97] Andrew Hodges. Twistor diagrams. *Physica A: Statistical Mechanics and its Applications*, 114(1):157–175, 1982.

[98] M. G. Eastwood and A. M. Pilato. On the density of twistor elementary states. *Pacific Journal of Mathematics*, 151(2):201–215, 1991.

[99] Ivor Robinson. Null electromagnetic fields. *Journal of Mathematical Physics*, 2(3):290–291, 1961.

[100] Dale Rolfsen. *Knots and Links.* AMS Chelsea Publishing, Providence, RI, 1976.

[101] Pik-Yin Lai. Dynamics of polymer knots at equilibrium. *Physical Review E*, 66(2):021805, 2002.

[102] Adam D. Swetnam, Charles Brett, and Michael P. Allen. Phase diagrams of knotted and unknotted ring polymers. *Physical Review E*, 85(3):031804, 2012.

[103] S. A. Wasserman and N. R. Cozzarelli. Supercoiled DNA-directed knotting by T4 topoisomerase. *The Journal of Biological Chemistry*, 266(30):20567–73, 1991.

[104] Davide Marenduzzo, Enzo Orlandini, Andrzej Stasiak, De Witt Sumners, Luca Tubiana, and Cristian Micheletti. DNA-DNA interactions in bacteriophage capsids are responsible for the observed DNA knotting. *Proceedings of the National Academy of Sciences*, 106(52):22269–74, 2009.

[105] Sergei Gukov. Three-dimensional quantum gravity, Chern-Simons theory, and the A-polynomial. *Communications in Mathematical Physics*, 255(3):577–627, 2005.

[106] M. S. El Naschie. Fuzzy multi-instanton knots in the fabric of spacetime and Dirac's vacuum fluctuation. *Chaos, Solitons & Fractals*, 38(5):1260–1268, 2008.